

# NUCLEAR SHAPES IN MEAN FIELD THEORY

*Sven Åberg*

Lund Institute of Technology, Department of Mathematical Physics,  
P.O. Box 118, S-221 00 Lund, Sweden

*Hubert Flocard*

Division de Physique Théorique\*, Institute de Physique Nucléaire,  
F-91406 Orsay Cedex, France

*Witold Nazarewicz*

Institute of Physics, Warsaw University of Technology,  
PL-00662, Warsaw, Poland

**KEY WORDS:** Hartree-Fock, Nilsson-Strutinsky, high spin, superdeformations,  
shape coexistence, octupole shapes, neutron-proton interaction.

---

## CONTENTS

|   |     |
|---|-----|
| 1. INTRODUCTION .....   | 440 |
| 2. MEAN FIELD THEORY .....  | 442 |
| 2.1 <i>Effective Interactions</i> .....                               | 442 |
| 2.2 <i>Constrained Hartree-Fock Method</i> .....                      | 443 |
| 2.3 <i>Constrained Hartree-Fock-Bogolyubov Method</i> .....           | 444 |
| 2.4 <i>Self-Consistent Symmetries</i> .....                           | 446 |
| 2.5 <i>Nilsson-Strutinsky Approach</i> .....                          | 447 |
| 3. NUCLEAR SHAPES .....   | 452 |
| 3.1 <i>Parametrization</i> .....                                      | 452 |
| 3.2 <i>Shape Consistency in the Nilsson-Strutinsky Approach</i> ..... | 453 |
| 4. QUADRUPOLE SHAPES .....  | 454 |
| 4.1 <i>Axially Symmetric Shapes</i> .....                             | 454 |
| 4.2 <i>Triaxial Shapes</i> .....                                      | 455 |
| 5. NUCLEAR SHAPES AT HIGH ANGULAR MOMENTA .....                       | 457 |

\* Unité de Recherche des Universités Paris VI et Paris XI associée au Centre National de la Recherche Scientifique.

|     |  |     |
|-----|--|-----|
| 5.1 | <i>Centrifugal Stretching</i> .....                | 457 |
| 5.2 | <i>Polarization by Decoupled Particle(s)</i> ..... | 462 |
| 5.3 | <i>Well-Deformed Intruder Bands</i> .....          | 466 |
| 5.4 | <i>Band Termination</i> .....                      | 468 |
| 5.5 | <i>Noncollective Rotation</i> .....                | 470 |
| 5.6 | <i>Superdeformations</i> .....                     | 476 |
| 6.  | REFLECTION-ASYMMETRIC SHAPES .....                 | 488 |
| 6.1 | <i>Occurrence</i> .....                            | 489 |
| 6.2 | <i>Spectroscopy</i> .....                          | 494 |
| 6.3 | <i>Dipole Moments</i> .....                        | 497 |
| 6.4 | <i>Exotic Octupole Shapes</i> .....                | 499 |
| 7.  | SHAPE COEXISTENCE .....                            | 502 |
| 7.1 | <i>Competing Prolate and Oblate States</i> .....   | 502 |
| 7.2 | <i>Spherical-Deformed Shape Isomers</i> .....      | 506 |
| 7.3 | <i>Pairing Isomers</i> .....                       | 510 |
| 8.  | OTHER INTERACTIONS .....                           | 511 |
| 8.1 | <i>Neutron-Proton Interaction</i> .....            | 511 |
| 8.2 | <i>Higher Deformations</i> .....                   | 515 |
| 9.  | NEW DEVELOPMENTS .....                             | 516 |
| 9.1 | <i>The Configuration Concept</i> .....             | 516 |
| 9.2 | <i>Relativistic Mean Field</i> .....               | 517 |
| 10. | BEYOND THE MEAN FIELD APPROACH .....               | 518 |

## 1. INTRODUCTION

The basic assumption of low-energy nuclear theory is that the nucleus can be described as a set of nonrelativistic nucleons interacting via a two-body interaction. Over the last half century, this assumption has been verified by many successes. This does not mean, however, that the nuclear many-body problem is close to being solved. The detailed microscopic understanding of the origin of the nuclear shell model was, and in some respect still remains, a major challenge. Even now the basic ingredient, namely the interaction between nucleons, is still a matter of discussion. Its dominant features are certainly known: a repulsive hard core at short distances, a strong attraction at intermediate distances, and a long-range force dominated by the one-pion exchange. The interaction between nucleons is strong both in its attractive and repulsive components. At first sight it is therefore difficult to explain why a finite assembly of such strongly interacting particles in so many respects can behave like a set of independent particles within a self-built shell model. However, particularly because of Pauli blocking, the mean free path of the nucleons increases by an order of magnitude inside the nucleus, which thereby facilitates a shell model description.

The nucleonic motion may occur in a highly correlated way, giving rise to vibrational-like and to rotational-like spectra as well as to large quadrupole moments. These experimental findings led Rainwater, Bohr, and Mottelson (1-4) in the early 1950s to introduce the concept of the

nonspherical nucleus, a concept that plays a central role in nuclear structure physics. Furthermore, it was possible to get a unified understanding of collective and single-particle degrees of freedom. It is, however, interesting to note that some consequences of nuclear deformation were discussed as early as 1937 by N. Bohr and F. Kalckar (5).

Since this first work on nuclear shapes and collective motion, much progress has been achieved (6–11). Many interesting phenomena have been observed, such as the rich variety of nuclear shapes in which various intrinsic symmetries are spontaneously broken. In addition to the well-known “phase transition” from a spherical to a deformed shape, a transition to shapes that break reflection symmetry has also been found. Many regions of the nuclear chart are found to be well deformed, and several nuclei exhibit an excited state connected with a deformation other than the ground state (“shape coexistence”). Improved experimental facilities have opened a new dimension in the study of nuclear shape and structure, namely the angular momentum degree of freedom (12). Rotation significantly influences the shape of the nucleus. A multitude of interesting phenomena have been observed in the rapidly rotating nucleus, for example a termination of the rotational band, the existence of high-spin isomeric states, the possible occurrence of triaxial shapes, and most spectacularly, the existence of superdeformed shapes (with axis ratio 2:1) that can be surrounded by thousands of states of other shapes without significantly mixing with them. The explanation of all these phenomena can be found in the mean field theory. This shows the power of mean field calculations, performed in the spirit of the Hartree-Fock (HF) method or in the more approximative but transparent Nilsson-Strutinsky (NS) approach.

Before entering the fascinating world of recent theoretical and experimental findings, we briefly discuss in Section 2 the basis of the mean field theory and the relations between the Hartree-Fock and Nilsson-Strutinsky approaches. The parametrization of the nuclear shape is discussed in Section 3, where the shape consistency in the Nilsson-Strutinsky approach is also analyzed and found to be satisfying. Then mean field calculations of nuclear shapes are reviewed, starting in Section 4 with the quadrupole degrees of freedom, including triaxial ground-state shapes. The various shapes and phenomena occurring in the rotating nuclei are discussed in Section 5. We consider nuclei at all spins over the entire periodic table, from the lightest p- or sd-shell nuclei to the heaviest elements. A rather extended (although far from complete) discussion in Section 5.6 deals with superdeformed nuclei. Octupole shapes are discussed in Section 6 and the phenomenon of shape coexistence in Section 7. The role played by different nonstandard residual interactions is reviewed in Section 8, where the focus

is on higher multipole moments in the shape parametrization as well as on the neutron-proton interaction. In Section 9 recent developments of the mean field approach are briefly reviewed, such as the concept of specifying a nucleonic configuration in terms of approximately good quantum numbers, and also the recent interesting attempts toward a relativistic mean field theory. Finally, in Section 10 a few words are said about what is missing in a mean field description.

In several places we compare different types of mean field calculations such as Nilsson-Strutinsky calculations using different nuclear potentials, or self-consistent Hartree-Fock calculations using Skyrme or Gogny forces. In general, all these different recipes for calculating shapes and excitation spectra yield astonishingly similar results. This means that the phenomenological terms in the mean field Hamiltonian representing deformation, pairing, and rotation generate rather optimal trial wave functions. Particularly at large deformations or at high spins, such a selection would require an extremely large basis in spherical shell model or boson expansion approaches.

## 2. MEAN FIELD THEORY

In this section we very briefly discuss some important concepts of nuclear mean field theory, and the necessary steps from the bare nucleon-nucleon interaction over effective interactions (Section 2.1) to the constrained Hartree-Fock (Section 2.2) and Hartree-Fock-Bogolyubov (HFB; Section 2.3) methods, and finally to the more easily handled Nilsson-Strutinsky approach (Section 2.5). In Section 2.4 we discuss preserved symmetries of the deformed mean field, where the mean field may be “deformed” in the ordinary space as well as in the gauge space. More detailed discussions of these concepts can be found elsewhere (6–8, 13).

### 2.1 *Effective Interactions*

The effective interaction between the nucleons within the nuclear medium can be derived from the bare nucleon-nucleon force by means of the Brückner theory (14, 15 and references therein). It defines an effective force (also named the *G*-matrix) that includes the effects of the hard core to infinite order. The adjective “effective” is indicative of the residual nature of an interaction acting between quasi-nucleons dressed by a strong short-range force. However, the Brückner procedure is difficult to handle and further approximations are necessary. Among them, the most successful is the density matrix expansion (16, 17). At the cost of one phenomenological parameter, it leads to interactions that, once used within Hartree-Fock calculations, reproduce the binding energies and radii of closed-shell

(spherical) nuclei. Unfortunately, the rather complex analytical structure of these effective interactions has prevented their systematic use in describing nuclear properties.

This task is generally ascribed to simpler phenomenological effective interactions. Their structure and complexity vary greatly depending on the range of properties one expects them to predict. A first example, close in spirit to the Brückner G-matrix, is provided by the Gogny and the Skyrme families of forces (18–22 and references quoted therein). They are devised for HF or HFB calculations, taking into account all the nucleons. Therefore they do not assume an a priori separation between a core and some valence nucleons. Their domain of application extends over the complete chart of elements. They have been used to predict a wide set of data related either with bulk nuclear properties like the binding energy and the charge density, or with energy surfaces describing the variations of the energy with respect to one or several collective deformations. These interactions depend on a small number of parameters (typically five to ten) determined by adjusting the properties of magic nuclei. Based on a local density approximation, one can establish a connection between these forces and Brückner G-matrices (23–25).

The other type of effective force describes nucleon interactions only in the vicinity of the Fermi surface. Among such descriptions, the separable forces play a special role because they can be directly associated with nuclear deformations. An example of such a force is the  $Q$ - $Q$  quadrupole interaction acting in the particle-hole (ph) channel, or the  $P^\dagger$ - $P$  pairing force acting in the particle-particle (pp) channel. The pairing-plus-quadrupole model describes with good accuracy the residual interactions prevalent in both spherical and deformed valence shells (26–29). Although it cannot be used to predict bulk nuclear properties, it has successfully predicted collective deformation properties within HF calculations restricted to the valence shell.

## 2.2 Constrained Hartree-Fock Method

The natural microscopic formulation of the shell model is provided by the Hartree-Fock method. Given an effective Hamiltonian  $H$  (from now on, we omit the adjective “effective”), the many-body wave function is approximated by a Slater determinant whose orbitals are determined by a minimization of the total energy  $E$ ,  $E = \langle H \rangle$ . This variation leads to an eigenvalue problem that, for a nucleus of mass  $A$ , defines both the orbitals  $\{\Phi_i, i = 1, \dots, A\}$  of the Slater determinant, and the single-particle energies  $e_i$ ,

$$h\Phi_i = e_i\Phi_i. \quad 1.$$

The HF Hamiltonian,  $h$ , appearing in this equation is a one-body operator defined self-consistently from the interaction and the orbitals.

A specific feature of the nuclear shell model is a strong coupling of the mean field with low-energy collective modes. Very early it was recognized that this coupling could be incorporated within the HF method by the addition of constraints proportional to some collective operators. The microscopic construction of these operators is still in great part unresolved (30–34). Nevertheless, the successful analysis of the data by phenomenological models such as the Bohr Hamiltonian (7, 35) suggests that most low-lying collective modes can be associated with quadrupole (hexadecapole and octupole) deformations of the isoscalar nuclear density.<sup>1</sup> It is therefore natural to associate a collective deformation of order  $l$  with a constraint proportional to the one-body operator  $f_l(r) Y_{lm}$ . If  $Q_k$  ( $k = 1, \dots, k_{\max}$ ) denotes the set of constraining operators, the HF solution is determined by the Routhian equation:

$$h' \Phi_i = \left( h - \sum_{k=1}^{k_{\max}} \lambda_k Q_k \right) \Phi_i = e_i \Phi_i, \quad 2.$$

in which the Lagrange multiplier  $\lambda_k$  is fixed in such a way that the expectation value  $\langle Q_k \rangle$  equals  $\mathcal{Q}_k$ . Here  $\mathcal{Q}_k$  is the collective coordinate associated with the operator  $Q_k$ . By varying the  $\mathcal{Q}$  values, one covers the entire collective space and constructs the potential-energy surface (PES); i.e. the variation of the HF binding energy with respect to  $\mathcal{Q}$  (see 36–39).

### 2.3 Constrained Hartree-Fock-Bogolyubov Method

The HF method used with interactions like that of Skyrme describes well the major features of the shell model. However, it is not sufficient to explain all the details of the collective PESs. Indeed, bulk properties (for instance, the odd-even variation of the total binding energies as a function of the neutron or proton numbers) and the low-lying spectroscopy are both affected by pairing correlations (40). Their correct description requires a knowledge of the residual interaction in the pp channel and an extension of the notion of mean field (41–43).

Pairing can be taken into account directly by the effective force, for example with the Gogny force, or it can be defined separately. Experience has shown that its dominant feature is a short-range attraction in the  $T = 1$  isospin channel. It can therefore be simulated with a delta force acting only on like nucleons. Sometimes one introduces a further sim-

<sup>1</sup> Because of the strong neutron-proton attraction, nuclear isovector modes are associated with higher excitation energy.

plification and uses the so-called seniority interaction, in which all pairs of time-reversed nucleons interact with the same strength (28, 29, 44). In view of their extreme schematization, both the delta and seniority forces are only meaningful in the vicinity of the Fermi surface. In addition, their strength must be adjusted according to the size of the nucleon space in which they are acting.

The microscopic extension of the mean field that incorporates pairing correlations is the HFB method (45–49). In it, the  $N$ -body wave function is approximated by an independent quasi-particle state, e.g. the Bardeen-Cooper-Schrieffer (BCS) state. The HFB equation can be written in a form similar to the HF equation (Equation 2):

$$\mathcal{H}'\Psi_i = E_i\Psi_i; \quad \mathcal{H}' = \begin{pmatrix} h' - \lambda & \Delta \\ -\Delta^* & -h'^* + \lambda \end{pmatrix}, \quad 3.$$

where  $E_i$  are quasi-particle excitation energies. In this equation, the Fermi energy  $\lambda$  is self-consistently determined by requiring that the average values of the nucleon numbers be equal to those of the considered nucleus. The HFB method therefore introduces an additional approximation: the eigenstate of Equation 3 is no longer an eigenstate of the nucleon number. In the HFB Equation 3, there appears a pairing field  $\Delta$ . Experience has shown that its accurate determination is crucial for a correct description of low-energy nuclear spectroscopy.

In nuclear physics there exists a strong analogy between pairing and deformation. Both are associated with attractive interactions, and both generate correlations that can be treated with good accuracy within the mean field approximation. In the ph subspace, the mass quadrupole operator,  $Q_{2m} = f_2(r)Y_{2m}$ , plays the role held by the pair operator,  $P + P^\dagger$ , in the particle-particle subspace. For magic nuclei and in their close neighborhood, the mean field expectation value of these two operators vanishes. However, as more nucleons are added to fill the valence shell, the fluctuations in  $Q$  and  $P + P^\dagger$  grow steadily. For some critical value of the nucleon number, there appears a second-order instability, which results in optimal mean field solutions with nonzero expectation values of the  $Q$  and  $P + P^\dagger$  operators.<sup>2</sup> These quantities then play the role of order parameters, and the “phase transition” results in the spontaneous breaking of a symmetry. This changes the spectrum from vibrational-like to rotational-like over an intermediate transitional region. In Figure 1 we schematically show the potential-energy curves to illustrate this “phase tran-

<sup>2</sup> Such a transition can be viewed as a nuclear version of the Jahn-Teller effect giving rise to a spontaneous symmetry breaking in molecules (see 50, 51 for more details).

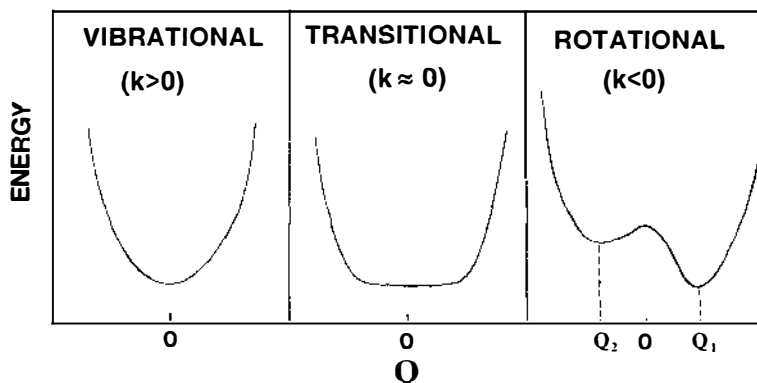


*Figure 1* Schematic illustration of the spontaneous breaking of a symmetry associated with the field  $Q$ .  $Q$  may be a deformation degree of freedom such as  $\beta_2$  or  $\beta_3$ , or for example the pairing field  $\Delta$ . Consequences of some broken symmetries can be seen in Table I. Depending on the potentials' curvature at spherical shape,  $k = d^2E/dQ^2$ , the collective dynamic results in the spectrum characteristics of a vibrational, transitional, or rotational system.

sition.” The onset of deformation may be triggered by changes in, for example, particle number or angular momentum. In Figure 1 the collective coordinate,  $Q$ , may be quadrupole or octupole deformation but it may also correspond to  $\Delta$ , i.e. a “deformation” in the pairing space or pp direction. The correspondence between deformation in ordinary space and in the pairing space (“gauge space”) can also be extended to the collective energy spectrum (e.g. 8). We have seen that PES obtained by HF calculations with a constraint on  $Q$  tell us about the characteristics of low-energy quadrupole excitations. Similarly, HFB calculation constrained on  $P + P^\dagger$  provide information on the low-lying pairing vibration (52–54).

## 2.4 Self-Consistent Symmetries

Any mean field solution when it is deformed, either in the ph or the pp direction, breaks one of the basic symmetries of the nuclear Hamiltonian. A Hartree-Fock solution with  $\langle Q \rangle \neq 0$  is not an eigenstate of the angular momentum  $I$ . In a similar way, the solution of the HFB equation is not an eigenstate of the nucleon number operator  $\hat{N}$ . The latter symmetry can be restored by projecting the mean field solutions onto states of good particle number (55–58). However, even at the level of the mean field theory, it is possible to construct wave functions that at least approximately take into account the effects of such a projection (59–62). We have already seen an example in the HFB equation that includes a constraint  $-\lambda\hat{N}$  in order to ensure the correct average nucleon number. By varying the value



of the Fermi energy  $\lambda$ , one generates HFB solutions for a sequence of nuclei. In a completely equivalent manner, approximate solutions of states of good angular momentum can be obtained by what is called the self-consistent cranking method (63). It can be shown that the addition to the mean field of a single constraining operator,  $\omega I_x$ , amounts to an approximate projection on a state of good angular momentum (59–61, 64, 65). For a state of total spin  $I$  belonging to a given  $K$  band, the value of the Lagrange multiplier  $\omega$ , which plays the role of an angular velocity, must be selected such that the expectation value of  $I_x$  satisfies the relation

$$\langle I_x \rangle = \sqrt{I(I+1) - K^2}. \quad 4.$$

Experience has shown that the predictions of cranked and/or deformed HF or HFB calculations often agree very accurately with data, despite the breaking of rotational invariance (66–75).

Not all symmetries of the wave functions are destroyed in such calculations (76). The remaining symmetries provide a simplification of the calculation as well as a convenient labeling of the individual orbitals. Among the possible set of remaining symmetries, usage has selected those associated with the following operators: the time-reversal; the parity; the signature (77, 78), i.e. half turn around the  $x$  axis,  $\exp(-i\pi I_x)$ ; and the simplex, i.e. parity times the inverse of signature. Depending on the constraints, the mean field solution will possess one or several of these symmetries. Table 1 indicates the preserved symmetries for selected types of deformations or constraints. If, in addition, the calculations are restricted to purely axial deformations, the cylindrical symmetry ensures that the orbitals can be chosen among the eigenstates of the operator  $J_z$  and therefore be labelled by the additional quantum number  $K$ . The single-particle quantum numbers associated with the symmetries  $P$ ,  $R$ , and  $S$  are denoted as  $\pi$ ,  $r$ , and  $s$ , and may take the values  $+$  or  $-$ ,  $+i$  or  $-i$ , and  $+i$  or  $-i$ , respectively. Instead of the signature quantum number, one often uses the signature exponent,  $\alpha$ ,  $r = \exp(-i\pi\alpha)$ . The total signature exponent can be related to the total angular momentum by means of  $\alpha = I(\text{mod } 2)$ .

## 2.5 Nilsson-Strutinsky Approach

The HF and the HFB equations form a set of coupled nonlinear integro-differential equations. Their solution therefore remains, even today, a difficult task despite steady improvements in both the numerical algorithms and the speed of computers. For this reason, although HF or HFB analysis of structure problems is becoming more numerous, nuclear physicists still rely in large part on an alternative and simpler method developed by

**Table 1** Symmetries of the mean field,  $H = H_0 + \sum_{lm} \alpha_{lm} r^l Y_{lm} - \omega I_x + \sum_l \Delta_l (P_l + P_l^\dagger) - \lambda \hat{N}$ , representing different types of constraints

|  |  | Symmetries                  |                   |                      |                                 |                        |                               |
|--|--|-----------------------------|-------------------|----------------------|---------------------------------|------------------------|-------------------------------|
|  | Constraint <sup>a</sup><br>(example)             | Time<br>reversal<br>( $T$ ) | Parity<br>( $P$ ) | Signature<br>( $R$ ) | Simplex <sup>b</sup><br>( $S$ ) | Cylindrical<br>( $K$ ) | Particle<br>number<br>( $N$ ) |
| Even- $l$ , ph<br>deformation<br>no rotation | $\alpha_{2m} r^2 Y_{2m}$                         | yes                         | yes               | yes                  | yes                             | only<br>for<br>$m = 0$ | yes                           |
| Odd- $l$ , ph<br>deformation<br>no rotation  | $\alpha_{3m} r^3 Y_{3m}$                         | yes                         | no                | no                   | yes                             | only<br>for<br>$m = 0$ | yes                           |
| Even- $l$ , ph<br>deformation<br>Cranked     | $\alpha_{2m} r^2 Y_{2m} - \omega I_x$            | no                          | yes               | yes                  | yes                             | no                     | yes                           |
| Odd- $l$ , ph<br>deformation<br>Cranked      | $\alpha_{3m} r^3 Y_{3m} - \omega I_x$            | no                          | no                | no                   | yes                             | no                     | yes                           |
| Even- $l$ , pp<br>deformation<br>Cranked     | $\Delta_l (P_l + P_l^\dagger) - \lambda \hat{N}$ | yes                         | yes               | yes                  | yes                             | yes                    | no                            |

<sup>a</sup> The introduction of the Lagrange operator,  $-\omega I_x$  or  $-\lambda \hat{N}$ , is denoted by "cranked." The mean fields,  $\alpha_{lm} r^l Y_{lm}$  and  $\Delta_l (P_l + P_l^\dagger)$ , are acting in the ph and pp channels, respectively.

<sup>b</sup>  $S = \text{symmetry}$ ;  $S = PR^{-1}$ .

Strutinsky to construct collective PES: the Nilsson-Strutinsky (NS) method (79, 80).

As early as 1955, Nilsson showed that nuclear deformations could be predicted by considering the sum of single-particle energies  $\sum_i \epsilon_i$  of a phenomenological potential designed to reproduce the characteristics of the mean field potential  $h'$  (81, 82; for the inclusion of pairing, see 83). The single-particle Nilsson potential was parametrized in terms of a quadrupole coordinate,  $\epsilon$ , and was later extended to other deformation degrees of freedom (see Section 3.1). In Figure 2 we show a typical Nilsson diagram. The drastic rearrangement of single-particle states due to deformation has been confirmed by experiment and gives a beautiful understanding of low-energy nuclear spectroscopy. Despite its successes, the Nilsson prescription for calculating nuclear deformations could not be used to predict binding energies, nor could it explain nuclear behavior at large deformations such as those encountered in fission. On the other hand, it was well known that these properties were accounted for with good accuracy by the classical model of the liquid drop (84, 85). However, this latter model predicted all nuclei to be spherical. Finally, neither model could explain the long-lived

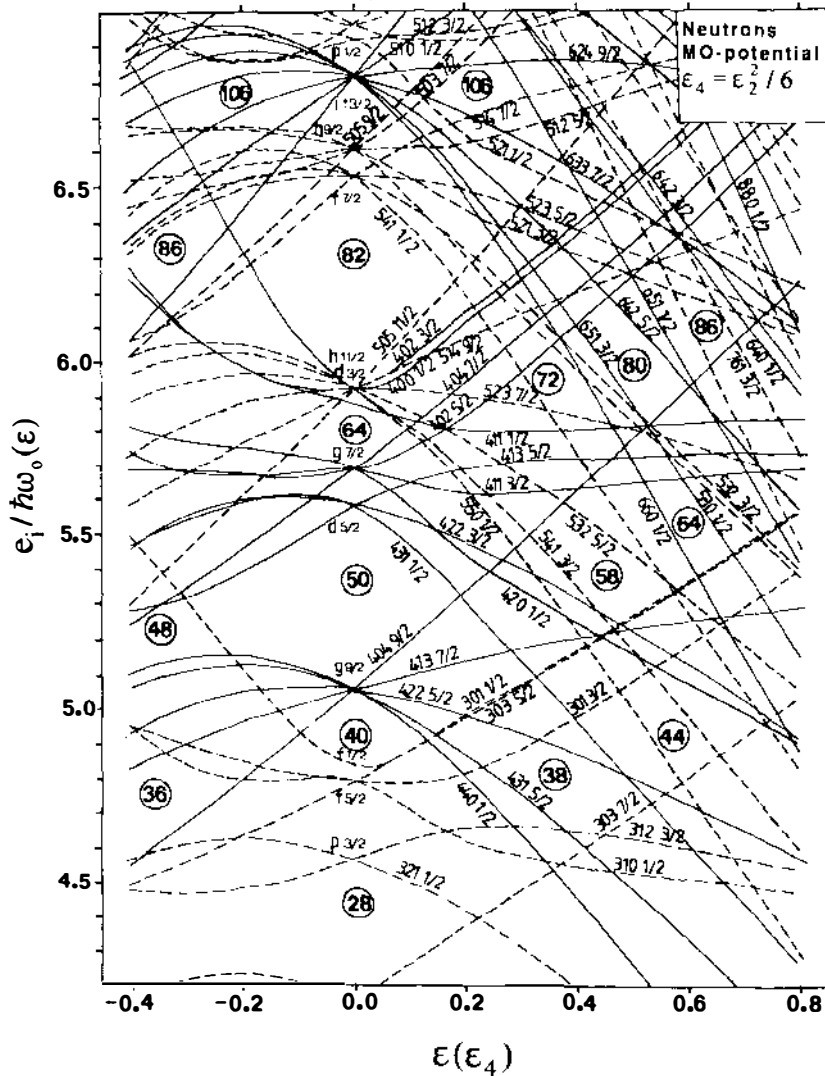


Figure 2 Nilsson diagram valid for neutrons. Potential parameters depend on the main oscillator quantum number (126). The single-particle orbitals are labelled by spherical quantum numbers ( $l$ ) at spherical shape or by means of asymptotic quantum numbers  $[Nn_z\Lambda\Omega]$  at deformed shapes.

fission isomers discovered at the beginning of the 1960s (86–88). The credit for solving this puzzle belongs to Strutinsky. [An early approach was, however, suggested by Swiatecki (89).] Not only did Strutinsky explain the physical contents of both the liquid drop and Nilsson models in terms of more fundamental descriptions like HF or HFB, but he also devised a flexible and simple method incorporating the qualities of the two phenomenological models.

Using the variational nature of the HF method, Strutinsky decomposes the HF binding energy into a sum of three terms of decreasing magnitude. The dominant (or zeroth-order) term varies smoothly as a function of deformation. It can be associated with the liquid drop energy. The first-order term contains the contribution of the shell effects. Its magnitude is typically one hundredth of that of the zeroth-order term. The remaining contribution incorporates the smaller corrections generated by the non-linearity of the HF method. The same analysis applied to the Nilsson prescription shows that the first-order term contained in the quantity  $\sum_i e_i$  matches that of the HF energy. In contrast, the magnitude and the deformation variation of Nilsson's zeroth-order term are unphysical.

Let us review briefly the essentials of Strutinsky's analysis (90–92). The HF energy is a functional of the one-body density matrix  $\rho$ , which can be written in configuration space as

$$\langle \mathbf{r} | \rho | \mathbf{r}' \rangle = \sum_i \Theta(\lambda - e_i) \Phi_i(\mathbf{r}) \Phi_i^*(\mathbf{r}'). \quad 5.$$

In the above expression,  $\Theta$  is a step function of the difference between the single-particle energy  $e_i$  and the Fermi energy. Strutinsky defined the liquid drop energy  $E_{\text{LD}}$  as the value of the same function for a "smoothed" density  $\bar{\rho}$ , defined by

$$\langle \mathbf{r} | \bar{\rho} | \mathbf{r}' \rangle = \sum_i g(\lambda - e_i) \Phi(\mathbf{r}) \Phi^*(\mathbf{r}'). \quad 6.$$

The weight function  $g$  is only required to vary smoothly from 0 to 1 over an energy interval of the order of the difference between successive nuclear shells. If one assumes that  $\rho$  and  $\bar{\rho}$  are close, the stability of the HF energy provides the following expansion in terms of  $\delta\rho = \rho - \bar{\rho}$ :

$$E_{\text{HF}} = E(\rho) = E_{\text{LD}} + \text{tr}[h(\rho)\delta\rho] + O(\delta\rho^2); \quad E_{\text{LD}} = E(\bar{\rho}). \quad 7.$$

The first-order term represents the so-called shell correction. It can be expressed in terms of the single-particle energies and the weight function  $g$ .

In practice, the method is used only when the HF solution and therefore  $h(\rho)$  and  $\{e_i\}$  are unavailable. In such a case, one constructs a simple

approximation of  $h(\bar{\rho})$  by means of an average potential whose shape is adjusted to that of the liquid drop. It is then legitimate to replace the first-order term by  $\text{tr}[h(\bar{\rho})\delta\rho]$  since this affects only the second-order term of the Strutinsky expansion. The numerical verification of this formal expansion had to wait until the mid-1970s when the problems associated with the determination of the effective forces and the solution of the HF equations had been solved. Brack & Quentin (93) demonstrated the correctness of Strutinsky's analysis (see Figure 3). In particular, they calculated the second-order term and demonstrated that its magnitude does not exceed one tenth of the first-order term, and that it does not display any structure as a function of deformation. In most calculations the smoothing function  $g$  entering the definition of  $\bar{\rho}$  is defined phenomenologically. It is also possible to define  $g$  with semiclassical methods based on expansion in  $\hbar$  of the Legendre transform of  $\rho$  (93–96). Both methods give very similar results.

In 1975–1976 the NS method was extended into the domain of high angular momenta (97–100). The formalism remains the same as in the nonrotational case. The shell correction is calculated using the rotating Nilsson scheme, and the macroscopic energy is replaced by the energy of the rotating liquid drop (101) [see Section 5; for the most recent version of the rotating liquid drop model, see (102)]. The inclusion of pairing correlations to the cranked Nilsson scheme, the so-called cranked shell model (CSM), turned out to be a very powerful tool in an interpretation

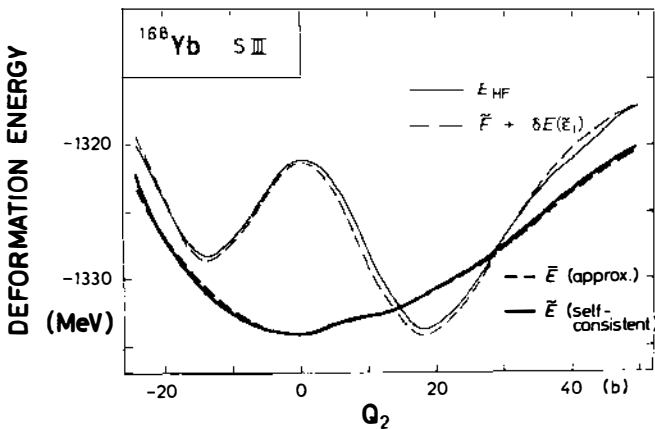


Figure 3 Deformation energy curves for the nucleus  $^{168}\text{Yb}$ . The thin solid line corresponds to the HF energy,  $E_{\text{HF}}$ . The heavy solid line ( $\bar{E}$ ) is the HF liquid drop energy  $E(\bar{\rho})$ . The thick and thin dashed lines show the contribution of the first ("liquid drop energy") and first two terms, respectively, in the Strutinsky expansion. (From 93.)

of near-yrast excitations in rotating nuclei by means of quasi-particle diagrams (103–105). The CSM has been extended to three-dimensional cranking (106), but the fundamentals of this latter scheme are still being disputed.

### 3. NUCLEAR SHAPES

Both experimental information and the long experience in mean field calculations tell us that only a few lowest multipolarities are important in the multipole expansion of the nuclear shape. This dramatically facilitates the calculations of equilibrium deformations and the description of the dynamics in the potential-energy landscape. In Section 3.1 we briefly discuss the two commonly used shape parametrizations, the  $\varepsilon$  and the  $\beta$  parametrizations.

Contrary to HF calculations, no real self-consistency is obtained (or required) in the NS approach, i.e. the local density obtained from the calculated wave function does not exactly match the corresponding potential density. It turns out, however, that the NS approach, to an accuracy of a few percent, gives quite a good self-consistency (Section 3.2).

#### 3.1 *Parametrization*

In NS calculations, the nuclear shape is usually parametrized in terms of a multipole expansion:

$$R(\theta, \varphi; \vec{\alpha}) = C(\vec{\alpha}) r_0 A^{1/3} \left[ 1 + \sum_{\lambda\mu} \alpha_{\lambda\mu} Y_{\lambda\mu}(\theta, \varphi) \right], \quad 8.$$

where the coefficient  $C$  assures that the total volume enclosed by the surface in Equation 8 is conserved. The quadrupole part ( $\lambda = 2$ ) is the most important one, and it can be described by only two quadrupole deformation parameters,  $\beta_2$  and  $\gamma$  (e.g. 7, 107):

$$\alpha_{20} = \beta_2 \cos(\gamma) \quad \alpha_{22} = \alpha_{2-2} = -\frac{1}{\sqrt{2}} \beta_2 \sin(\gamma). \quad 9.$$

Furthermore, because of symmetries of Equations 8 and 9, it is sufficient to consider the sector  $\beta_2 \geq 0$ ,  $0^\circ \leq \gamma \leq 60^\circ$  only. Prolate and oblate shapes correspond to  $\gamma = 0^\circ$  and  $60^\circ$ , respectively, and the remaining shapes are triaxial. In the case of (one-dimensional) cranking calculations, the sector  $-120^\circ \leq \gamma \leq 60^\circ$  is required since the nucleus may rotate around any of the three axes. In the Lund convention of  $\gamma$  (100) that we follow here, the rotation takes place around the smallest, the intermediate, and the largest axis in the three sectors  $0^\circ \leq \gamma \leq 60^\circ$ ,  $-60^\circ \leq \gamma \leq 0^\circ$ , and  $-120^\circ \leq \gamma \leq$

$-60^\circ$ , respectively. Noncollective rotation, in which the rotation axis coincides with the symmetry axis, takes place at  $\gamma = 60^\circ$  (oblate shape) and  $\gamma = -120^\circ$  (prolate shape). At axially asymmetric shapes, tensors of order higher than 2 are usually considered in a schematic way only [see (108) for  $\lambda = 3$  and (109–112) for  $\lambda = 4$ ]. When only axially symmetric shapes are considered ( $\mu = 0$ ), we find  $\alpha_{\lambda 0} \equiv \beta_\lambda$ .

In the modified oscillator (MO, Nilsson) potential, the oscillator frequencies rather than the radius are parametrized ( $\varepsilon$  parametrization), and stretched coordinates are introduced (81, 113). This leads to a more complicated expression for the radius, but it offers the possibility of better defining nucleonic configurations in terms of occupied quantum states (cf Section 9.1), since the main oscillator quantum number  $N$  (rather: stretched  $N$ ) is approximately good. Bengtsson et al provide a detailed comparison between the MO and the Woods-Saxon (WS) potentials, stressing similarities and differences (114). In the literature both models are frequently used, and here we refer extensively to both. It is therefore useful to have a transformation between the two kinds of parametrization. In reflection-symmetric shapes, the Nilsson parameters ( $\tilde{\varepsilon}$ ) may be approximately expressed in the  $\beta$  parameters (114):

$$\varepsilon_2 \approx 0.944\beta_2 - 0.122\beta_2^2 + 0.154\beta_2\beta_4 - 0.199\beta_4^2 \quad 10.$$

$$\varepsilon_4 \approx -0.852\beta_4 + 0.141\beta_4^2 + 0.122\beta_2\beta_4 + 0.295\beta_2^2. \quad 11.$$

In HF calculations the shape is usually parametrized in terms of the mass multipole moments. For moderate (axially symmetric) deformations the quadrupole moment may be expressed in the  $\beta_2$  and  $\beta_4$  coordinates as

$$Q_0 \approx 1.09A^{5/3}\beta_2 \left( 1 + \frac{2}{7}\sqrt{\frac{5}{\pi}}\beta_2 + \frac{12}{7\sqrt{\pi}}\beta_4 \right) \text{fm}^2. \quad 12.$$

For large deformations higher multipolarities are needed to describe smooth and realistic nuclear shapes. Still, in most calculations aimed at describing reflection-symmetric axial shapes, only  $\beta_2$  and  $\beta_4$  are included. In Section 8.2 we discuss some attempts to include higher multipole components in the parametrization. For other kinds of shape parameterization, see (74, 88, 91, 115–119).

### 3.2 Shape Consistency in the Nilsson-Strutinsky Approach

Theoretically, the shell correction is expressed in terms of single-particle levels of the deformed shell model and thus depends on the average potential deformation parameters,  $\beta_\lambda^*$ . On the other hand, the macroscopic part describes the bulk properties of the nuclear matter distribution in the

nucleus, and it should depend on the deformation parameters  $\beta_\lambda^v$  of the resulting single-particle density distribution. The improved deformed shell model formula for the total energy (120) reads

$$E_{\text{tot}} = E_{\text{macro}}[\beta^p(\beta^v)] + E_{\text{shell}}(\beta^v). \quad 13.$$

The above equation stresses the fact that the potential deformation  $\beta^v$  is a variational parameter while the physical shape is that associated with  $\beta^p$ . In the simplest version (112, 120–122) the deformation parameters of nucleonic density are calculated from the condition that microscopic and macroscopic multipole moments are equal:

$$Q_{\lambda, \text{macro}}(\beta^p) = Q_{\lambda, \text{shell}}(\beta^v), \quad \lambda = 2, 3, \dots, \lambda_{\text{max}}. \quad 14.$$

Equations 13 and 14 constitute a mathematical expression of the so-called shape consistency condition in the shell correction method. In particular, by means of Equation 14 one can calculate the so-called shape inconsistency, which is defined as  $\delta\beta_\lambda = (\beta_\lambda^v - \beta_\lambda^p)$ . Of course, in the fully self-consistent calculations the HF equation guarantees automatically that  $\delta\beta_\lambda = 0$ . The size of  $\delta\beta_\lambda$  therefore tells us how self-consistent the assumed mean field is with respect to the shape distortion of multipolarity  $\lambda$ . The general properties of the shape inconsistencies of the MO and WS mean fields have been discussed in using the extended Thomas-Fermi method (122). The absolute values of  $\delta\beta_\lambda$  are fairly small (usually not exceeding 5% of the actual deformation value). However, the effect of shape inconsistency may be of some importance when interpreting the results of measurements of the charge multipole moments in terms of the mass multipole moments. For example, for the WS model the quadrupole deformation of charge distribution,  $\beta_2^v$ , is about 10% larger than the calculated equilibrium deformation  $\beta_2^v$ ,  $\beta_2^v = 1.1\beta_2^v - 0.03(\beta_2^v)^3$  (122).

## 4. QUADRUPOLE SHAPES

The quadrupole part of the mean field expansion of the nuclear shape is the lowest-order nontrivial isoscalar moment; it is also the most important part. In this section we briefly review the status of mean field calculations of ground-state axially symmetric shapes (Section 4.1) and triaxial shapes (Section 4.2). Triaxial shapes induced by rotation are discussed in Section 5.

### 4.1 Axially Symmetric Shapes

The transition from spherical to deformed nuclei has been verified experimentally in several mass regions. The experimental fingerprints of nuclear deformation are rotational spectra with low-lying  $2^+$  states, enhanced



E2 transitions, an increase in the root mean square (rms) radius, or a backbending (or upbending) behavior in a plot of the neutron number vs the two two-neutron separation energy.

Mean field calculations are largely facilitated by an imposed axial symmetry since in addition to parity the quantum number  $K$  is preserved (see Table 1). Mean field calculations restricted to axially symmetric shapes have been performed since the mid 1950s. Möller and collaborators performed very extensive NS calculations based on a folded Yukawa average potential (123–125). They computed ground-state deformations, masses, and fission barriers over the periodic table from  $^{16}\text{O}$  to  $^{263}\text{116}$ . Recent systematic calculations restricted to axially symmetric shapes have also been carried out by Ragnarsson & Sheline (126). They utilized the MO potential and discussed different regions of deformation in the whole nuclear periodic table, for example in the neutron-rich Sr-Zr region and in the neutron-deficient Ba region. A “new” island of deformed nuclei has been found in very neutron-rich Na and Mg isotopes with  $N \approx 20$ –22. The onset of deformation in these nuclei can be associated with the occupation of the fp-shell neutron orbits that have a strong tendency to drive toward prolate deformations (127). More dramatic shape effects were seen in some exotic light nuclei, as reviewed by Détraz & Vieira (128). Recent measurements using radioactive beams suggest a dramatic increase of the (reaction) radius in, for example,  $^{11}\text{Be}$  and particularly in  $^{11}\text{Li}$  and  $^{14}\text{Be}$  (129). The former case has been interpreted as a sign of a large deformation (130) (see also Section 5.6.3), while the existence of a “neutron halo” has been suggested to explain the large radius of  $^{11}\text{Li}$  and  $^{14}\text{Be}$  (131).

## 4.2 Triaxial Shapes

The possibility that some nuclei are triaxial in their ground states is a long-standing problem in nuclear structure physics. Davydov & Filippov (132) employed a triaxial rotor model to explain a second low-lying  $2^+$  state in many nuclei. Many calculations based on the particle-plus-rotor model gave a good description of rotational spectra of odd- $A$  nuclei after assuming a nonzero value of  $\gamma$  (e.g. 133). However, it has also been shown by many authors that the experimental data can be reproduced equally well without involving static triaxial shapes but by changing other parameters of the mean field, or by considering dynamical fluctuations in the  $\gamma$  direction by means of collective models.

In the late 1960s Kumar & Baranger (134) performed a set of calculations in the  $(\beta_2, \gamma)$  plane within the pairing-plus-quadrupole model and found indications for strong  $\gamma$  anharmonicity in a number of nuclei. Evidence for triaxial shapes in light nuclei was given by HF (135–138) or HFB calculations (139, 140). The concept of nonaxial shapes was introduced to

the deformed shell model by Pashkevich (141) in the context of fission isomers in actinides. This work was followed by a series of calculations based on the shell correction approach with the MO (109, 113, 142–145) and WS (116, 146) average potentials. Although many nuclei were predicted to have well-pronounced minima at axially symmetric deformations, or to possess low-lying coexisting prolate and oblate minima, in no case was a deep minimum having a finite  $\gamma$  deformation found. On the basis of systematic calculations one can thus conclude that triaxial shapes for medium mass and heavy nuclei are rather rare—if they exist at all.

The best prospects for  $\gamma$  instability are expected in transitional systems with weakly developed quadrupole deformations. From this point of view, the most interesting regions are the nuclei around  $^{74}\text{Ge}$ ,  $^{110}\text{Pd}$ ,  $^{132}\text{Ba}$ , and  $^{158}\text{Os}$ , and indeed there exist some calculations that predict ground-state  $\gamma$  instability (72, 109, 147–153). Predicted triaxial shapes for the  $N < 82$  transitional Sm isotopes were recently supported by observed spectra and electromagnetic transitions (152, 154).

In all the calculations mentioned above, however, the predicted minima are very shallow; the gain in energy due to  $\gamma$  is rather small, of the order of a few hundred keV. What physical interpretation can then be given to such shapes? This problem was illuminated by Hayashi, Hara & Ring (155), who performed three-dimensional angular momentum projection calculations for transitional  $\gamma$ -soft nuclei. Figure 4 shows the calculated

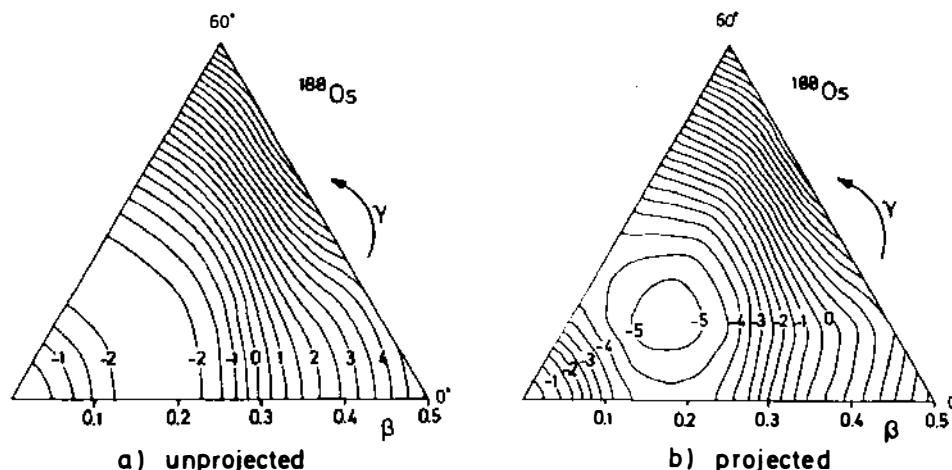


Figure 4 PES in the  $(\beta, \gamma)$  plane for  $^{188}\text{Os}$ . Note how angular momentum projection (*right*) creates the triaxial minimum in the  $\gamma$ -unstable region of unprojected PES (*left*). (From 155.)

PES for  $^{188}\text{Os}$  with and without angular momentum projection. The unprojected surface is  $\gamma$  unstable, and in this case the angular momentum projection has a large effect; the triaxial minimum with  $\gamma \approx 30^\circ$  clearly develops.

## 5. NUCLEAR SHAPES AT HIGH ANGULAR MOMENTA

The shape of the rapidly rotating nucleus was first investigated in the structureless, (rigidly) rotating liquid drop model (RLD) (101). When rotation is imposed, the primarily spherical shape flattens at the poles. The oblate deformation increases with increasing angular momentum until it reaches the Jacobi instability toward triaxial shapes. Heavy nuclei fission along a path of triaxial and large prolate shapes, while nuclei with  $A \lesssim 220$  (or nuclei along the  $\beta$ -stability line) obtain an intermediate sequence of stable triaxial shapes. The angular momentum value that limits fission increases approximately linearly with mass number, reaches a (flat) maximum of about  $95\hbar$  at around  $A \approx 130$ , and decreases to zero at  $A \approx 320$  (still along the  $\beta$ -stability line). A representative PES for a nucleus exhibiting intermediate triaxial shapes,  $^{154}\text{Sm}$ , is seen in Figure 5. Note the very flat energy surface at  $I = 80$ , ranging from  $\varepsilon \approx 0.3$ ,  $\gamma = 60^\circ$  (oblate shape) to  $\varepsilon \approx 0.6$ ,  $\gamma = 0^\circ$  (prolate shape). This indicates that quantal effects ("shell structure") change the RLD picture of nuclear shapes quite drastically at high spins, and local minima at large deformations may appear.

In 1974 Bohr & Mottelson (156) discussed various regimes of the rapidly rotating nucleus, taking quantal effects into account. At a certain spin value the nucleus, which has a prolate ground-state deformation, is expected to undergo a deformation change over triaxial shapes toward an oblate structure of noncollective, irregularly spaced states. This scenario was later confirmed experimentally, as discussed below.

High-spin phenomena, including their impact on nuclear shapes, have been reviewed previously (8, 9, 11, 105, 157–161). Since the latest reviews, remarkable progress has been achieved in several topics, e.g. band termination, shape coexistence, and superdeformation. We therefore concentrate mainly on these recent achievements.

### 5.1 *Centrifugal Stretching*

In the well-deformed nuclei, the observed deviations of the rotational spectrum from the simple  $I(I+1)$  formula provide strong evidence for a modification of the nuclear mean field with increasing angular momentum. This modification can affect either the quadrupole deformation or the pairing gap (or both). In the first study of this phenomenon, Marshalek

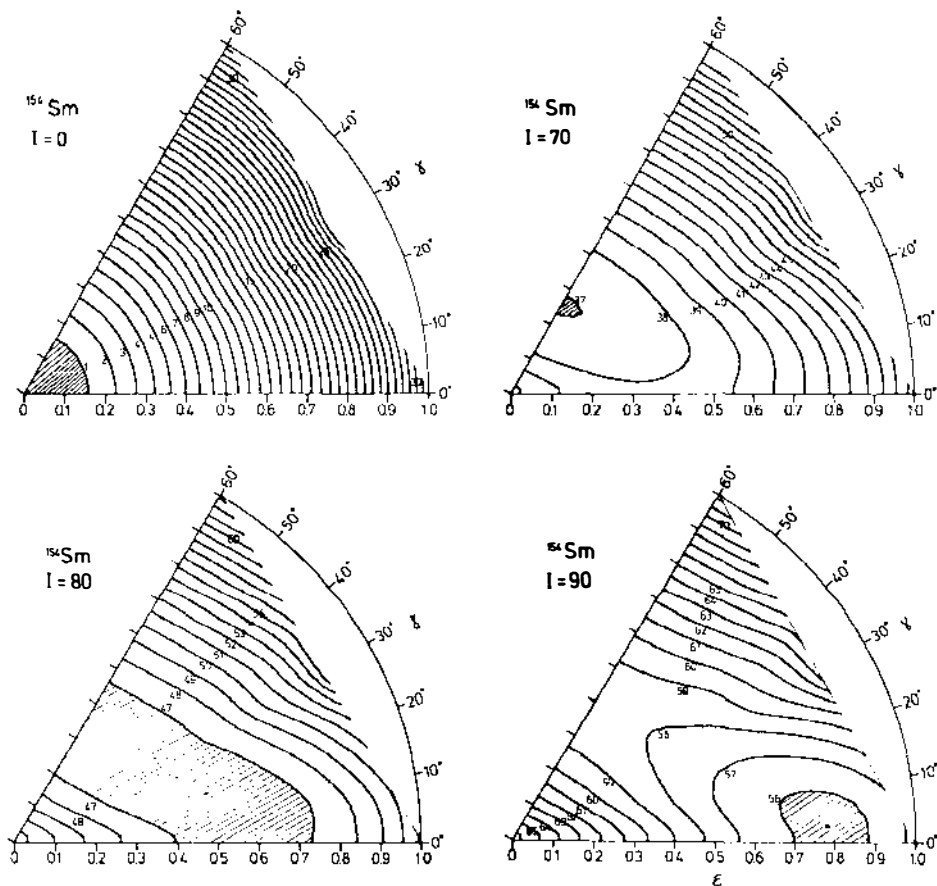


Figure 5 Energy surfaces in the  $(\epsilon, \gamma)$  plane for  $^{154}\text{Sm}$  at angular momenta  $I = 0, 70, 80$ , and  $90$ . Only the macroscopic rotating liquid drop energy,  $E_{\text{RLD}}$ , is plotted; all quantum effects (shell energy) are ignored. (From 100.)

(162) found that the decrease of pairing due to the Coriolis antipairing effect (CAP), is generally stronger than the centrifugal stretching effect. However, these two mechanisms are of equal importance for transitional nuclei from the border of deformed regions. For instance, cranked Nilsson-Strutinsky (CNS) calculations including a full variation over  $\epsilon$ ,  $\gamma$ , and  $\Delta$  (163) found a smooth increase of the deformation between the  $0^+$  and  $10^+$  states of the ground-state band of  $^{160}_{70}\text{Yb}$ : from  $\epsilon = 0.18, \gamma = 0^\circ$  to  $\epsilon = 0.22, \gamma = -5^\circ$ , and a decrease in the pairing gap by about 10%. As can be seen

from Figure 6, the CAP and the centrifugal stretching effects are needed to reproduce the spectra, particularly for nuclei in the transitional region,  $N = 88, 90$  (164). For the sequence of isotopes  $^{164-168}\text{Yb}$ , the variation in the pairing gap is still important, while the quadrupole deformation stays fairly constant up to the  $10^+$  state. The variation of ground-state deformations with particle number explains the angular momentum dependence of the moments of inertia. In the transitional  $N = 88, 90$  nuclei, for example a 10% increase of quadrupole or pairing deformation induces a 350-keV lowering of the energy of the  $8^+$  state. A similar change of deformation or pairing in well-deformed  $N \geq 92$  nuclei ( $\epsilon \approx 0.23$ ) yields only about 50 and 200 keV, respectively. In addition, the deformation changes are favored by the soft PES in the transitional regions.

Other examples of centrifugal stretching can be found in the Os region. CNS calculations utilizing the WS potential predict a considerable stretching in the ground-state band of  $^{176,178}\text{Os}$  (165, 166). For instance, the

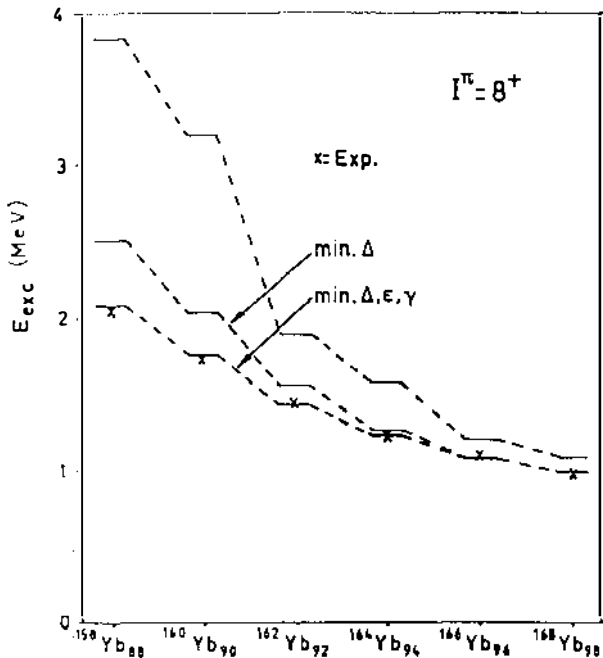


Figure 6 Theoretical (horizontal lines) and experimental (crosses) excitation energies of the  $8^+$  state in  $^{158-168}\text{Yb}$ . The three calculated curves correspond to pairing and deformation coordinates fixed at the  $I = 0$  values (upper line); fixed deformation (middle line); and free minimization with respect to  $\Delta$ ,  $\epsilon$ , and  $\gamma$  (lower line). (From 164.)

deformation of  $^{176}\text{Os}$  increases from  $\beta_2 = 0.22$  at  $\hbar\omega = 0$  to  $\beta_2 \approx 0.26$  at  $\hbar\omega = 150$  keV. In this case the significant stretching becomes possible mainly because of a rather  $\beta_2$ -soft PES.

Experimental evidence for centrifugal stretching can be obtained from measured lifetimes (e.g. 167, 168) or from the values of quadrupole moments deduced from Coulomb excitation measurements. In Figure 7, measured transition ( $Q_t$ ) and static ( $Q_d$ ) quadrupole moments are shown as functions of angular momentum for the isotopes  $^{182,184,186}\text{W}$  (169). The two moments are defined as

$$Q_t \equiv Q_2(I, I-2), \quad Q_d \equiv Q_2(I, I), \quad 15.$$

where

$$Q_2(I_1, I_2) = \sqrt{\frac{16\pi}{5}} (2I_1 + 1)^{-1/2} \frac{|\langle I_2 \| M(E2) \| I_1 \rangle|}{\langle I_1 0 2 0 | I_2 0 \rangle}. \quad 16.$$

Within the (one-dimensional) cranking approximation, a rough relation to the shape variables has been derived (170):

$$Q_t = c\beta_2 \cos(30^\circ + \gamma), \quad Q_d = \sqrt{3}c\beta_2 \sin(30^\circ + \gamma), \quad 17.$$

where  $c = \sqrt{12/5\pi Z e R_0^2}$ . The data for  $^{184,186}\text{W}$  are rather well reproduced by cranking calculations, shown by solid lines in Figure 7 (169). On the other hand, the large difference between the measured and calculated values of  $Q_t$  and  $Q_d$  in  $^{182}\text{W}$  is not explained by the cranking model.

The cranking model values of  $Q_t$  and  $Q_d$  given by Equation 17 are not free from uncertainties. In particular, the triaxial-rotor model predicts  $Q_d$  values that are substantially lower than those obtained within the (one-dimensional) cranking model (171). Largest deviations are found for small  $\gamma$  values and low spins. Onishi et al (171) investigated only the sector  $-60^\circ < \gamma < 0^\circ$  (since the irrotational-flow moments of inertia were utilized), but deviations from Equation 17 are expected for general triaxial shapes. A correct quantum-mechanical treatment of rotational motion should lead to a decrease of the effective  $\gamma$  deformation. In the case of  $^{182}\text{W}$ , taking into account rotation around all three axes would not resolve the discrepancy, since the data appear to require effective  $\gamma$  values larger than those found with ordinary cranking.

Since the moments of inertia in the actinide nuclei are approximately twice as large as in the rare earth systems, rotational perturbation should be less important. This is confirmed by experimental data showing that in the actinide region centrifugal stretching remains weak up to very high spin values (172, 173). Indeed, the cranked HFB calculations by Egido & Ring (174) show no tendency of stretching up to spin  $40\hbar$ .

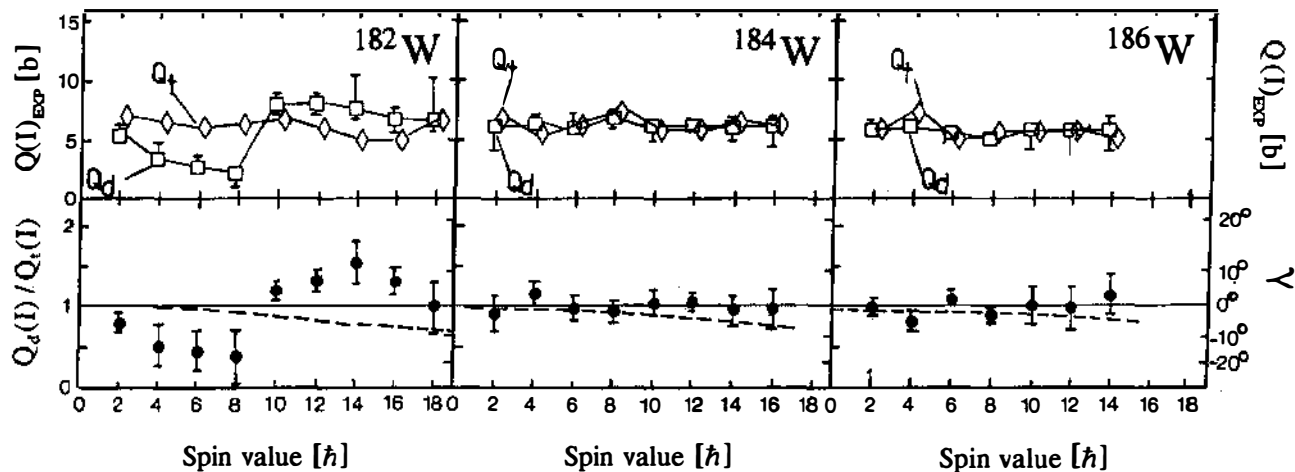


Figure 7 Plot of  $Q_i$ ,  $Q_d$ , and  $Q_d/Q_i$  evaluated from measured E2 matrix elements through Equations 15–17. The dashed line corresponds to equilibrium deformations obtained from cranked WS calculations with pairing. (From 169.)

Recent advances in the field of Coulomb excitation make it possible to measure complete sets of  $E\lambda$  matrix elements for low- and medium-spin states of stable nuclei (175). Using the technique of rotational invariants one can then deduce shape parameters (176, 177). One hopes that this kind of analysis will provide us with rich structural information about deformation changes in rotating nuclei.

## 5.2 Polarization by Decoupled Particle(s)

Interaction between collective rotation and single-particle motion may result in the decoupling of a pair of nucleons that align their angular momentum vectors along the rotation axis. This rotation alignment (RAL) mechanism, suggested by Stephens et al (178), provides the explanation of the backbending phenomenon (179, 180). Of course, the RAL is also expected to change the mean field itself. The first backbending is caused by a change of the rotational band structure from the ground-state band (g-band) to the Stockholm band (s-band). This change is connected by the angular momentum alignment of a pair of nucleons occupying the high- $j$  unique parity states, e.g. an  $i_{13/2}$  neutron pair in rare earth nuclei, or a proton  $i_{13/2}$  pair or a neutron  $j_{15/2}$  pair in actinide nuclei. Thus, because of the blocking effect, the backbending decreases the neutron or proton pair gaps. Figure 8 shows the calculated neutron pairing gap vs rotational frequency in  $^{155,156}\text{Dy}$  (66). The particle alignment [transition from the zero-quasi-particle (0qp) band to the 2qp band, or to the 1qp band in a neighboring odd- $A$  nuclei] is the main reason for the pairing decrease, while a much smaller decrease due to CAP is seen for a configuration

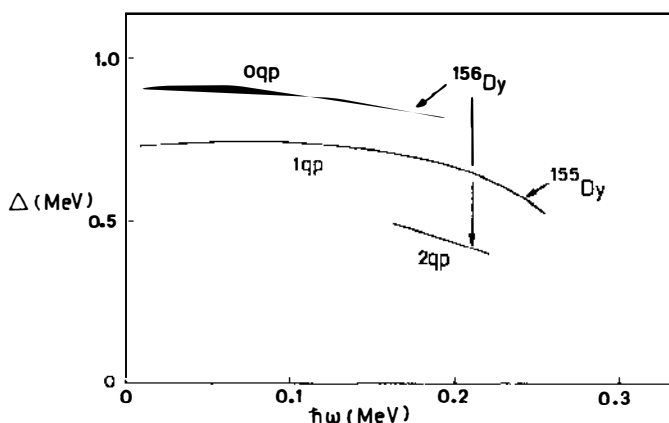


Figure 8 Neutron pairing gaps of  $^{155,156}\text{Dy}$  vs the rotational frequency. Note the strong dependence on the number of excited quasi-particles. (From 66.)



with fixed number of quasi-particles. See recent review articles for more examples (e.g. 181, 182).

In addition, the RAL induces a modification of the quadrupole equilibrium deformation through a polarization of the core. In particular, the alignment of the spins of the decoupled particles along a rotation axis perpendicular to the symmetry axis generates triaxial shapes (156). Frauenthorff & May (183) showed how the position of the chemical potential,  $\lambda$ , affects this tendency of high- $j$  quasi-particles to drive the mean field toward triaxial shapes. When the unpaired quasi-particles occupy one of the lowest levels of a high- $j$  shell, the  $\gamma$  deformation becomes positive; negative  $\gamma$  values are favored by quasi-particle(s) in the upper part of a  $j$  shell. Within a single  $j$ -shell model, Hamamoto & Mottelson (184) derived a simple expression for the favored  $\gamma$  value, which nicely confirms these conclusions,  $\cos(\gamma + 120^\circ) = \frac{3}{2}(\lambda/\Delta e)$ , where  $\lambda$ , is measured from the degenerate (spherical)  $j$  shell and  $\Delta e$  is the total deformation splitting of the  $j$  shell. It is then seen from the above formula that in the bottom of the  $j$  shell the value of  $\gamma = 60^\circ$  is favored while  $\gamma = -120^\circ$  is favored by a particle placed in the upper part of the  $j$  shell. Thus, in the neutron-deficient rare earth nuclei, decoupled  $i_{13/2}$  neutrons drive the shape toward  $\gamma > 0$  (Figure 9, middle) and decoupled  $h_{11/2}$  protons (Figure 9, top) drive toward  $\gamma < 0^\circ$ . By adding the quasi-particle energy, obtained from a CSM calculation, to the energy of the “core,” simply parametrized in the  $\gamma$  and  $\omega$  variables, approximate equilibrium shapes can be obtained for selected 1-, 2-, and 3-quasi-particle configurations (see Figure 9, bottom).

The results of more elaborate cranked Nilsson-Strutinsky (CNS) calculations for the s-band states in  $^{160}\text{Yb}$  including a full variation of pairing and quadrupole ( $\epsilon, \gamma$ ) deformations (163) agree reasonably well with the results of the simple approach. The calculated positive  $\gamma$  values  $\gamma = 5^\circ\text{--}10^\circ$  imply less collective rotation, namely retarded E2 transitions (cf Equation 17). Indeed, longer lifetimes have been measured for s-band states, e.g. in  $^{156,158}\text{Dy}$  (168).

Among other experimental evidence indicating triaxiality generated by a polarization by unpaired nucleons, one can mention signature inversion (185) and the anomalous signature dependence of M1 matrix elements in odd nuclei such as the  $N = 90$  isotones  $^{157}\text{Ho}$ ,  $^{159}\text{Tm}$ , and  $^{161}\text{Lu}$  (see 186). For the latter odd- $Z$  nuclei, the above discussion suggests  $\gamma < 0^\circ$  after the s-band crossing [which is also confirmed by microscopic calculations (187)] in agreement with the analysis in (188, 189).

Shape polarizing effects have also been investigated in the Ce region, where decoupled protons placed in the lower part of the  $h_{11/2}$  subshell drive the deformations toward  $\gamma > 0^\circ$ , and neutrons in the upper part of  $h_{11/2}$  favor negative values of  $\gamma$  (190–195). Thus one expects the proton s-

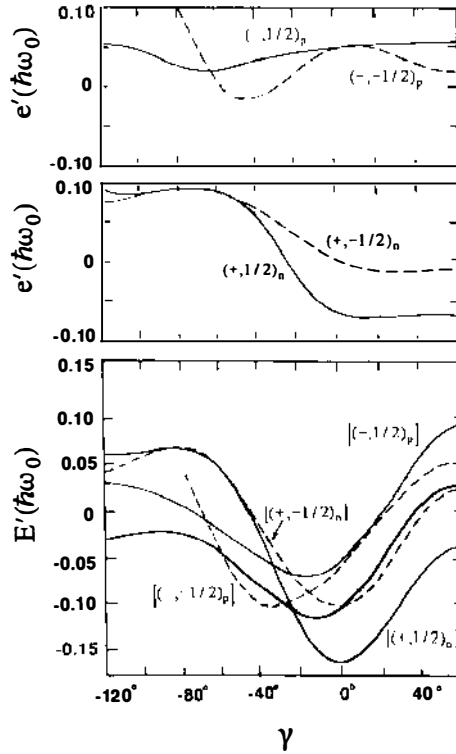


Figure 9 Illustration of  $\gamma$  driving force of quasi-proton (upper part) and quasi-neutron (intermediate part) levels around the Fermi surface for  $Z \approx 68$  and  $N \approx 89$ . The lower part displays total Routhians for indicated configurations. The thick line corresponds to the ground-state configuration. The parameters used are  $\omega = 0.03\omega_0$ ,  $\varepsilon = 0.2$ ,  $\varepsilon_4 = 0$ ,  $\Delta_p = 0.3\hbar\omega_0$  and  $\Delta_n = 0.1\hbar\omega_0$ . (From 183.)

bands to have positive  $\gamma$  values and the neutron s-bands to be associated with negative  $\gamma$  values. CNS calculations based on the Woods-Saxon potential plus a monopole pairing force have been performed for several Ce-Ba-Xe nuclei (194, 195). The predicted equilibrium deformations of ground bands, proton s-bands, and neutron s-bands support these expectations (Figure 10). With increasing neutron number, the  $\gamma$  deformation of the neutron s-band decreases as the Fermi energy rises inside the  $\nu h_{11/2}$  shell. Both types of s-bands have been observed in several Xe-Ce nuclei. On the basis of systematics, and  $g$ -factor measurements, they were assigned as  $(\pi h_{11/2})^2$  and  $(\nu h_{11/2})^2$  (193–195).

A similar situation is expected in medium-mass nuclei from the  $A \approx 80$

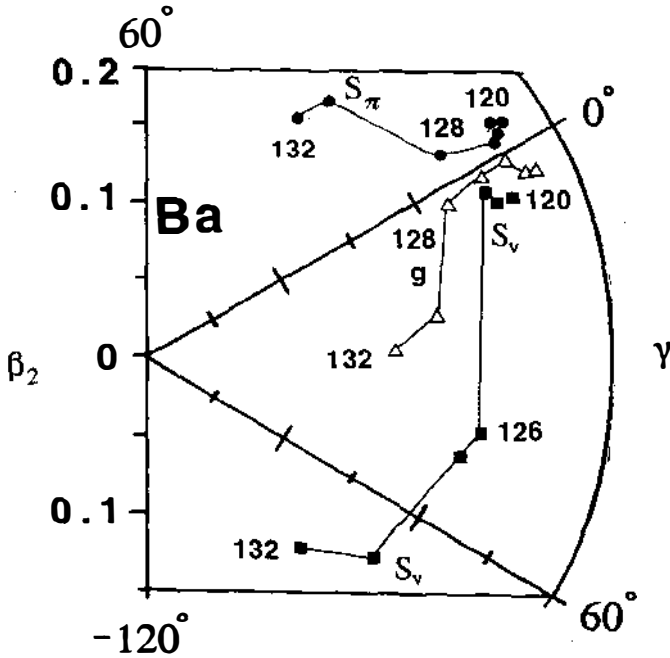


Figure 10 Calculated equilibrium deformations for different configurations in  $^{120-132}\text{Ba}$ : The ground band (triangles), the proton s-band (circles), and the neutron s-band (squares). The calculations have been done with the cranked WS-NS formalism with pairing. (From 195.)

region. In this case both the proton and the neutron Fermi levels lie within the same  $g_{9/2}$  unique parity subshell. It has been observed experimentally, in several odd- $A$  Br, Kr, Rb, Sr, Y, and Zr nuclei with  $N \approx 44$  that the magnitude of the signature splitting changes dramatically at a band crossing (196–201). In several nuclei around  $^{72}\text{Se}$  a low-frequency band crossing has been observed (202). Moreover, quite dramatic shifts in the band-crossing frequency have been seen in many nuclei from the  $A \approx 80$  region (203). All these effects have been interpreted in terms of a deformation change caused by aligned  $g_{9/2}$  particles (for more discussion, see 203–206).

Transitional nuclei from the W-Hg region are also expected to exhibit rather complex shape polarization effects induced by aligned quasi-particles. The neutrons penetrate the upper half of the  $i_{13/2}$  subshell ( $N \approx 106$ ) and then polarize the core toward triaxial or nearly oblate shapes with negative values of  $\gamma$ . The lowest quasi-proton excitations can

originate either from the  $h_{11/2}$  subshell (again, driving the shape toward strongly negative  $\gamma$  values) or they can be built upon the lowest  $h_{9/2}$  and  $i_{13/2}$  intruder states, which have a strong tendency to drive the system toward  $\gamma > 0^\circ$  because of their particle character (see also Section 7.1). Various scenarios of quasi-particle shape polarization in the W-Hg region are discussed elsewhere (165, 166, 207, 208).

The deformation of light nuclei may be drastically altered even by a small modification of the orbital occupation scheme. We review some other aspects specific to the light nuclei below, but first we give an example of various polarization effects in signature partner rotational bands. In a few soft nuclei the occupation of an odd nucleon in the two signature partner states,  $\alpha = 1/2$  and  $\alpha = -1/2$ , leads to very different deformations. This was predicted from cranked Nilsson-Strutinsky calculations for  $^{27}\text{Al}$ , for example (209). In this nucleus, collective rotation favors oblate ( $\gamma = -60^\circ$ ) shapes for the  $7/2^+$  and  $11/2^+$  states ( $\alpha = -1/2$ ), while the  $5/2^+$ ,  $9/2^+$ , and  $13/2^+$  states ( $\alpha = 1/2$ ) have triaxial shapes with the rotation taking place around the smallest axis ( $\gamma \approx -75^\circ$ ). The observed signature splitting provides experimental support for this scenario. At  $\gamma = -60^\circ$  the calculated signature splitting becomes zero, while at  $\gamma = -75^\circ$  it becomes larger than the observed one (see Figure 11). Similar examples of such phenomenon, but in a heavier system, can be found in  $^{79}\text{Ru}$ , where the two 3qp signature partners are believed to have different deformations (210).

### 5.3 Well-Deformed Intruder Bands

The occupation of high- $j$  intruder orbitals (such as  $i_{13/2}$  or  $j_{15/2}$ ) considerably modifies the nuclear deformation through core polarization. For several nuclei around  $^{132}_{58}\text{Ce}_{74}$  the measured quadrupole moments of the excited bands are much larger than those of the ground-state band; these bands are therefore often referred to as “superdeformed” (e.g. 211). The quadrupole moment of an excited band of  $^{132}\text{Ce}$  corresponds to a deformation with  $\beta_2 \approx 0.4$  (212). This agrees well with cranking calculations, which find a mean field  $\beta_2$  close to 0.2 at low spins and  $\beta_2 \approx 0.4$  for  $I \gtrsim 40\hbar$  (Figure 12) (213). The large deformation minimum, which coexists with the smaller deformed minimum at lower frequencies, corresponds to the excitation of two neutrons to well-deformed  $i_{13/2}$  intruder orbitals, which have a strong polarizing effect on the core. The situation is thus quite different from that in the Dy and Hg regions, where superdeformed bands have a much different structure than the low deformed bands (see Section 5.6).

Several CNS calculations with (213) or without (145, 214, 215) pairing demonstrate the appearance of a secondary minimum at  $\beta_2 \approx 0.4$  in nuclei

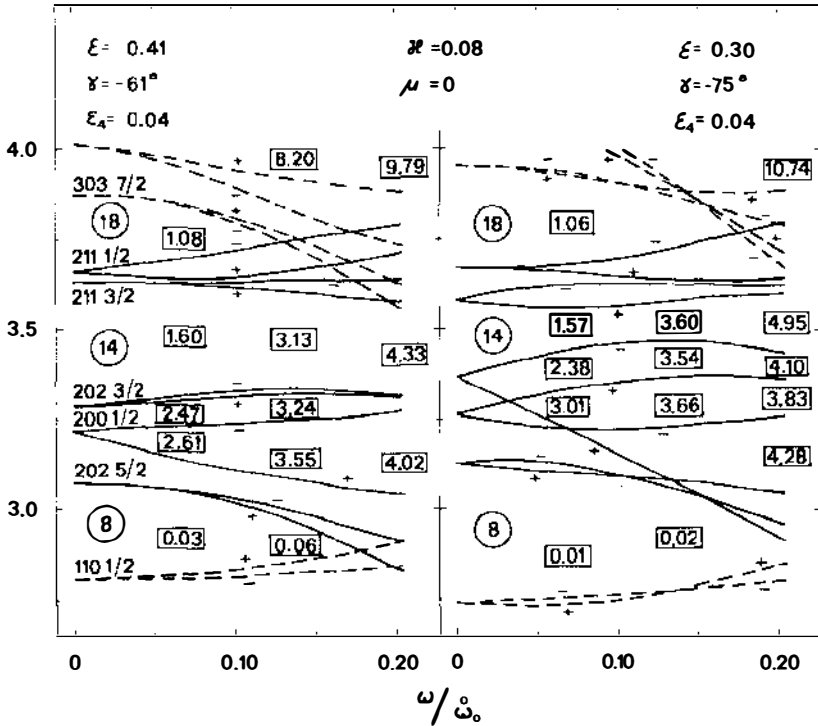


Figure 11 Routhians obtained with the cranked MO potential at deformations representative for the two signature partners of the positive parity band in  $^{27}_{13}\text{Al}_{14}$ . The left side of the diagram is valid for the  $\alpha = -1/2$  sequence and the right side corresponds to the  $\alpha = 1/2$  sequence. (From 209.)

around  $^{132}\text{Ce}$ . Some workers used the MO potential (145, 214) and some the WS potential (213, 216). All these calculations led to similar results, despite some differences in the exact value of the spin at which the  $\beta_2 \approx 0.4$  configuration becomes yrast: the favored shell structure for the large deformation band appears around  $Z = 58-62$ ,  $N \approx 72$ .

There are many other examples of deformation-driving intruder orbitals in different mass regions (217). In the Sr region, for instance, there is a  $[431\ 1/2]$  Nilsson state that at large prolate shapes crosses the  $N = 50$  gap and becomes occupied (199, 218). The measured transition quadrupole moment in the  $[431\ 1/2]$  rotational band in  $^{81}\text{Sr}$  is around 3.5 eb, as compared to the ground-state band transition quadrupole moment,  $Q_t \approx 1.9$  eb (199). Let us also mention the  $\pi i_{13/2}$  rotational bands seen in

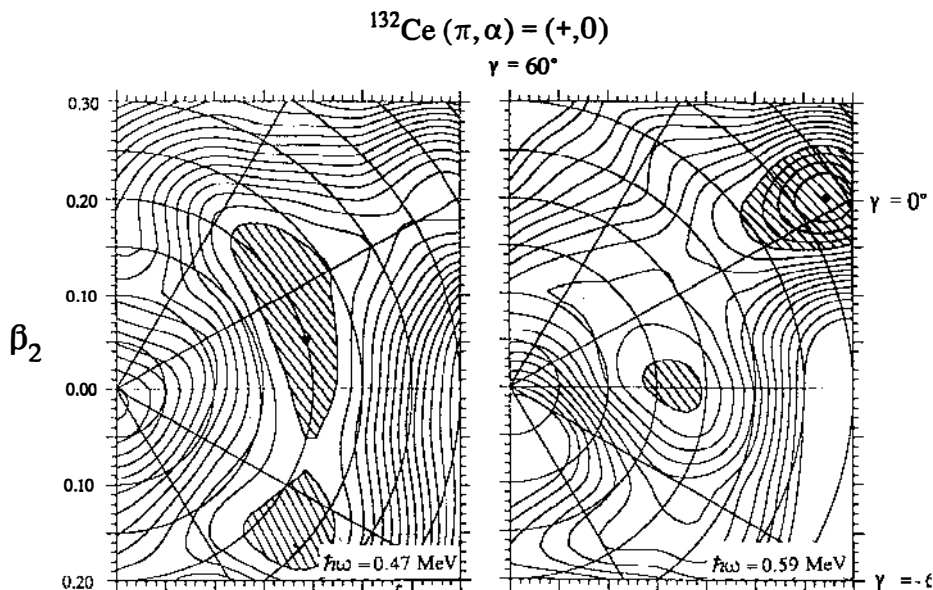


Figure 12 Routhian surfaces (energy in the rotating system at a constant rotational frequency) in the  $(\beta_2, \gamma)$  plane for the  $(+, 0)$  configuration in  $^{132}\text{Ce}$  at  $\hbar\omega = 0.47$  and  $0.59 \text{ MeV}$ . The prolate minimum at  $\beta_2 \approx 0.40$  can be associated with the excitation of two neutrons to the  $i_{13/2}$  subshell. Local minima are shaded. The minimum appearing at  $\gamma \approx -30^\circ$  to  $-60^\circ$  corresponds to the alignment of an  $h_{11/2}$  neutron pair. The absolute minimum for each frequency is marked by a dot and the energy separation between contour lines is  $100 \text{ MeV}$ . (From 213.)

several Ta, Re, Ir, Pt, Au, and Hg isotopes (for a cranked NS analysis, see 166, 219–222). These proton excitations are analogous to the well-deformed intruder states in the Ce region discussed above.

#### 5.4 Band Termination

When all valence nucleons of a given configuration are coupled to a maximum angular momentum, the associated rotational band terminates. To obtain states with higher angular momenta requires drastic rearrangements. The simplest example of a band termination is provided by the ground-state band of  $^{20}\text{Ne}$  built on the  $(sd)^4$  configuration, i.e. a proton and a neutron pair each in  $d_{5/2}$ . In the mean field approach, the highest possible spin [ $8 = 2 \times (5/2 + 3/2)$ ] corresponds to an oblate shape ( $\epsilon = 0.1$ ,  $\gamma = 60^\circ$ ) with the angular momentum vector coinciding with the symmetry axis (209). This contrasts with the prolate deformation ( $\epsilon \approx 0.35$ ,  $\gamma = 0^\circ$ ) of the ground state. The band termination process is thus associated with

a shape change from a collective prolate to noncollective oblate. This modification of the collectivity is evidenced by the experimentally observed drop in the E2 transition matrix elements (cf discussion in 7).

Band termination is not a phenomenon specific to the mean field approach; it is a basic quantum-mechanical property of a few-body system. For this reason it also appears in spherical sd-shell model calculations (223) and in the Elliott SU(3) model (26), thereby providing an interesting connection between the mean field approach and spectroscopic methods that describe nuclear states in terms of a mixing of complicated particle-hole configurations. We discuss such a comparison in more detail below.

In heavier nuclei, the ground-state band does not terminate until very high spins, when it is already very much above the yrast line. However, as originally discussed by Bohr & Mottelson (156), several subsequent spin alignments along the rotation axis tend to create a density distribution symmetric around the rotation axis. This may in some cases ultimately create an oblate shape ( $\gamma = 60^\circ$ ), with the angular momentum being the sum of the contributions from a small number of quasi-particles. Such a prolate-to-oblate shape transition was observed in the first cranking calculations (99, 100). However, the details of the band termination scenario were first discussed by Bengtsson & Ragnarsson, who analyzed the behavior of all individual configurations (223a). In order to follow the evolution of a rotational band to its termination, one must be able to specify a configuration at each point in the deformation and rotation space. Such a formalism (see Section 9.1) was developed and applied to sd-shell nuclei (209) and then extended and applied to medium-heavy nuclei (163, 204, 214; see 224 for more details). In Figure 13 the equilibrium deformations of several different configurations in  $^{158}\text{Er}$  are shown in the  $(\epsilon, \gamma)$  plane at various spin values. In particular, we note the  $\pi(h_{11/2})^4 \nu[(f_{7/2})^3(h_{9/2})^3(i_{13/2})^2]$  and  $\pi(h_{11/2})^4 \nu[(f_{7/2})^4(h_{9/2})^2(i_{13/2})^2]$  configurations (defined relative to the  $^{146}\text{Gd}_{82}$  "core"), which terminate at spins 46 ( $I_p = 16, I_n = 30$ ) and 40 ( $I_p = 16, I_n = 24$ ), respectively. For these configurations the  $^{146}\text{Gd}$  core is not excited, and states below 40 become very  $\gamma$  unstable (cf Section 5 of Ref. 224). The comparison between calculated and measured energies in Figure 13 supports the above configuration assignment of the terminating band.

Band termination can only be observed if the number of valence particles is not too large. Yet the number of particles outside spherical shells must be large enough to allow for a collective rotation at low spins. These requirements are fulfilled for a number of  $N \approx 90$  nuclei, and have been experimentally confirmed also for  $^{158}\text{Yb}$  (225),  $^{156}\text{Er}$  (226),  $^{154}\text{Dy}$  (227),  $^{155}\text{Er}$  (228), and  $^{155}\text{Dy}$  (229). As an additional support for the proposed behavior, measured  $B(\text{E}2)$  values show a rather smooth drop from about

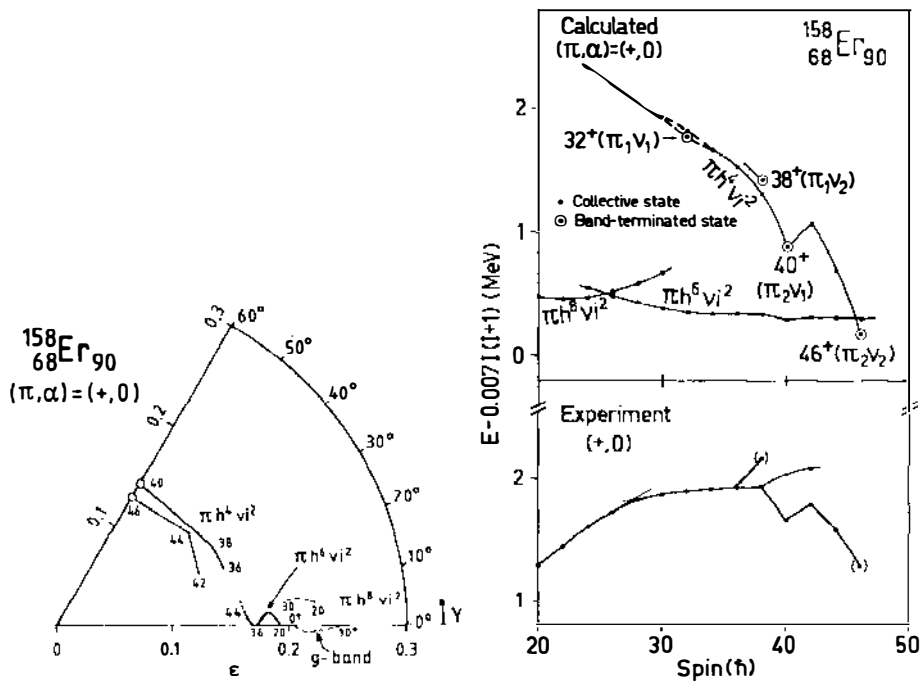


Figure 13 (Left) Calculated equilibrium deformations of  $^{158}\text{Er}$  at spin values between  $0^+$  and  $46^+$ . The cranked MO potential was used and pairing was neglected. The configurations are denoted by the number of particles in  $h_{1/2}$  proton and  $i_{3/2}$  neutron orbitals. (From 223a.)

(Right) Observed and calculated high-spin states with even spins and positive parity of  $^{158}\text{Er}$ . A reference energy of  $0.007I(I+1)$  MeV is subtracted. The configurations are denoted in the same way as in left-hand diagram. Terminated states are labeled by the proton configurations  $\pi_1 = [h_{1/2}]_8^+$  and  $\pi_2 = [h_{1/2}]_{16}^+$  and the neutron configurations  $v_1 = [f_{7/2}^4 h_{9/2}^2 i_{13/2}^2]_{24}^+$  and  $v_2 = [f_{7/2}^3 h_{9/2}^3 i_{13/2}^2]_{30}^+$ . While  $\pi_2$  and  $v_2$  are fully aligned,  $\pi_1$  and  $v_1$  are partly anti-aligned. The rotational band  $\pi h^4 v_i^2$  reaches intermediate band termination states at  $32^+$ ,  $38^+$ ,  $40^+$ . At  $I^\pi = 46^+$  the whole angular momentum available from the valence particles is depleted. (From 224.)

300 Weisskopf units (W.u.) in the g-band to  $\sim 10$  W.u. around band termination (230–233).

Candidates in which one might find band-terminating states in other mass regions are listed elsewhere (224 and references quoted therein).

### 5.5 Noncollective Rotation

By noncollective rotation we mean states in which all angular momentum comes from a few excited nucleons. Noncollective rotation is sometimes



also referred to as “rotation around the symmetry axis.” Examples of noncollective high-spin states are the terminated states discussed above. In these the noncollective state could decay to states within the same configuration and smoothly approach fully collective states within the rotational band. However, for nuclei with a small number of valence nucleons, collective rotation appears to be completely absent, and the yrast line consists of a set of irregularly spaced noncollective many-qp states. Such a sequence has been observed in several nuclei around  $^{146}\text{Gd}$  and  $^{208}\text{Pb}$ .

A simple mean field description of noncollective states has been developed (100, 234). The energy and angular momentum for each many-particle-many-hole (or many-qp) configuration are calculated as

$$E(I^\pi) = \min_{\beta} \left\{ \sum_{i \in \text{part}} e_i + \sum_{k \in \text{holes}} e_k + E_{\text{shell}} + E_{\text{LD}} \right\} \quad 18.$$

$$I = \sum_{i \in \text{part.}} m_i - \sum_{k \in \text{holes}} m_k,$$

where the  $e_i$  and  $m_i$  denote the single-particle energies and angular momenta along the symmetry axis. The energy  $E_{\text{shell}}$  is defined as the  $I = 0$  Strutinsky shell energy, and  $E_{\text{LD}}$  is the liquid drop energy. All quantities in Equation 18 depend on the deformation parameters,  $\beta$ . As expected, this model predicts that the aligned valence particles generate an oblate shape, in contrast with the prolate shape that results from an alignment of hole orbitals (235, 236). The deformation increases with the number of aligned particles. One thus generally expects deformation to increase along the yrast line, as a result of the core polarization. When the pairing force is of importance, the stretching may be further accentuated by the CAP effect (237). To reach angular momenta higher than available from the valence particles, one must create core excitations, which in turn generate an additional increase of the deformation (236, 238, 239). Figure 14 shows calculated (239) and measured (240) electric quadrupole moments for some isomeric high-spin states in  $^{147}_{64}\text{Gd}_{83}$ . Since this nucleus has only one neutron outside the spherical “core,” core excitations are necessary to obtain the states with  $I > 13/2$ . The  $49/2$  state corresponds to a deformed shape,  $\beta_2 = -0.17$ . The larger deformation for the  $49/2$  state is explained by the additional breaking of the neutron core. This modification of the internal structure gives rise to a substantial  $\gamma$ -decay hindrance, which results in a lifetime of 510 ns for the  $49/2^+$  state.

As mentioned above, several nuclei around  $^{208}\text{Pb}$  also display irregular, noncollective yrast lines. The importance of self-consistency in defor-

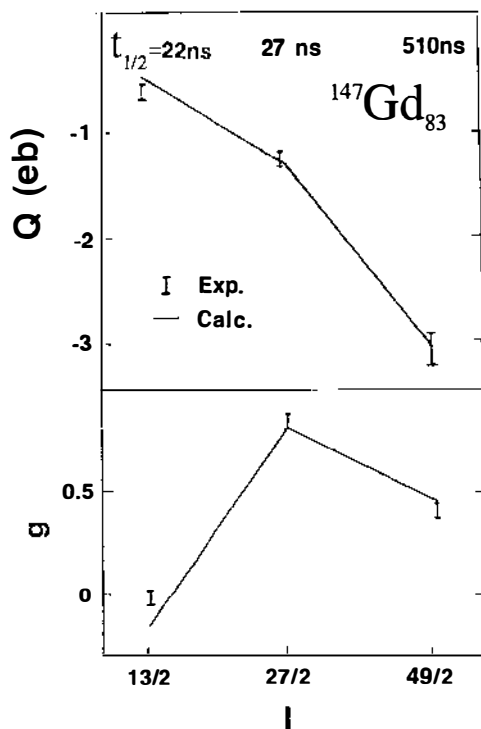


Figure 14 Quadrupole moments  $Q$  and gyromagnetic ratios  $g$  of three isomers in  $^{147}\text{Gd}$  with  $I = 13/2$ ,  $27/2$ , and  $49/2$ . The isomers are assigned as  $\nu 1_{13/2}$ ,  $\nu[f_{7/2}\pi(d_{5/2}^{-2})_0 h_{1/2}^2]$ , and  $\nu[(d_{3/2}^{-2})_0 f_{7/2} h_{9/2} i_{13/2}] \pi[(d_{5/2}^{-2})_0 h_{1/2}^2]$  relative to a  $^{146}\text{Gd}$  core. (From 239.)

mation is shown in Figure 15, where the noncollective spectrum of  $^{212}\text{Rn}$ , calculated with a deformation minimization, is compared to the spherical and the experimental spectra. The minimization with respect to shape parameters induces a deformation increase from  $\varepsilon = 0$  at  $12^+$  to  $\varepsilon = -0.1$  at  $30^+$ , resulting in a more compressed spectrum in good agreement with experiment. The general features of Figure 15 reveal the importance of the long-range quadrupole residual interaction. However, to get a correct description of, for example, the  $30^+$  state in  $^{212}\text{Rn}$  concerning transition rates,  $g$ -factors, etc, the pure mean field approach is insufficient and it becomes necessary to include residual interactions, particularly a coupling to collective octupole phonons (240a). A discussion of the relation between deformation effects and residual interactions in the spherical shell model in the description of noncollective states can be found in (238).

Several other mean field calculations of noncollective spectra have been

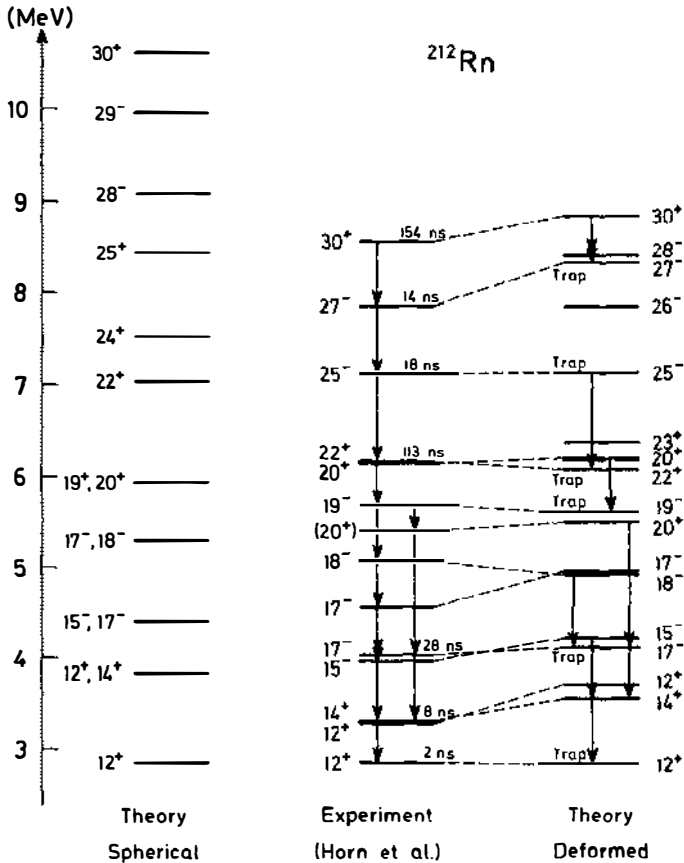


Figure 15 Experimental and calculated levels with  $I \geq 12$  in  $^{212}\text{Rn}$ . In the left-hand spectrum, the nucleus is constrained to spherical shape, while a free minimization with respect to the deformation coordinates  $\varepsilon$  and  $\varepsilon_4$  is performed in the right-most spectrum. The minimization results in a smooth increase of the deformation from  $\varepsilon = 0$  at  $I = 12$  to  $\varepsilon = -0.1$  at  $I = 30$ . The notation "trap" is given whenever a state cannot decay with E1, M1, E2, or M2 transitions. (From 236.)

performed in the  $A \gtrsim 150$  region (228, 241–245) as well as in the Pb region (246, 247; see also 159).

The so-called  $K$ -isomeric states of some Hf and W isotopes are of the same nature as the noncollective states discussed above. Indeed, although this is a region of well-deformed prolate nuclei (with low-lying collective rotational bands), the total spin of these  $K$ -isomeric states is the sum of

many-particle-many-hole (or many-qp) contributions. On the other hand, theoretical investigations performed within the approach described above show that a correct reproduction of these states depends much more on a good account of pairing effects than on deformation degrees of freedom (236, 248, 249).

$^{24}\text{Mg}$  provides another example of coexisting collective and non-collective rotation. Despite the small number of nucleons, a collective rotational band has been observed up to  $8^+$ . The  $10^+$  and a  $12^+$  states have also been tentatively assigned. Below the  $K = 0$  rotational band, a  $K^\pi = 8^+$  state is observed, which decays to the yrast  $6^+$  states with an E2 strength more than ten times smaller than the intraband strength. Mean field calculations within either the cranked HF + BCS method (using a Skyrme interaction and monopole pairing) (250) or the cranked NS model (209) are able to reproduce this coexistence. Both approaches give very similar results, but although they provide a qualitative understanding of the observed spectrum, the calculated moment of inertia comes out about 30% too large. In all likelihood, this difference cannot be attributed to the missing  $T = 1$  pairing correlations. Indeed, the discrepancy in the moment of inertia is nearly constant along the band. The inclusion of a neutron-proton ( $T = 0$ ) particle-particle interaction may, however, account for the discrepancy (cf Section 8.1).

A comparison between the cranked NS and spherical shell model wave functions provides an interesting insight into the physical content of the mean field approach. Since the matrix elements of the residual interaction used in the shell model are adjusted to the experimental data, the agreement with measured quantities is often excellent. To compare the structure of the wave functions one can calculate in both models the  $j$ -shell occupancies of different orbitals (251). The spherical occupation numbers (Figure 16) are drastically changed by the residual interaction, whether it is described by the experimentally adjusted two-body matrix elements (Preedom-Wildenthal interaction) or by the deformed and rotating mean field. The results are amazingly similar. The major difference results from technical limitations of the shell model, which in this calculation prevented the occupation of orbitals beyond the sd shell. The other minor differences might provide clues for future improvements of the phenomenological parameters used in the NS description of light nuclei.

The mean field “construction” of the noncollective states by the “oblate coupling scheme” is well adapted to the completely aligned configurations discussed above, such as a  $10^+$  state built on the  $(h_{11/2})^2$  configuration. On the other hand, this simple method cannot be applied with the same success to states that correspond to partially aligned configurations (252). For example, some of the predicted states must be eliminated for symmetry

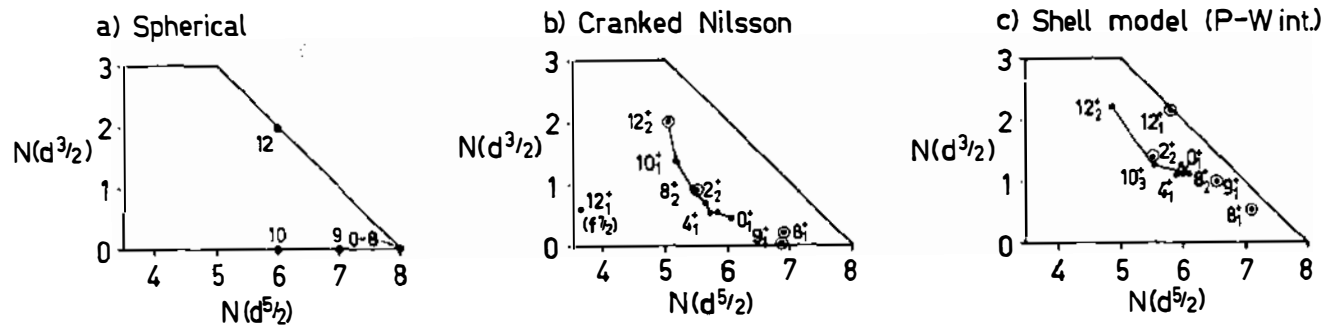


Figure 16 Average number of particles occupying the spherical  $d_{3/2}$  and  $d_{5/2}$  shells for different states in  $^{24}\text{Mg}$ . The three portions show the results from calculations utilizing a pure spherical shell model (excluding residual interactions), a CNS model, and a shell model with the Freedman-Wildenthal interaction. (From 251.)

reasons [e.g. the odd spins in the  $(h_{1/2})^2$  multiplet]. In addition, the partially aligned configurations calculated within this method are generally too excited as compared to experiment. Finally, a correct treatment of the angular momentum coupling is expected to result in a much more complex structure of the wave functions than the one given by the simple de-alignment of just one particle.

## 5.6 Superdeformations

One of the most spectacular achievements in nuclear structure physics has been the discovery of superdeformed rotational bands. In 1985 Twin et al (253) at the Daresbury Laboratory found a very regular pattern of closely spaced  $\gamma$  transitions in the spectrum of  $^{152}\text{Dy}$ , which they assigned to a rotational cascade between levels of spin ranging from  $60\hbar$  to  $24\hbar$  and excitation energy varying from  $\sim 30$  to  $\sim 12$  MeV. The moment of inertia of the associated band was found to be close to that of a rigid rotor with a 2:1 axis ratio. Later on, lifetime measurements brought additional support to this assumed large deformation (254). The experimental situation was recently reviewed by Nolan & Twin (211).

The discovery of a superdeformed band was preceded by many predictions based on calculated PES at high spin (97–100). The existence of the 2:1 deformed shape had certainly been established long ago with the observation of fission isomers in actinide nuclei (86; see 88 for a review), and there also existed some theoretical indications of the superdeformed favorable shell structure in nuclei around  $^{152}\text{Dy}$  (80). The essentially new idea emphasized by the cranking calculations was that rotation provided the practical tool to stabilize the very deformed configurations. Another main theme was that quantal (shell) effects would survive and influence the structure even at the most rapid rotations sustainable by the nuclear system.

Since its discovery in 1985, superdeformation has become one of the most active subfields of nuclear structure, both experimentally and theoretically. These efforts have thus far been rewarded by the identification of about 20 different superdeformed bands in nuclei around  $^{152}\text{Dy}$ . More recently, a new region of superdeformation was found around  $^{194}\text{Hg}$  (255). These data greatly increase our knowledge of the nuclear structure properties at these extreme deformations. Before we describe the predictions of deformed exotic shapes in other mass regions, we review the status of mean field calculations for superdeformations in the  $^{152}\text{Dy}$  and  $^{194}\text{Hg}$  regions.

**5.6.1 THE  $^{152}\text{Dy}$  REGION** The experimental information confirms the magic character of the numbers  $N = 86$  and  $Z = 66$  at the 2:1 deformation,

which had been predicted as early as 1980 (256). A detailed discussion of the properties of the superdeformed minimum around  $^{152}\text{Dy}$  is available elsewhere (257–265, 265a). The shell-energy diagram of Figure 17 shows minima for approximately these two particle numbers at the 2:1 deformations ( $\varepsilon = 0.6$ ). (To see the true character of the  $N = 86$  and  $Z = 66$  gaps, an explicit minimization of the  $\varepsilon_4$  degree of freedom has to be performed.) Because of the persistence of these minima at high spins (combined with the large moment of inertia), the superdeformed band becomes yrast at  $I \gtrsim 50\hbar$ . The measured superdeformed band in  $^{152}\text{Dy}$  is shown in Figure 18, together with two coexisting structures: oblate noncollective and a prolate collective one (253). These three types of rotation can be associated with distinct minima in the PES of CNS calculations of Figure 18 (262). In Figure 19, which shows single-particle energies obtained from the cranked WS potential (265) vs rotational frequency at the 2:1 deformation ( $\beta_2 = 0.62$ ,  $\beta_4 = 0.12$ ), one sees that the  $N = 86$  and  $Z = 66$  gaps persist to high frequencies. A similar picture emerges from the cranked MO potential (262, 266).

As with ordinary doubly magic nuclei, one expects several rotational bands in neighboring nuclei associated with the low-lying one-particle or one-hole states. This expectation is confirmed by the data: in  $^{152}\text{Dy}$  only one superdeformed band has been observed while three superdeformed bands (most probably very close in energy) have been identified in  $^{153}\text{Dy}$  (267). Because of the large shell gaps, one also expects a rather small density of rotational bands at an excitation energy for several MeV above yrast in  $^{152}\text{Dy}$  (268).

In Figure 19 several high- $N$  orbits (i.e.  $N = 7$  neutrons and  $N = 6$  protons) appear in the vicinity of the Fermi surface. These orbits, which at normal deformations are only occupied in actinides (see Figure 2), play a major role in the structure of the different superdeformed bands (263). While other levels are only weakly affected by rotation, the Routhians of these high- $N$  bands correspond to large intrinsic angular momentum (since they originate from  $\pi i_{13/2}$  and  $\nu j_{15/2}$  high- $j$  spherical orbitals). Their curvature versus  $\hbar\omega$  is also large and dependent upon the state (see Figure 20). The cumulated curvature of all occupied orbitals corresponds to the so-called second moment of inertia, given by

$$\mathcal{J}^{(2)} = \frac{dI}{d\omega} = - \sum_{\text{occ.}} \frac{d^2 e^\omega}{d\omega^2}. \quad 19.$$

Figure 21 shows the evolution of experimental  $\mathcal{J}^{(2)}$  moments of inertia in superdeformed bands versus rotational frequency:

$$\mathcal{J}_{\text{exp}}^{(2)} = 4/\Delta E_\gamma; \quad \omega_{\text{exp}} = \frac{1}{2}E_\gamma. \quad 20.$$

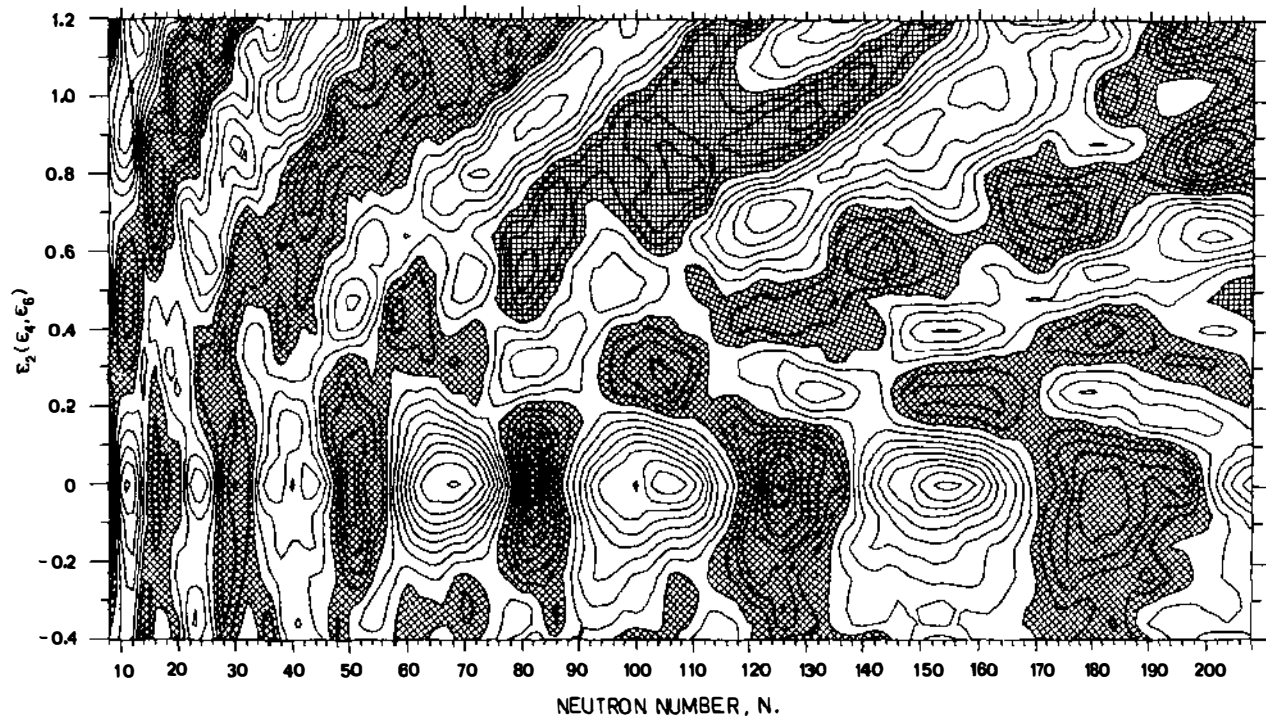


Figure 17 Shell energy diagram in the  $(\epsilon_2, N)$  plane. The term  $\epsilon_2$  depends explicitly on  $\epsilon_4$  and  $\epsilon_6$  in such a way as to approximately minimize the liquid drop energy. Areas corresponding to negative shell energy are shaded, and the contour separation is 1 MeV. (From 126.)



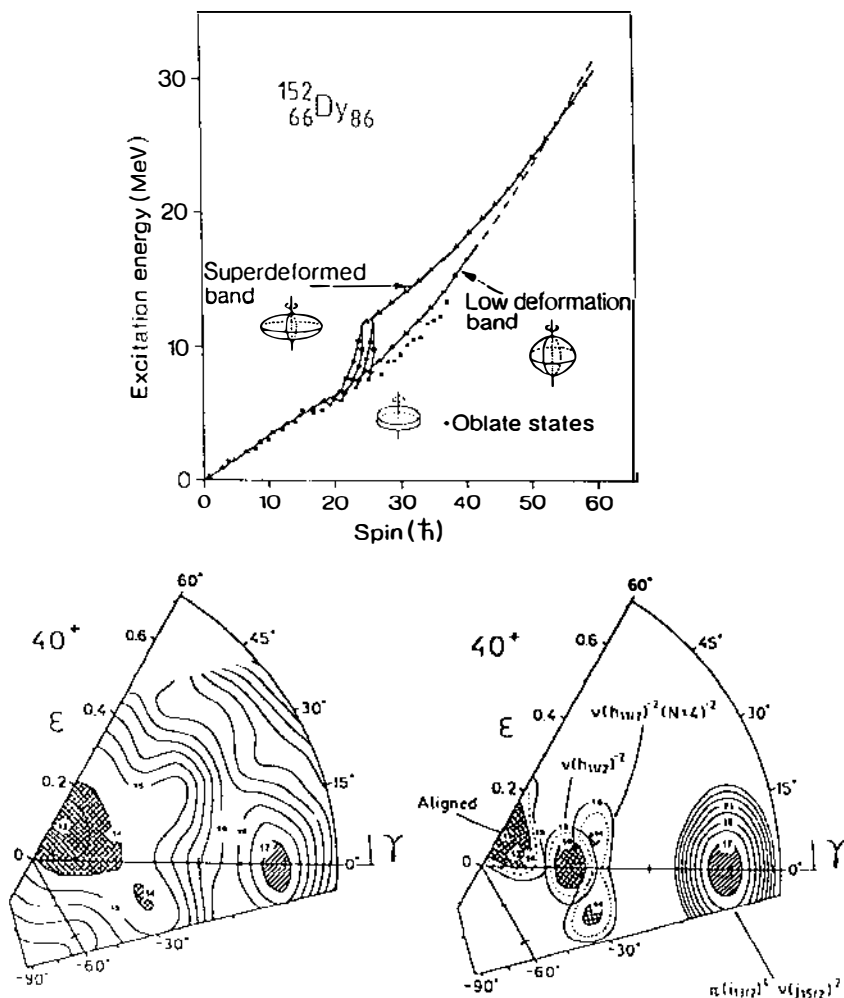


Figure 18 The three coexisting structures observed in  $^{152}\text{Dy}$  (upper part)—oblate non-collective states, low-deformation band, and superdeformed band—have their correspondence in calculated PES (lower part). In the right-hand side the constraints have been made on occupied configurations (cf Section 9.1) while the left-hand side represents the PES with constraint only on parity ( $\pi = +$ ) and signature ( $\alpha = 0$ ) quantum numbers. (From 262.)

The behavior of various  $\mathcal{J}^{(2)}$  in several nuclei is theoretically well understood in terms of different occupations of the high- $N$  orbits (263, 265, 265a, 266). Changing the high- $N$  occupation changes the  $\mathcal{J}^{(2)}$  behavior, as approximated in Figure 20.

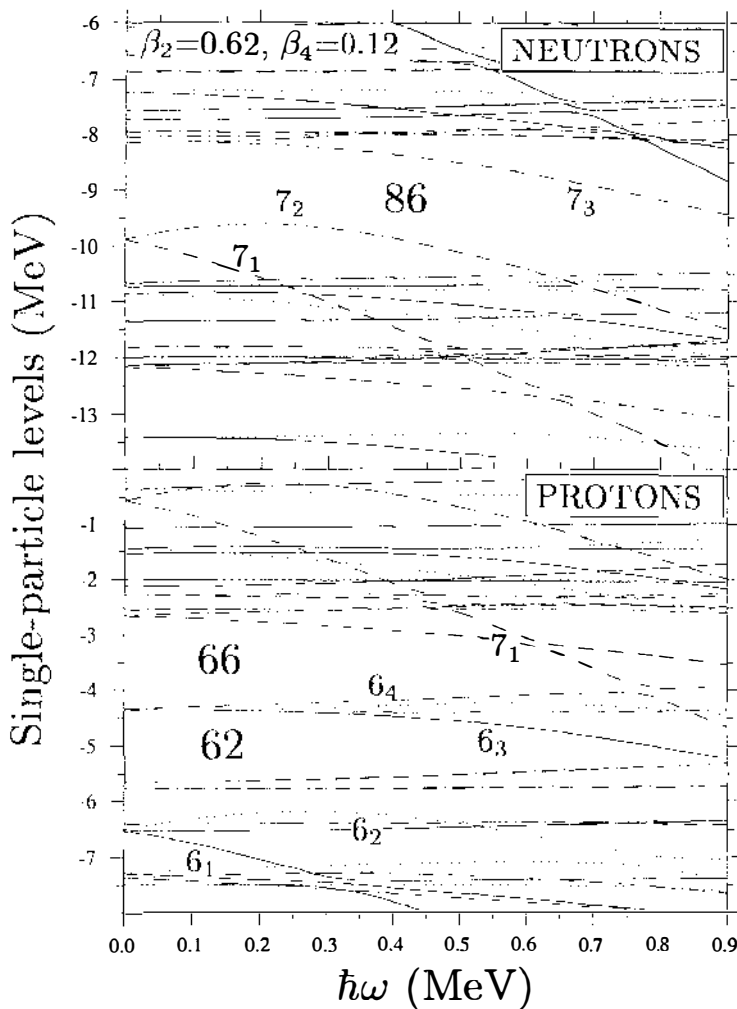


Figure 19 WS single-particle superdeformed energies in the rotating frame vs rotational frequency for neutrons and protons at the superdeformed minimum,  $\beta_2 = 0.62$ ,  $\beta_4 = 0.12$ . The following line convention was used: solid ( $\pi = +$ ,  $\alpha = 1/2$ ), dotted ( $+$ ,  $-1/2$ ), dot-dashed ( $-$ ,  $1/2$ ), and long-dashed ( $-$ ,  $-1/2$ ). The lowest high- $N$  orbits, originating from the  $i_{13/2}$  ( $N = 6$ ) and the  $j_{15/2}$  ( $N = 7$ ) subshells, are indicated. (From 265.)

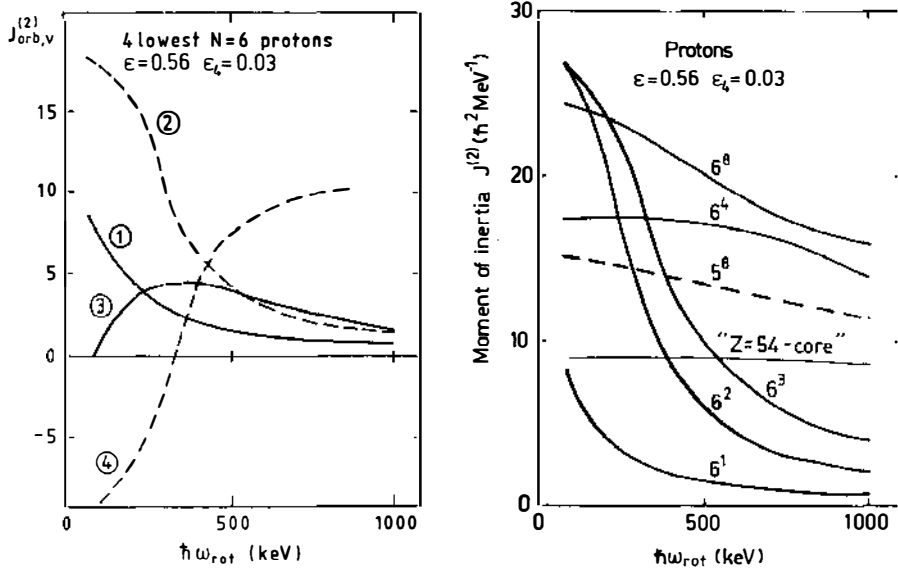


Figure 20 Contributions to the dynamical moment of inertia  $\mathcal{J}^{(2)}$  from high- $N$  orbits around the Fermi surface in superdeformed nuclei around  $^{152}\text{Dy}$ . Single-particle contributions from the four lowest  $N = 6$  orbitals are shown in the left-hand part, and the right-hand part refers to various configurations with  $n$  particles in an  $N$  shell. (From 263.)

Since high- $N$  orbits carry a rather large single-particle quadrupole moment, their occupation (or depletion) is bound to affect the equilibrium deformations. The experimental values of charge quadrupole moments (from lifetime measurements) of  $^{152}\text{Dy}$ ,  $^{149}\text{Gd}$ ,  $^{150}\text{Gd}$ , and  $^{146}\text{Gd}$  are 19, 17, 17, and 12 eb, respectively (254, 269, 269a, 270). These numbers are in good agreement with the calculated equilibrium deformations (265, 266). The deformation decrease of the superdeformed band when neutron number changes from  $N = 86$  to  $N = 82$  can also be seen in the shell-energy diagram of Figure 17.

The mean field approach should correctly take into account the modifications of the pairing gap as well as the level ordering induced by the deformation variations. While pairing seems to play a minor role in the superdeformed band of  $^{152}\text{Dy}$  [it has a dynamic character (271, 272)], the lower part of the superdeformed band in  $^{150}\text{Gd}$  is presumably affected by pairing. The large increase of  $\mathcal{J}^{(2)}$  in the lower part of the superdeformed band in  $^{150}\text{Gd}$  [see (269a) and Figure 21] has been interpreted as an alignment of the  $N = 7$  neutron pair resulting in a modification of the

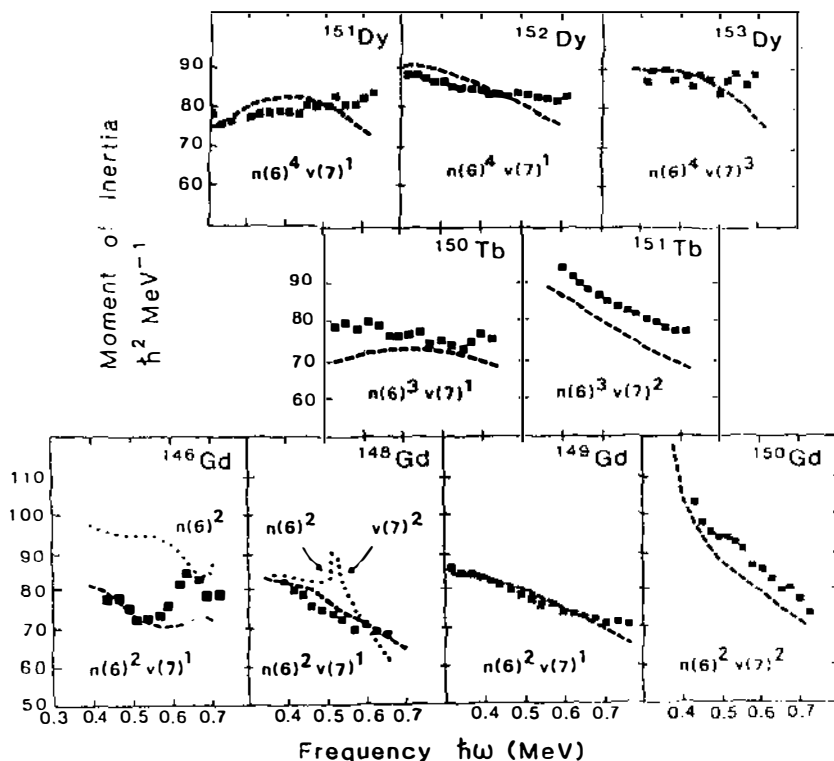


Figure 21 Experimental  $J^{(2)}$  values vs  $\hbar\omega$  for superdeformed bands in  $A \approx 150$  nuclei. For comparison the calculated quantities are also shown (265). The number of particles in proton  $N = 6$  and neutron  $N = 7$  orbits is indicated. [From 497 and 270 ( $^{146}\text{Gd}$  data).]

configuration from  $\pi 6^2 \nu 7^0$  to  $\pi 6^2 \nu 7^2$  (264, 265). An interesting band crossing has been observed at  $\hbar\omega \approx 650$  keV in the superdeformed band of  $^{146}\text{Gd}$  (270). This might be explained by an unpaired band crossing between the two Nilsson orbitals  $\nu[651 \frac{1}{2}]$  and  $\nu[642 \frac{5}{2}]$ . Although the same configuration has been assigned to  $^{148}\text{Gd}$ , such a band crossing has not been seen there (see Figure 21). This is attributed to single-particle rearrangements caused by the larger deformation of  $^{148}\text{Gd}$  (270).

**5.6.2 THE  $^{192}\text{Hg}$  REGION** Recently some superdeformed bands were observed in  $^{191,192,193,194}\text{Hg}$  (255, 273–276), and in  $^{194}\text{Pb}$  (277). In this mass region ( $N \approx 114$ ,  $Z \approx 80$ ) the superdeformations are somewhat smaller ( $\epsilon_2 \approx 0.5$ ) than around  $^{152}\text{Dy}$  ( $\epsilon_2 \approx 0.6$ ). Here, too, the experimental discovery was preceded by several theoretical analyses that showed the exis-

tence of a superdeformed minimum, even at  $I = 0$  (37, 116, 278, 279) that becomes stabilized by rotation (145, 208, 214, 273, 280–282). The  $I = 0$  excitation energy predicted by various models varies between 4 and 7.5 MeV. The persistence of a well-marked minimum in the PES down to spin  $I = 0$  is an important difference between the superdeformed states in this mass region and those in nuclei near  $^{152}\text{Dy}$ . It is, however, important to note that all of the observed superdeformed bands in the Hg region depopulate completely below spin 8 or 10.

The measured  $\mathcal{J}^{(2)}$  moments of inertia in the superdeformed band from the Hg region increase with  $\omega$ , see Figure 22 (a behavior opposite to that observed in the  $^{152}\text{Dy}$  region). This has been explained by a paired band crossing with a  $\nu(j_{15/2})^2$  band followed by a gradual  $\pi(i_{13/2})^2$  alignment, i.e. a smooth transition from a superdeformed ground-state band to a

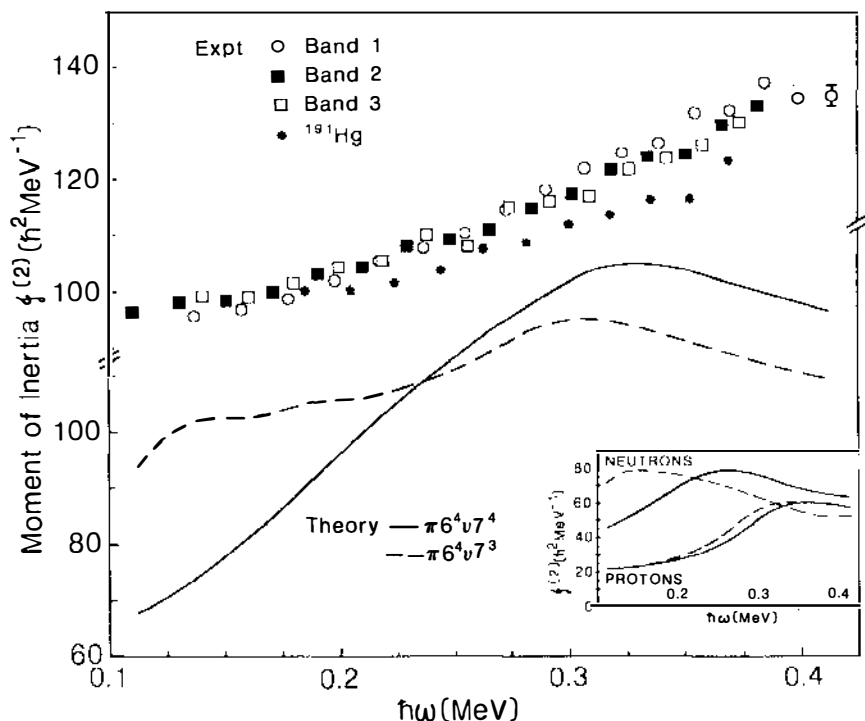


Figure 22 Experimental  $\mathcal{J}^{(2)}$  values vs  $\hbar\omega$  for superdeformed bands in  $^{194}\text{Hg}$  (three bands) and  $^{191}\text{Hg}$  (one band). For  $^{194}\text{Hg}$  the calculated values are shown for the two different configurations,  $\pi 6^4 \nu 7^4$  and  $\pi 6^4 \nu 7^3$ . The contributions to  $\mathcal{J}^{(2)}$  coming from protons and neutrons are shown in the inset. (From 273.)

neutron and proton s-band (273). However, probably because of reduced neutron pairing and a large  $Z = 80$  gap, these crossings induce only a very smooth increase of  $\mathcal{J}^{(2)}$  and the two alignments cannot be distinguished. Yet we know that above the band crossing the  $\mathcal{J}^{(2)}$  moment of inertia should decrease, i.e. it reaches a maximum at the crossing point. Assuming the  $\mathcal{J}^{(2)}$  background to be constant, one expects the maximum around  $\hbar\omega \approx 0.4$  MeV. The verification of this prediction would provide strong support to this theoretical analysis of the  $\mathcal{J}^{(2)}$  behavior.

According to the theoretical interpretations there is a structural difference between superdeformed bands in the  $^{192}\text{Hg}$  and the  $^{152}\text{Dy}$  regions. In the Dy region the observed portion of the superdeformed band has an "s-band" character, i.e. the  $N = 7$  neutrons and  $N = 6$  protons are already aligned. In fact, the de-alignment process, which explains the increase in  $\mathcal{J}^{(2)}$  at the lowest frequencies observed in some cases, might be connected to the rather rapid depopulation of intensity. In the Hg region, on the other hand, the observed part of the superdeformed band can be viewed as a strong mixture of the g-band and two s-bands.

**5.6.3 LIGHT NUCLEI** The application of the Strutinsky method to light (p- and sd-shell) nuclei may be a rather bad approximation to the self-consistent Hartree-Fock method, since the contribution from the higher-order terms in Equation 7 may be rather large (283). Still, it has proven to be quite useful in identifying minima in potential-energy surfaces for light nuclei with experimental states (144, 256, 284); in fact, very similar results emerge from both Hartree-Fock and Nilsson-Strutinsky calculations (250).

A particular feature of light nuclei is that the rearrangement of one or a few particles may drastically change the shape. If nuclei with an axis ratio of 2:1 or larger are considered as superdeformed, several light nuclei certainly belong to this group, and some of them even have superdeformed ground states. For example, the ground state of  $^8\text{Be}$  may be described in terms of a prolate 2:1 deformation (two alpha particles), and the ground state of  $^{12}\text{C}$  corresponds to an oblate 2:1 deformation (three alpha particles in a triangle) (144, 256). But the most exotic ground-state shape may be found in  $^{11}\text{Be}$ , which is calculated to be superdeformed and triaxial ( $\varepsilon = 0.65$ ,  $\gamma = 40^\circ$ ) (256). This calculated very large deformation may explain why the  $1/2^+$  ground state has unnatural parity, and it may also account for the measured (129) large root mean square radius (130).

Several light nuclei have excited superdeformed states. If proton and neutron pairs in  $^{12}\text{C}$  are excited from the p shell to the sd shell, a shape emerges that resembles three  $\alpha$  particles in a row, i.e. a 3:1 deformation ( $\varepsilon \approx 1.0$ ,  $\gamma = 0^\circ$ ). Unstable  $0^+$  and  $2^+$  states at 10–11 MeV of excitation

energy may be connected with such a configuration. The prolate 3:1 configuration is expected to cross the “ground-state band,” i.e. the oblate 2:1 configuration, at spin 4 (Figure 23).

Among many examples of excited superdeformed configurations in light nuclei is the 2:1 band in  $^{32}\text{S}$  ( $^{16}\text{O} + ^{16}\text{O}$ ) (144, 285), a 4:1 configuration in  $^{16}\text{O}$  (four alpha particles in a row) (144, 145, 286), or a suggested 5:1 shape in  $^{20}\text{Ne}$  ( $\varepsilon = 1.25$ ,  $\varepsilon_4 = 0.24$ ) (144) and a 6:1 shape in  $^{24}\text{Mg}$  ( $\varepsilon = 1.25$ ,  $\varepsilon_4 = 0.08$ ).

With quite good success one can associate local potential-energy minima at large deformations with resonances seen in heavy ion collisions (for review, see 287). For example, a minimum in the  $^{24}\text{Mg}$  energy surface at  $\varepsilon \approx 1.2$ ,  $\gamma \approx 40^\circ$  has been related to resonances seen in the  $^{12}\text{C} + ^{12}\text{C}$  reaction. The moment of inertia that can be deduced by connecting the resonance energies at different angular momenta fits well with the rigid-body value calculated at the large deformation (209). In fact, several “bands” of resonance states have been seen in the  $^{12}\text{C} + ^{12}\text{C}$  reaction, and efforts have been made to relate them to different shapes and excitations in the  $^{24}\text{Mg}$  system (288).

Angular momenta much higher than in any other light system (up to the vicinity of spin  $40\hbar$ , have been identified in  $^{56}\text{Ni}$ , which can be considered as an intermediate system in the  $^{28}\text{Si} + ^{28}\text{Si}$  reaction (289). Also, in the  $^{24}\text{Mg} + ^{24}\text{Mg}$  reaction several high-spin resonances have been identified in the proposed intermediate  $^{48}\text{Cr}$  system (290). High-spin PES utilizing the

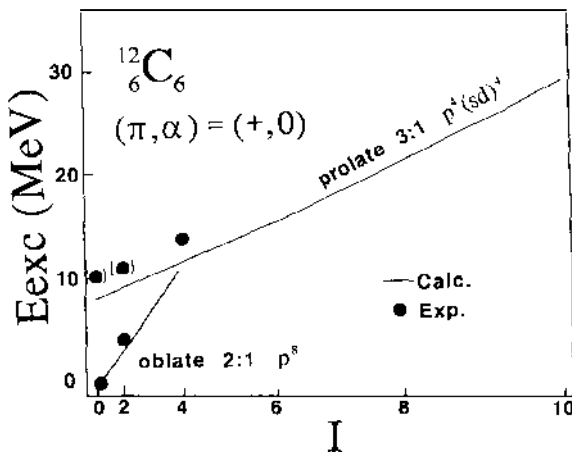


Figure 23 The two lowest calculated configurations in  $^{12}\text{C}$  corresponding to very deformed shapes: collectively rotating 2:1 oblate shape and prolate 3:1 shape. Experimental energies are indicated by dots. (From 284.)

MO potential show minima for  $^{56}\text{Ni}$  and  $^{24}\text{Mg}$  at deformations roughly corresponding to two  $^{28}\text{Si}$  or two  $^{24}\text{Mg}$  nuclei touching each other (291; I. Ragnarsson, S. Åberg, unpublished, 1984).

**5.6.4 PERSPECTIVES** With the help of future powerful detector systems like the Eurogam, Gammasphere, and the Euroball, much will certainly be learned about superdeformation. One question concerns a possible deformation dependence of the spin-orbit potential (292–294), about which detailed spectroscopy in the superdeformed states may provide an answer. Other interesting perspectives are new superdeformed regions, either in terms of new mass regions with already known shapes or in terms of yet unknown, more exotic shapes.

From the shell-energy diagram in Figure 17, one can see that nuclei in the  $N = Z \approx 40$  region obviously favor large deformations ( $\varepsilon \approx 0.6$ ). This spin-zero tendency remains at high spins, and superdeformed configurations in nuclei around  $^{80}\text{Zr}$  are predicted to be yrast at spin  $\sim 40\hbar$  (145, 198, 204, 294a, 295–297). In Figure 24 we compare the spectrum of  $^{80}\text{Sr}_{42}$  obtained from Skyrme III Hartree-Fock and Nilsson-Strutinsky calculations. Note the astonishing similarity between the two. A minor difference is that the HF calculation gives a slightly larger effective moment of inertia than the NS calculation (cf Figure 24, in which energies  $0.018I^2$  and  $0.02I^2$  are subtracted for the HF and NS calculations, respectively). The neutron and proton configurations of the lowest bands are approximately the same in both models. The shape change from prolate (configuration “1”) to oblate (“2”) deformation, both with collective rotation, is connected with the alignment of  $g_{9/2}$  neutrons. At higher spins,  $h_{11/2}$

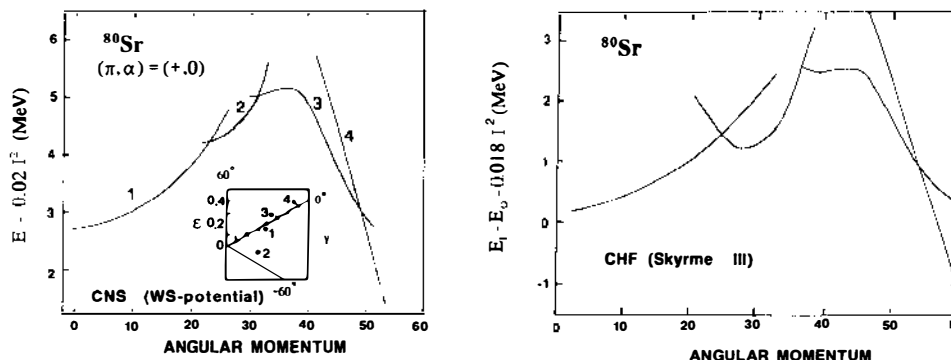


Figure 24 Collective rotational bands with  $(\pi, \alpha) = (+, 0)$  in  $^{80}\text{Sr}$  calculated with a cranked NS model using the WS potential (left), and the cranked HF approach with a Skyrme III force (right). (From 204, 297.)



neutrons are occupied, which results in a larger prolate or slightly triaxial deformation (configuration “3”). Finally, for superdeformed yrast states ( $\beta_2 \approx 0.6$ ), the configuration involves the alignment of two protons and two neutrons in  $h_{11/2}$  ( $\pi 5^2\nu 5^2$ ). At high frequencies (or particle numbers) the lowest  $i_{13/2}$  ( $N = 6$ ) orbital also becomes occupied, which gives rise to an even larger superdeformation.

Very little is known about the very neutron-deficient Po-Th nuclei with  $N < 126$ . Theoretically, the most interesting are the very neutron-deficient nuclei with  $N = 104$ –116. Indeed, the calculated PES are shallow and the energies of the prolate and oblate minima are very close (126). An interesting feature of the calculated PES is the presence of low-lying superdeformed minima with  $0.6 < \beta_2 < 0.8$ . In  $^{198,200}\text{Ra}$  these minima are expected to be almost degenerate with the ground state.

The possibility for triaxial high-spin superdeformations ( $\epsilon \approx 0.45$ ,  $\gamma \approx 20^\circ$ ) has been discussed in several papers (99, 100, 145, 258, 260, 298–300). This kind of superdeformation should appear in nuclei with proton numbers  $Z = 70$ –74 and neutron numbers  $N = 88$ –106, and these bands are calculated as yrast for  $I \lesssim 50\hbar$ . Since the triaxiality is rather large and stable, triaxial superdeformations may provide good examples for studying triaxial quantum phenomena such as wobbling bands or special electromagnetic properties. Furthermore, the  $\mathcal{J}^{(2)}$  moment of inertia is expected to behave in an unusual way. Since the rotation is predicted to occur around the smallest axis,  $\mathcal{J}^{(2)}$  is expected to be substantially smaller than the corresponding axial deformation (298, 300).

Dudek (215) predicted octupole instability of  $^{152}\text{Dy}$  in the superdeformed minimum, and Höller & Åberg (301) suggest stable reflection-asymmetric superdeformations for nuclei around  $^{200}\text{Rn}$ . Although the spin alignment is strongly affected by octupole deformation (see Section 6), the  $\mathcal{J}^{(2)}$  behavior in the superdeformed bands is only very weakly influenced (301). However, one way of detecting reflection-asymmetric superdeformations would be to observe enhanced E1 transitions (see Section 6.3). At a sufficiently large octupole deformation these may indeed compete with the supercollective E2 transitions at low spins.

Cranked NS calculations also suggest the existence of so-called hyperdeformations in nuclei around  $^{168}\text{Yb}$  (302). These very elongated shapes ( $\beta_2 \approx 0.9$ ,  $\gamma = 0^\circ$ ) are expected to become yrast at around spin  $80\hbar$ . Other types of exotic superdeformed shapes are the “banana” shapes, involving a  $Y_{31}$  component in the mean field (303) or the “molecular” shapes in heavier nuclei (257, 301, 304). These molecular shapes might exist in both symmetric and in asymmetric combinations of ions and should be favored by heavy ion reactions in which the target and the projectile are close to doubly magic.

## 6. REFLECTION-ASYMMETRIC SHAPES

The question of whether certain nuclei can be reflection asymmetric in their ground and excited states has been a subject of many experimental and theoretical studies. The issue was first considered in the 1950s (305, 306) following the discovery of low-lying negative parity states in light actinides (307). The single-particle mechanism underlying the effect of spontaneous breaking of reflection symmetry was emphasized by Strutinsky (306), who pointed out that the particle-hole coupling between opposite parity levels yields a tendency toward octupole deformation. This problem was investigated in more detail by many authors (308–319) but no sizeable effect was obtained in the ground state; these early calculations of deformation energies led to the conclusion that even-even nuclei with low-lying negative parity states are very soft with respect to intrinsic octupole deformation, but are never unstable.

First indications for a reflection-asymmetric component of the mean field came from investigations of light systems (144, 313, 315, 316, 320), which can also be described in terms of alpha clusters. For example, a sizeable octupole effect was found in  $^{24}\text{Mg}$ , where the reflection-asymmetric minimum was predicted at about 17 MeV (144) as compared to an experimental resonance state at 19.3 MeV (321).

Nuclei with strong octupole correlations have particularly low-lying negative parity states. From the systematics of the lowest negative parity excitations (322), one learns that the nuclei with strongest octupole correlations are the neutron-deficient nuclei around  $^{224}\text{Th}$  (with negative parity excitations of the order of 200 keV) and the neutron-rich nuclei around  $^{146}\text{Ba}$  (with the energy of lowest  $1^-$  state of about 750 keV). The reason that regions of very strong octupole correlations are especially well localized around particular proton and neutron numbers can be understood from the Nilsson diagram shown in Figure 2. The tendency toward maximal octupole coupling occurs just above closed shells, i.e. for  $Z$  or  $N \approx 34, 56, 88$ , and  $134$ , where the  $(Nl_j)$  intruder orbitals interact with the  $(N-1, l-3, j-3)$  natural parity states through the octupole component of the mean field. In combining these “octupole-driving” particle numbers, five regions of likely candidates for octupole-deformed equilibrium shapes emerge: neutron-deficient actinides with  $Z \approx 88$  and  $N \approx 134$ , neutron-rich (neutron-deficient) Xe-Nd isotopes with  $Z \approx 56$  and  $N \approx 88$  ( $N \approx 56$ ), and light (heavy) Ge-Kr nuclei with  $Z \approx 34$  and  $N \approx 34$  ( $N \approx 56$ ). Figure 25 shows the shell-energy landscapes of the MO potential plotted versus the particle number and octupole deformation  $\varepsilon_3$ . Notice that the shell energy slopes down with  $\varepsilon_3$  at the “optimal” particle numbers discussed above. Generally, the energy distance between the

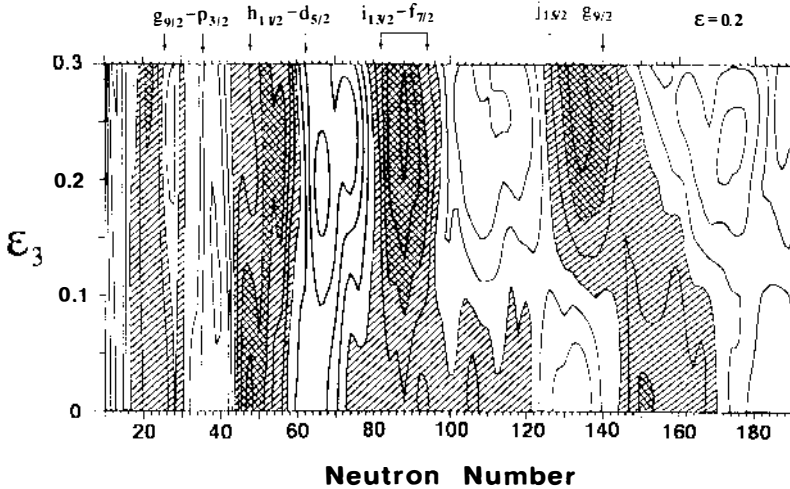


Figure 25 Shell energy diagram of the MO potential in the  $(\epsilon_3, N)$  plane at the prolate deformation  $\epsilon = 0.2$ . Regions with negative shell energy are shaded, and cross shading is used for regions with shell energy below  $-3$  MeV. The strongest octupole coupling arises from the coupling between  $\Delta l = \Delta j = 3$  subshells. (From 322.)

orbitals coupled by an octupole field decreases with increasing mass number. At the same time, both the number and the magnitude of the coupling matrix elements increase. This explains, for example, why the octupole coupling is stronger in the Ra-Th region than in the Ba-Nd region.

### 6.1 Occurrence

A turning point in the studies of pear-shaped nuclei came with the theoretical predictions made in the beginning of the 1980s and demonstrating that certain neutron-deficient actinide nuclei can be described in terms of octupole deformation. In 1980, Chasman (323), using a model based on diagonalization of Woods-Saxon single-particle levels, gave the first evidence for the presence of ground-state octupole deformation in  $^{229}\text{Pa}$  and  $^{227}\text{Ac}$ . One year later a substantial ground-state octupole instability was found in the folded Yukawa NS model calculations of Möller & Nix (324) for a number of nuclei around  $^{224}\text{Ra}$ . They used an improved macroscopic energy term, much softer toward higher multipoles as compared to the standard Myers-Swiatecki formula (85). The predicted gain in binding energy due to octupole degree of freedom of about 1–2 MeV greatly reduced previous discrepancies between calculated and experimental masses. These findings were expanded in a survey by Leander et al

(322), who successfully employed the folded Yukawa model to explain various spectroscopic properties of light actinide nuclei.

In the ensuing years a flurry of experimental and theoretical discoveries provided new indications of reflection-asymmetric deformations in medium mass and heavy nuclei. The predictions of folded Yukawa models were soon supported by the shell correction calculations based on Woods-Saxon (325, 326) and modified oscillator (327) potentials. The potential energy as a function of octupole deformation is displayed in Figure 26 for the four strongly octupole-favored nuclei for the modified oscillator (MO), Woods-Saxon (WS), and folded Yukawa (FY) models (325). Although the octupole instability manifests itself in a similar way in all the models, the difference in magnitude of octupole deformation energy can be seen. This discrepancy arises primarily from the different values of the interaction coupling and from the different single-particle energy separations between the strongly interacting orbitals (for discussion, see 325, 327).

In the regions of nuclei around  $^{146}\text{Ba}$  and  $^{114}\text{Xe}$ , octupole instability was first predicted by Nazarewicz et al (325) and Skalski (328), respectively, but the calculated octupole potentials turned out to be much softer than in the Ra-Th region (Figure 26).

Recently, it was demonstrated that the higher-multipole deformations ( $\beta_5, \beta_6, \dots$ ) can stabilize octupole minima. The importance of the  $\lambda = 5$  deformation was first noticed by Möller et al (329, 330) in their description of the fission process. Various authors used the higher-multipole deformations  $\lambda = 5, 6$  but not as free variational parameters, since they were estimated from the minimum of the macroscopic part of the energy (322, 324, 325). The importance of the  $\lambda = 6$  moment in describing reflection-asymmetric nuclei was emphasized by Chasman (331), who demonstrated that inclusion of this degree of freedom leads to substantial reduction of octupole barriers in light actinides. However, soon afterward it was shown within the many-dimensional NS calculations employing a rich deformation space that, after taking into account the higher-order odd multipole deformations,  $\lambda = 5, 7$ , the reflection-asymmetric shape again becomes very favorable (332–334; see also 280). Figure 27 displays the systematics of calculated deformation energies,  $E_{\text{def}}$ , octupole barriers,  $E_{\text{om}}$ , and equilibrium deformations,  $\beta_{2,\dots,7}$ , for even-even nuclei from the Ra-Th region (333). It is seen that the equilibrium values of  $\lambda = 5$  deformation are roughly proportional to those of octupole deformation. This result can be explained using simple shell model selection rules for multipole moments, as demonstrated by Ćwiok & Nazarewicz (334) in their discussion of the microscopic basis of the higher-order deformation.

Only very recently was the concept of stable octupole deformation in both the Ra-Th and the Xc-Sm regions supported by self-consistent

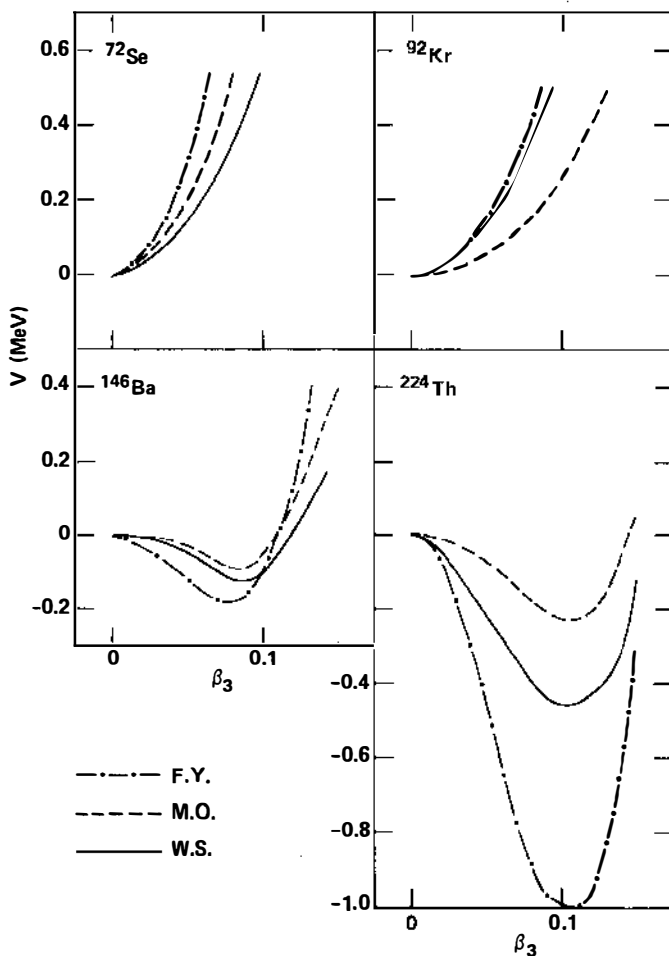


Figure 26 PES curves in the  $\beta_3$  direction calculated for  $^{72}\text{Se}$ ,  $^{92}\text{Kr}$ ,  $^{146}\text{Ba}$ , and  $^{224}\text{Th}$ . Three different NS calculations are compared: the folded Yukawa model (FY), the MO model, and the WS model. (From 325.)

calculations. Bonche et al (75, 335) employed the HF + BCS model using the Skyrme III effective interaction and projection on parity. As an example, such calculations for  $^{222}\text{Ra}$  are shown in Figure 28. After projecting out the good parity, both  $\pi = +$  and  $\pi = -$  states acquire large octupole deformations but different quadrupole moments. Similarly, Hartree-Fock calculations have been performed with the Gogny forces for

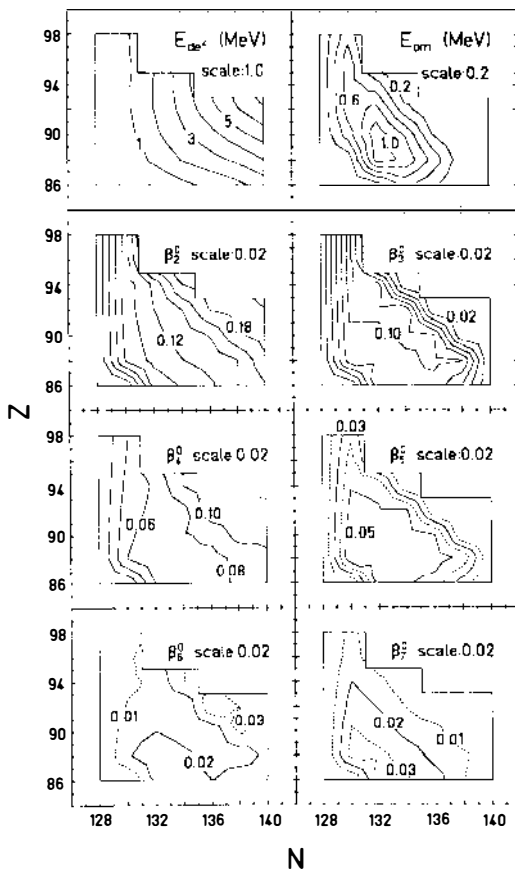
$$\min: \beta_{\lambda} \quad (\lambda=2,3,4,5,6,7,8)$$


Figure 27 Calculated equilibrium deformations for several actinide nuclei in the  $(Z, N)$  plane. The WS potential was used with a free minimization of the energy with respect to all  $\beta_\lambda$ ,  $\lambda = 2-8$ . In the two upper portions the deformation energy and octupole barrier are shown. (From 333.)

light actinides (336, 337). Again, octupole barriers of 1–2 MeV were obtained, see Figure 29. The experimental parity splitting and transition probabilities could be well described in models utilizing dynamical correlations (337, 338). The higher-multipolarity deformations,  $\beta_5$ ,  $\beta_6$ , and  $\beta_7$ , extracted from self-consistent calculations (337) turned out to be of the same order and to behave in a way similar to those obtained within the shell correction method (333, 334). One can thus conclude that both the NS

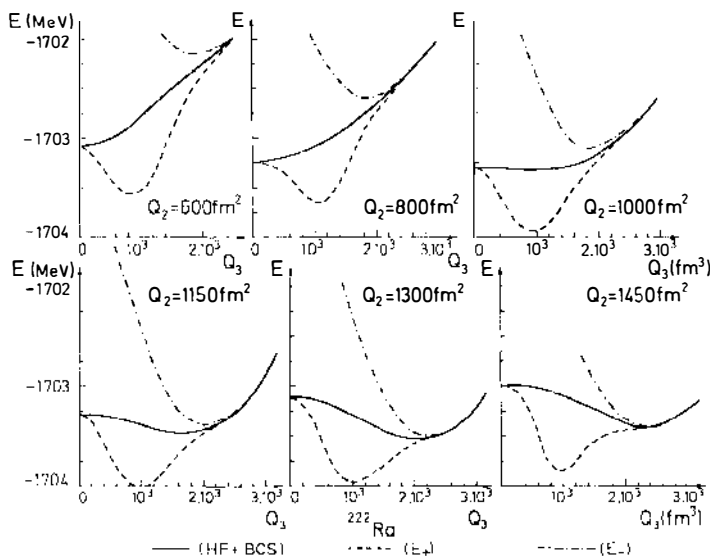


Figure 28 PES curves along the mass octupole moment,  $Q_3$ , for  $^{222}\text{Ra}$  at six different quadrupole shapes. The calculation is performed within the HF+BCS method using the Skyrme III interaction without (solid lines) and with (dashed lines and dot-dashed lines) parity projection. Note that the  $\pi = +$  and  $\pi = -$  states have different quadrupole deformation. (From 75.)

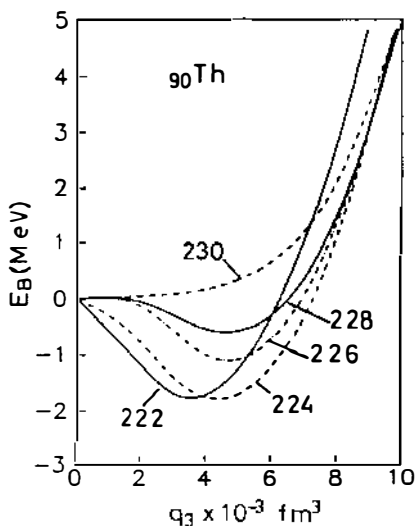


Figure 29 PES curves along the mass octupole moment for even-even Th isotopes with  $A = 222-230$ . The calculations employed the HFB method with the Gogny effective interaction. (From 337.)

model and self-consistent approaches lead to similar results for octupole instability around  $^{146}\text{Ba}$  and  $^{222}\text{Th}$ .

## 6.2 Spectroscopy

The calculated octupole barriers of the order of 1–2 MeV suggest strong octupole anharmonicities rather than stable octupole shapes. Probably the strongest indication for the static octupole field is revealed by high-spin spectroscopy. In a reflection-asymmetric nucleus one should expect a “quasi-molecular” rotational band with spin states of alternating parity, connected by collective electric dipole transitions. Such bands were first observed in  $^{222}\text{Th}$  (339) and then in many Ra-Th (e.g. 340–343) and Ba-Sm (e.g. 344–348) nuclei.

In the presence of static octupole deformation, neither the intrinsic parity  $\pi$  nor the signature  $r$  are good quantum numbers. However, the mean field can still be invariant with respect to the reflection through the  $(y, z)$  plane (7, 349). The quantum number  $s$  associated with this self-consistent symmetry is called simplex (340, 350, 351) (see Table 1). Frauendorf & Pashkevich (352) referred to this quantum number as combined signature. A rotational band of total simplex  $s$  consists of spin states  $I$  of alternating parity,  $\pi = se^{-inI}$ .

Theoretical calculations of the single-particle states in an octupole-deformed cranked potential were first carried out in 1981 by Faber et al (353, 354) in the context of heavy-ion-induced fission. They employed the Strutinsky method without pairing to describe the mass-asymmetric fission channel at high spins in heated nuclei. Four years later this model was extended to take into account pairing correlations, and was then applied to Ra-Th nuclei by Nazarewicz et al (340, 341, 350, 351, 355) and Frauendorf & Pashkevich (352). As an example of a typical quasi-particle diagram, the quasi-particle proton Routhians in  $^{222}\text{Th}$  are shown in Figure 30 as functions of rotational frequency at  $\beta_3 = 0$  and  $\beta_3 = 0.14$ . The two diagrams are indeed very different. At  $\beta_3 = 0$  a clear backbending is present, the result of the alignment of high- $j$  intruder orbitals (here  $i_{13/2}$  protons). At  $\beta_3 \neq 0$  the excitation pattern becomes very collective, with many orbitals having about equally large alignment, and the sharp band crossing is washed out (340, 350, 351, 356). The microscopic mechanism responsible for the “equalization” of the rotational strength is the parity mixing between the strongly aligned intruder orbitals and the natural parity states carrying considerably smaller angular momentum alignment.

At high rotational frequencies, aligned quasi-particle excitations have a strong tendency to drive a nucleus toward the mirror-symmetric shape (340, 355). For the ground-state octupole minima this polarization effect is not strong enough to restore the reflection symmetry in two quasi-



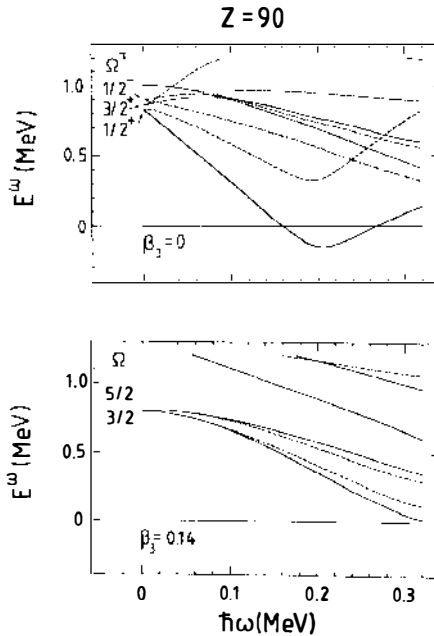


Figure 30 The influence of octupole deformation on quasi-particle Routhians,  $E^\omega$ . Solid lines indicate Routhians with simplex  $s = +i$  while dashed lines correspond to  $s = -i$ . The simplex splitting and the angular momentum alignment are much larger in the reflection-symmetric case (upper part) than in the limit of static octupole deformation (lower part). The  $\Omega$  quantum number is only valid at  $\hbar\omega = 0$ . (From 340.)

particle configurations. Nevertheless, after the alignment of a second nucleon pair, a nucleus is predicted to undergo a shape transition toward  $\beta_3 = 0$ . This effect is illustrated in Figure 31, which presents the angular momentum alignment plot calculated for  $^{222}\text{Th}$  using a WS cranking model with pairing (355). Up to  $I \approx 26$  the yrast line can be associated with the reflection-asymmetric configuration, while at higher spins a band crossing takes place with a four-quasi-particle band,  $\nu j_{15/2}^2 \pi i_{13/2}^2$ , at  $\beta_3 = 0$ . The experimental data are also shown for comparison (357). While at  $\beta_3 \neq 0$  a gradual increase of  $I$  with  $\hbar\omega$  can be seen, in nice agreement with the data, there are two sharp band crossings around  $I = 12$  predicted by the calculations at symmetric shape. It can be seen that the shape transition is expected just above the last experimental point and thus it would be very interesting to extend the data to still higher angular momenta to test this prediction. In the Ba-Nd region the calculations also suggest a shape change associated with the alignment of a neutron pair (345, 347) and

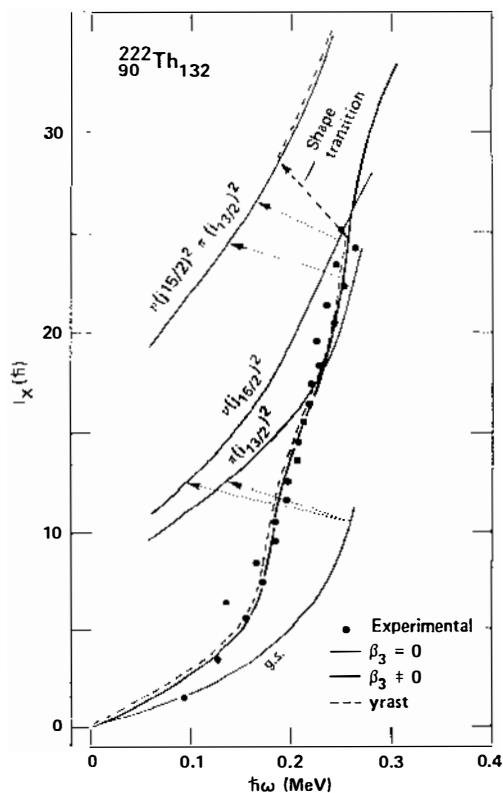


Figure 31 Angular momentum vs rotational frequency for  $^{222}\text{Th}$  calculated with (*thick solid line*) and without (*thin solid lines*) octupole deformation. The calculated yrast sequence is marked by a *dashed line*. Experimental values are marked by *filled circles*. Note the calculated shape transition at  $I \approx 24\hbar$  from  $\beta_3 \approx 0.10$  to  $\beta_3 \approx 0$ . (From 355; experimental data are taken from 357.)

indeed, an abrupt termination of the octupole strength was detected in  $^{150}\text{Sm}$  just after the neutron crossing (346).

In both the Ra-Th and Ba-Sm regions of octupole instability there is a general tendency to enhance octupole correlations at low and medium spins. At large octupole deformations, pairing correlations are weaker (because of large gaps in the single-particle spectrum), and the weakness increases the moments of inertia. Secondly, the octupole strength is locally enhanced by the mixing between intruder and natural parity orbitals that approach each other with increasing frequency. The shape changes induced by rotation are most pronounced in nuclei like  $^{146}\text{Nd}$ ,  $^{148}\text{Sm}$ ,  $^{218}\text{Ra}$ , which do not have well-developed ground-state deformations, and which

experimentally exhibit “quasi-rotational” bands. Calculations suggest that in these nuclei significant octupole instability persists up to very high rotational frequencies (345, 355). For  $^{218}\text{Ra}$  this prediction was recently confirmed experimentally by Schulz et al (358).

An octupole component of the mean field deformation affects some single-particle orbitals in ways that should be manifest in the spectroscopy of odd- $A$  nuclei. The experimental fingerprint of octupole deformation in odd- $A$  nuclei is the presence of parity doublets with very distinct rotational properties and unusual electromagnetic moments. A beautiful example of such structure is the rotational “quasi-molecular” parity doublet in  $^{223}\text{Th}$  (343). There exists a rich literature on how to interpret the properties of one-quasi-particle states in the presence of octupole deformation (323, 334, 340, 359–364). Because of the above-mentioned fragmentation of the single-particle angular momentum, octupole deformation can significantly influence the single-particle intrinsic parity contents (361) and Coriolis matrix elements. Therefore, parity splittings, spectroscopic amplitudes, decoupling parameters, magnetic moments, and electromagnetic rates all change in the octupole-deformed nucleus. An extensive survey of different manifestations of octupole instability in odd- $A$  nuclei can be found in works by Leander et al (361, 363) in terms of the reflection-asymmetric particle-plus-rotor model.

As stated above, the quasi-particle excitations induce a strong octupole shape-polarization effect on the core. One may thus expect that the ground-state deformation and the size of the octupole barrier in an odd- $A$  system will vary depending on which single-particle orbital is occupied by the odd particle (322, 361, 364). In  $^{227}\text{Th}$ , for example, calculations predict coexisting symmetric and reflection-asymmetric states (364).

### 6.3 Dipole Moments

If the nuclear mean field is not reflection symmetric, a large E1 moment may arise in the intrinsic frame because of a shift between the centers of mass of the proton and neutron distributions (Figure 32). Such a dipole moment should manifest itself by very enhanced electric dipole transitions between opposite parity members of quasi-molecular rotational bands. This fact was pointed out in the 1950s by Strutinsky (306) and Bohr & Mottelson (365, 366), who estimated the value of the intrinsic dipole moment based on a liquid drop model. Experimental dipole moments extracted from measured  $B(\text{E1})$  transitions in the Ra-Th and Ba-Nd nuclei are indeed unusually large, of the order of 0.1–0.3 efm (e.g. 339, 343, 344, 346, 348). In recent papers the shell correction approach to the isovector E1 moment has been formulated for Ra-Th and Ba-Nd nuclei (345, 367, 368). Within this theory the E1 moment can be written as a sum of two

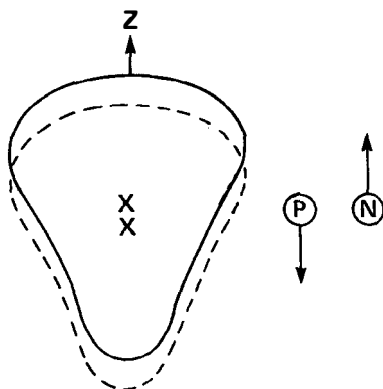


Figure 32 Schematic illustration of the increase of the static dipole moment due to the presence of static reflection-asymmetric deformations. (From 368.)

terms: a macroscopic (liquid drop) term,  $Q_1(\text{LD})$ , and a shell correction term,  $Q_1(\text{SC})$ . The latter is given by

$$Q_1(\text{SC}) = e(1 + \chi) \left( \frac{N}{A} \langle z \rangle_p - \frac{Z}{A} \langle z \rangle_n \right), \quad 21.$$

where  $\chi$  is the E1 polarizability coefficient and  $\langle z \rangle$  is the Strutinsky-renormalized displacement of the center of mass. As shown in Figure 33, the quantity  $\langle z \rangle$  displays a smooth oscillatory behavior as a function of particle number (368). The strongest shell correction to the dipole moment should be expected for Th and U isotopes with  $N \approx 130$  and for Sm-Gd isotopes with  $N \approx 86$ . The macroscopic contribution to the dipole moment was estimated and found to be negligible within the droplet model by Dorso et al (369). This conclusion, however, was recently questioned by Denisov (370), whose result is consistent with the previous estimate of Strutinsky (306) (cf. 370a). On the other hand, the values extracted from experiment are much smaller (345, 368). From this point of view, the question of the magnitude of the liquid drop dipole moment is still open. The shell correction calculations provide an overall agreement with experimental data (345, 368, 371, 372). In particular, a dramatic reduction of  $Q_1$  in  $^{224}\text{Ra}$  and  $^{146}\text{Ba}$  and an enhancement in  $^{222}\text{Th}$  and  $^{150}\text{Sm}$  are borne out by the calculations.

Intrinsic dipole moments for even-even Ra and Th isotopes have also been calculated within the HF + BCS model with the Gogny interaction by Egido & Robledo (337). They also predicted a very low value of  $Q_1$  in  $^{224}\text{Ra}$  and reproduced observed  $B(\text{E}1, 1^- \rightarrow 0^+)$  transition rates in all Ra and Th nuclei considered.

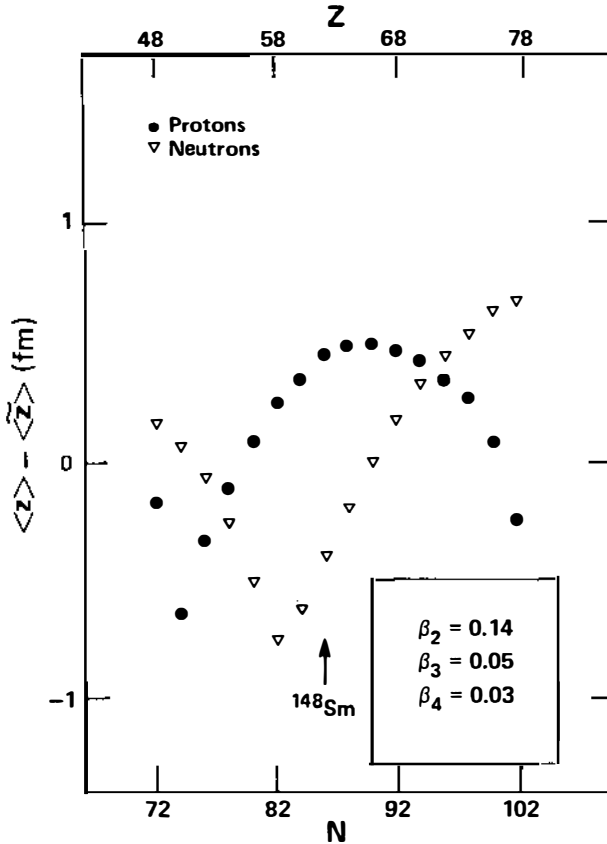


Figure 33 The Strutinsky renormalized contribution to the displacement of the center of mass for protons and neutrons for neutron numbers  $N = 72$ – $102$  and proton numbers  $Z = 48$ – $78$ . The calculation is performed with the WS potential at the fixed deformation,  $\beta_2 = 0.14$ ,  $\beta_3 = 0.05$ ,  $\beta_4 = 0.03$ . With the combinations of  $N$  and  $Z$  values shown, large cancellation in the E1 moment occurs in  $^{146}\text{Ba}$ , but enhancements are found in  $^{148}\text{Sm}_{86}$ . (From 368.)

## 6.4 Exotic Octupole Shapes

The nuclei that are predicted in calculations to be octupole soft or even unstable belong to a transitional region between spherical and well-deformed shapes. Consequently, nonaxial deformations are likely to exert some influence. Moreover, the axial symmetry is expected to be broken at high spins, especially after angular momentum alignment of the first pair of quasi-particles (see Section 5.2). In all calculations mentioned so far,

however, axial symmetry has been assumed, mainly because of numerous conceptual and computational difficulties associated with simultaneous inclusion of both reflection asymmetry and triaxiality. Probably the first attempt to investigate the combined effect of octupole deformation and triaxiality was the Nilsson model study by Åberg et al (158), who discussed the second saddle-point configurations in actinides. Recently, Chasman & Ahmad (373) employed the shell correction approach with a WS potential to the octupole-unstable ground states in Ra-Th isotopes. They found very  $\gamma$ -soft octupole minima, with  $Z = 86$ ,  $N = 130$  as an optimal case. This study was followed by that of Skalski (108), who also used the WS model but considered a much richer family of shapes. He found rather large stiffness against triaxiality for Ba-Nd and Ra-Th regions. The  $\gamma$  stiffness is predicted to be smaller in very neutron-deficient reflection-asymmetric Xe and Ba isotopes but is as yet undiscovered experimentally. Probably the best prospects for finding a nonaxial octupole shape are in  $^{64}\text{Ge}$  and  $^{96-98}\text{Zr}$ . The calculated octupole minimum in  $^{64}\text{Ge}$  is rather soft in both  $\beta_3$  and  $\gamma$ , which will probably influence the low-energy spectrum of this exotic  $N = Z$  system (108, 374). In  $^{96}\text{Zr}$  the calculations suggest a nearly spherical shape with pronounced octupole instability (375). The measured  $B(E3, 3_1^- \rightarrow 0^+)$  rate of  $65 \pm 10$  W.u. is the fastest known (375 and references therein).

It has long been known that inclusion of reflection asymmetry is essential for describing nuclear fission phenomena. In 1961, MO model calculations by Johansson (311) demonstrated that  $\lambda = 3$  deformation may lower the second barrier peak by 1–4 MeV. This work was extended by many authors (e.g. 88, 91, 318, 329, 330, 376–380). As a detailed analysis of these results goes beyond the scope of this paper, we comment only on the recent investigations of two fission modes of the heavy fermium elements (119, 381, 498). The results of NS-type calculations involving a rich space of nuclear shapes explain the simultaneous appearance of two fission modes with low and high total kinetic energy of the fragments, observed experimentally (382). Figure 34 illustrates the shape of  $^{258}\text{Fm}$  along two families of shapes  $L_1$  and  $L_2$  favored by calculations (498). The latter trajectory corresponds to more reflection-asymmetric and more elongated shapes.

Finally, let us comment on yet another manifestation of nuclear octupole deformation, probably the most spectacular one. In the beginning of the 1970s a third minimum around the fission barrier of heavy elements was predicted in the NS model calculations by Pashkevich (115) and Möller (330). This shallow minimum corresponding to large elongation,  $\varepsilon \approx 0.9$ , splits the asymmetric saddle into two asymmetric saddle points. Experimentally, this minimum appears as a microstructure in the resonances found using the (n, f) and (d, pf) reactions (see 383–385). The calculated

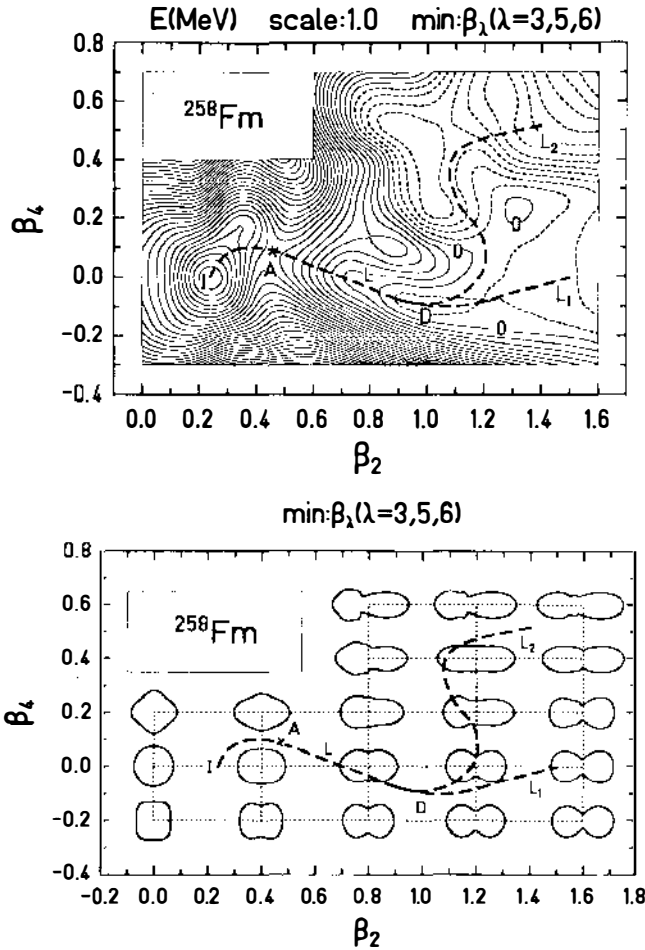


Figure 34 Calculated PES curves for  $^{258}\text{Fm}$  (upper part) and corresponding shapes (lower part). Two favored fission paths are marked as  $L_1$  and  $L_2$ . The path  $L_1$  resembles the fusion path while octupole shapes play a role along the “fission-like” path  $L_2$ . (From 498.)

octupole deformation of a third minimum is large, about  $\epsilon_3 = 0.2$ , and it manifests itself by the presence of alternating parity bands built on the same single-particle state. Therefore, these third minima are one of the best nuclear pear-shapes known. A systematic study of a third minimum, made using the NS approach, found that it is very shallow and very localized in particle number (386). The deepest minimum, about 1.5 MeV, is predicted for very neutron-rich nuclei around  $Z = 86$ ,  $N = 148$ .

## 7. SHAPE COEXISTENCE

The phenomenon of coexisting nuclear states built upon configurations with different shapes is usually referred to as shape coexistence or shape isomerism. There already exists a very rich literature devoted to this issue; see for example reviews by Hamilton and coworkers (387–389). Therefore we do not discuss this topic in great detail, but rather attempt to present some recent examples and developments. In this section we focus attention on the shape coexistence phenomenon at low excitation energies, near the ground state. Several examples of shape coexistence at high spins are discussed in Section 5.

Generally, the phenomenon of shape coexistence can be related to (a) strong shell effects resulting from the subshell closures (large energy gaps in the single-particle spectrum) at different deformations, and (b) strong single-particle polarization caused by deformation-driving Nilsson orbitals. Good examples of scheme (a) are the fission isomers in actinides (see 88) and the superdeformed rotational bands in the rare earth nuclei around  $^{152}\text{Dy}$  (Section 5.6). The shape isomers belonging to the group (b) include the intruder states in the neutron-deficient Pb isotopes discussed below and the well-deformed rotational bands around  $^{132}\text{Ce}$ , discussed in Section 5.3. In many cases the effects of single-particle deformation polarization and the shell structure are strongly correlated because the number of occupied deformation-driving orbitals is relatively large.

A simple illustration of the single-particle polarization mechanism is provided by the deformation variations between 1qp states in odd- $A$  nuclei. The noncollective band heads energies can be calculated within the independent-quasi-particle formalism (with or without blocking) (e.g. 217, 390–394a). Figure 35 shows calculated equilibrium deformations for different single-proton configurations in Lu isotopes (394a). They are compared to the ground-state shapes in the neighboring even-even cores of Yb and Hf. The equilibrium values of  $\beta_2$  and  $\beta_4$  exhibit a pronounced configuration dependence, and therefore the usual assumption of a fixed shape in all the 1qp states is not justified. Of course, the single-particle polarization is even more pronounced in transitional nuclei with soft even-even cores (note that the Yb and Hf cores shown in Figure 35 are amongst the most deformed systems in the whole rare earth region). Several examples of such situation are discussed below.

### 7.1 *Competing Prolate and Oblate States*

In many nuclei calculated PES curves show the presence of two axial minima, one corresponding to an oblate shape and one associated with a



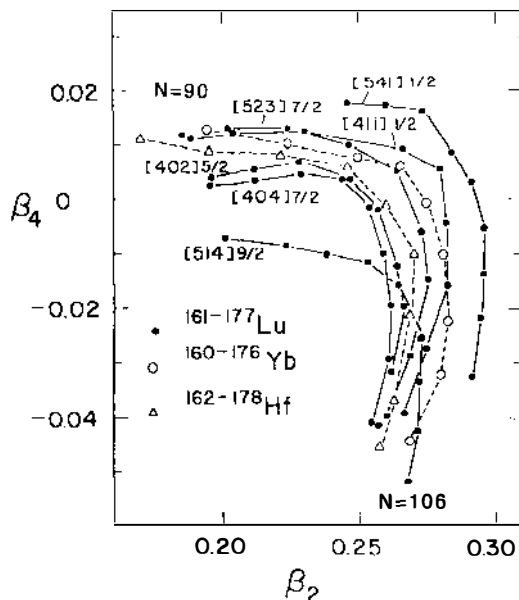


Figure 35 Calculated equilibrium deformations for various states in the odd Lu isotopes with  $A = 161-177$ . Also shown are the ground-state equilibrium deformations in the even-even cores of Yb and Hf. (From 394a.)

prolate configuration. The barrier between the two minima appears for a triaxial shape.

In the light nuclei ( $A \approx 80$ ), many examples of nuclear shape coexistence have been established (387-389). The richness of different structural effects makes this region an ideal area for testing various theoretical approaches. The microscopic reason for the observed strong variation of collective properties with particle number is the relatively low single-particle level density in these medium-mass nuclei. While in the heavier systems equilibrium deformations vary smoothly from nucleus to nucleus, in the  $A \approx 80$  region shape changes are much more abrupt.

Calculations employing the shell correction method (109, 123, 124, 126, 197, 204-206, 324, 395, 396) and the HF method (72, 74, 147, 148, 297, 397-399) suggest an interpretation of experimental data in terms of well-deformed, elongated (prolate) shapes competing with flattened (oblate) shapes and shell-model (spherical) configurations. The differences among various models are reflected by their predictions concerning prolate-oblate energy differences and deformation energies, and the nature of shape-

coexisting states. As shown in Figure 36, an astonishingly close agreement between predicted prolate-oblate energy differences, deformation energies, and equilibrium deformations was found for a folded Yukawa model (124, 324) and a Woods-Saxon model (204). The self-consistent HF calculations with the Skyrme III force (74) yield similar results (see 198 for discussion). In Figure 24 the calculated energy evolution vs angular momentum for  $^{80}\text{Sr}$  was shown from two models: Skyrme III HF and NS with the WS potential (cf Sections 5.6.4 and 9.1). The various kinds of shapes coexist in both model calculations, and the structure of the yrast line is also very similar. It is predicted that nuclei with a large prolate ground-state deformation are centered around particle number 38–40 while oblate ground states are expected in nuclei with particle number around 32–34. The best prospects for prolate-oblate shape coexistence are the Se, Br, Kr, Rb, and Sr isotopes with  $36 \leq N \leq 42$  (205, 396).

The neutron-deficient Pt, Au, and Hg isotopes also exhibit striking examples of shape coexistence at low spins. The first predictions of shape-coexisting structures around  $A = 186$  were given by Kumar & Baranger (134, 400) within the quadrupole-plus-pairing model. Mean field calculations predict two minima to coexist in PES for Ir, Pt, Au, and Hg isotopes with  $N \leq 110$  (the heavier isotopes are weakly oblate deformed) (37, 116, 123, 124, 221, 324, 372, 401–415). The prolate minimum,  $0.2 < \beta_2 < 0.25$ , can be associated with the ground state in the Pt isotopes, while the less deformed oblate minimum,  $-0.15 < \beta_2 < -0.1$ , forms an excited intruder  $0^+$  state. In the Hg isotopes, however, this pattern is reversed and the prolate minimum lies above the oblate one. The calculated values of the prolate-oblate energy difference,  $\Delta E_{\text{po}}$ , are rather sensitive to various model parameters. Figure 37 shows  $\Delta E_{\text{po}}$  for the Hg isotopes as a function of neutron number (414). Three variants of NS model calculations are displayed: the WS model results (*solid curve*), the results of the MO model with standard parameters (*dash-dotted curve*), and the MO results with potential parameters slightly adjusted to reproduce single-particle states in the Pt-Hg region (*dashed curve*). For comparison, energies for the excited  $0^+$  states deduced from experiments are also given. One can see that the experimental tendency is rather well reproduced by both models, with the deviation between experiment and theory being of the order of a few hundred keV. Of course, the comparison cannot be too quantitative as the static theory does not take into account many important effects, such as mixing between  $0^+$  states with different deformations or coupling to pairing vibrations [experimentally, the interaction between prolate and oblate states in Pt isotopes is around 200–400 keV (416)].

In the odd- $A$  Ir and Au nuclei, the odd proton can be coupled either to prolate (Pt) or to oblate (Hg) even-even cores. The calculated band head

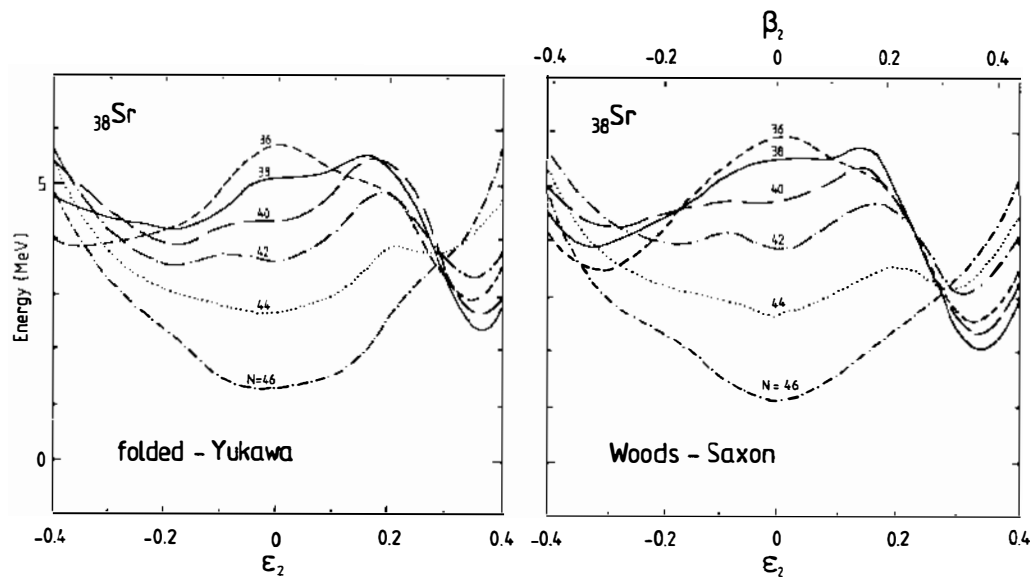


Figure 36 Calculated PES curves along the  $\epsilon_2$  coordinate for Sr isotopes with  $N = 36-46$ . The NS calculations are performed with the folded Yukawa potential (left) and the Woods-Saxon potential (right). (From 204.)

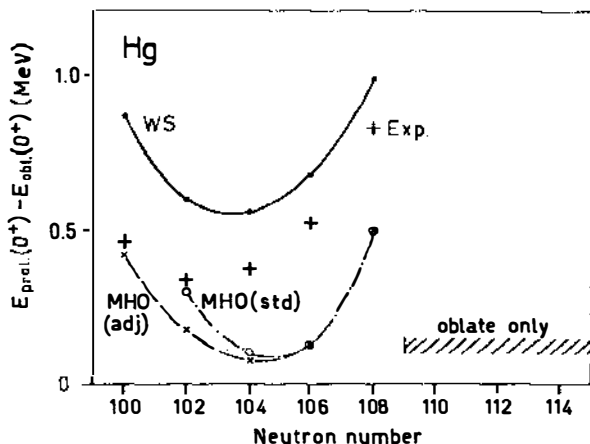


Figure 37 The prolate-oblate energy difference in even Hg isotopes. For  $N \geq 110$  only the oblate minimum exists. The NS calculations were performed with two different potentials: WS and MO [the latter ones were performed with a standard set of parameters (std) and adjusted parameters (adj)]. The observed excitation energies of coexisting  $0^+$  configurations are indicated by crosses. (From 414; the added experimental point for  $^{180}\text{Hg}$  comes from 414a.)

energies (see 217, 221, 372, 406, 407 and references therein) have equilibrium deformations that change from state to state. In particular, there are prolate and oblate 1qp configurations competing with each other. The recent experimental data for light gold isotopes indicate that the prolate-to-oblate shape transition takes place just around  $^{185}\text{Au}$  (299, 417, 418).

## 7.2 Spherical-Deformed Shape Isomers

The deformed intruder states in magic or semi-magic nuclei with spherical ground states provide spectacular examples of shape isomerism. The best cases can be found around  $N = 28$ ,  $Z = 50$ ,  $Z = 82$ , and in the nuclei from the  $Z = 40$  and  $Z = 64$  subshell regions. The current status of experimental data and a phenomenological shell model interpretation are presented in a series of papers by Heyde et al (217, 419–421). The deformed intruder states can be viewed as np-nh excitations through the closed shells. In the language of the deformed shell model, these states can be associated with strongly deformation-driving, high- $j$  Nilsson orbitals that, because of their large quadrupole moment, cross the single-particle gaps and become occupied at well-deformed shapes. The excited  $0^+$  states in the Sn isotopes or the  $\frac{9}{2}^+$  states in the odd- $A$  isotopes of Sb and I are representative examples of such a structure. They are associated with  $\pi g_{9/2}$  and  $\pi d_{5/2}$  configurations (217, 419, 422). A detailed analysis of intruder states is

beyond the scope of this study, in the following we concentrate mainly on the zirconium and lead nuclei.

In the heavy zirconium region ( $A \approx 100$ ) a sharp shape transition from sphericity to the deformed regime takes place at  $N = 58$  (e.g. 423). The calculations based on several variants of the shell correction method (123, 124, 126, 206, 285, 324, 364, 395, 424–428) and HF approach (74, 429) show the great sensitivity of the model predictions, especially for transitional nuclei such as  $^{96,98}\text{Zr}$ . The onset of quadrupole deformation around  $N = 58$  can be understood in terms of an interplay between the spherical  $Z = 40$ ,  $N = 56$ , and the deformed  $Z = 40$ ,  $N = 60$  closures in the single-particle spectrum (206, 430) (see also Section 8.1 for more discussion). In order to illustrate the sensitivity of calculated PES in this region to the choice of model parameters, we show in Figure 38 the total energy curves versus  $\beta_2$  for  $^{96,98,100}\text{Zr}$ . In the left portion the standard set of spin-orbit parameters are used. In this case, the PES of  $^{96}\text{Zr}$  has a very shallow spherical or nearly spherical minimum, while that of  $^{98}\text{Zr}$  exhibits a minimum at large deformation. With the new parameters (right side of the figure) the results agree better with the experimental trend. Indeed, they lead to an increase of the  $Z = 40$  and  $N = 56$  spherical gaps, which stabilizes the spherical configuration. Similar results have also been found in the HF calculations of Bonche et al (74 and Figures 3, 4, and 11 therein).

In the lead isotopes the intruder states have been associated with a  $2p$ - $2h$  proton excitation across the  $Z = 82$  gap to the  $h_{9/2}$  subshell (420, 421, 431). These states have been successfully interpreted with a phenomeno-

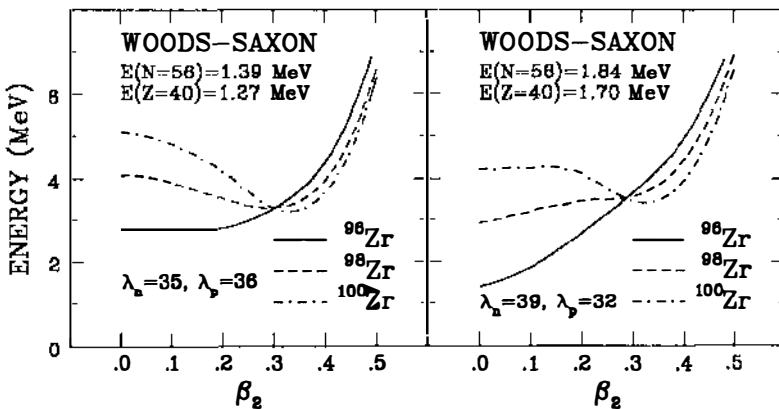


Figure 38 WS calculation of PES for  $^{96,98,100}\text{Zr}$ . In the left side, standard parameters have been used, while in the right diagram the strength of the spin-orbit potential has been adjusted to reproduce the spherical-deformed shape transition around  $N = 58$ . (From 206.)

logical shell model using a residual neutron-proton  $Q$ - $Q$  interaction (see Section 8.1) plus a monopole pairing force (420, 421). In particular, there is evidence for a scaling of the excitation energy of intruder states with the number of particle-hole pairs forming the intruder configuration.

The mean field calculations for Pb isotopes predict spherical minima in all the cases (415, 431, 432). However, in the neutron-deficient isotopes the calculations yield a very shallow prolate minimum with deformation  $\beta_2 \approx 0.28$ . In addition, they find a flat region in the PES at oblate shape at  $\beta_2 \approx -0.17$ , which does not, however, develop into a local minimum. A one-dimensional PES for  $^{186}\text{Pb}$  is presented in Figure 39 as a function of  $\beta_2$ . The energy minimum at prolate shape corresponds to the filling of low- $\Omega$  proton Nilsson levels originating from the  $h_{9/2}$  and  $f_{7/2}$  subshells. On the other hand, the origin of the flat region at oblate shape is connected with the filling of the oblate-driving  $[505\ 9/2] h_{9/2}$  level. This Nilsson orbital is well known to form a low-lying oblate-deformed  $I^\pi = \frac{9}{2}^-$  state in the TI

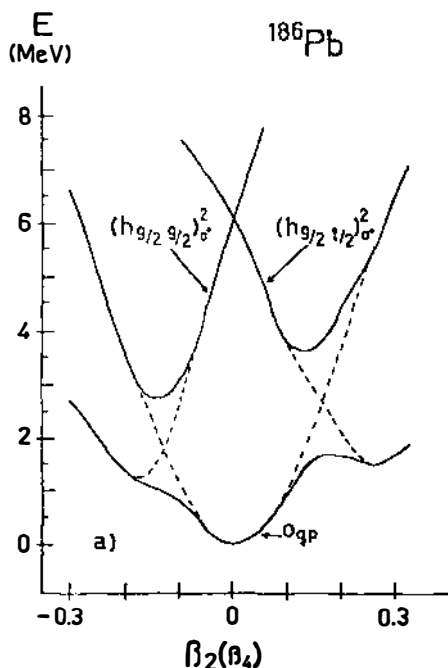


Figure 39 Adiabatic (solid curves) and diabatic (dashed curves) PES for  $^{186}\text{Pb}$ . The excited configurations correspond to the excitation of a proton pair to the  $h_{9/2}$  orbital. For each  $\beta_2$ , the energy has been minimized with respect to  $\beta_4$ . (From 432.)

isotopes (for calculations, see 217, 372, 415, 432–434). The potential-energy curves for the lowest two-quasi-particle proton excitations involving  $h_{9/2}$  proton orbitals are also shown in Figure 39. There is a crossing with large matrix element between the  $0_{qp}$  and  $\pi(h_{9/2})^2$  configurations. The magnitude of the configuration-mixing matrix element depends on the value of the proton pairing gap, which smoothes out the sharp crossing between corresponding Nilsson orbitals. This leads to a gradual increase of the  $h_{9/2}$  proton occupation in the vacuum configuration. By freezing the occupation numbers of the crossing single-particle levels either to 1 or to 0, it is possible to generate two configurations; one in which the  $h_{9/2}$  level is occupied by a pair of particles and one in which it is empty. In this way, one prevents the scattering of particles in and out from these levels, which is due to the pairing interaction. [Chasman (435) demonstrated that the pairing force matrix elements between intruder states are large as compared to the matrix elements between intruder and normal parity orbitals.] The associated diabatic curves are shown by the dashed lines in Figure 39. Bengtsson et al (432, 436) discuss this procedure and give more examples.

In Figure 40, the evolution of the excitation energies of the lowest  $\pi(h_{9/2})^2$  diabatic configurations in Pb isotopes is compared with that of the experimental intruder  $0^+$  states. More support for the deformed shell model interpretation comes from the recent measurements of monopole

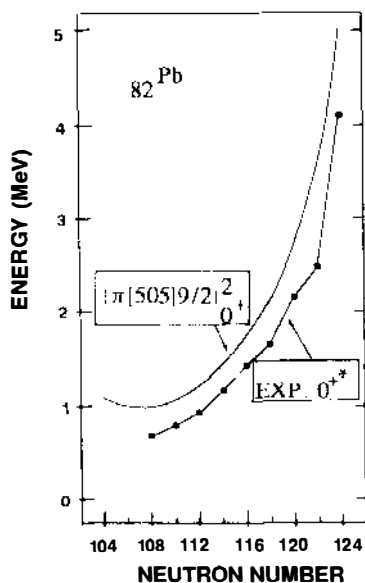


Figure 40 Excitation energies of  $0^+$  intruder states in Pb isotopes with  $N = 104$ –124. The experimental  $0^+$  energies are compared to the calculated ones, see Figure 39. The ground states are spherical while the excited  $\pi(h_{9/2})^2$  intruder states are oblate. (From 432.)

transitions in  $^{190,192,194}\text{Pb}$  (437). The measured E0 values are fairly consistent with calculated deformations of intruder states and the configuration-mixing matrix element turns out to be very small ( $\sim 50\text{--}80\text{ keV}$ ). Let us mention finally that similarities between the spherical and deformed shell model approach for intruder states were recently discussed by Heyde et al (438).

### 7.3 *Pairing Isomers*

It is well known that subshell effects can decrease substantially the magnitude of pairing correlations. Indeed, the pairing gap is approximately related to the level density around the Fermi level,  $g(\lambda_F)$ , by the formula  $\Delta \propto \exp\{-1/[Gg(\lambda_F)]\}$  in which  $G$  denotes the monopole pairing strength (43). In particular, if the single-particle gap is too large the BCS equations break down and have just the trivial HF solution (i.e.  $\Delta = 0$ ). In multiple-quasi-particle configurations, the reduction of the number of single-particle states available for pairs of nucleons (blocking effect) generates an additional decrease of the pairing correlations. In the mean field approach, the total energy is minimized with respect to some set of deformation parameters. At certain deformations, the static pairing can disappear because of the reduced single-particle level density or the blocking effect, or both. This leads to unphysically large variations in pairing energy. Of course, because of dynamical pairing fluctuations (pairing vibrations), such an abrupt transition from superfluid to normal phase never occurs in a system with a small particle number, like the atomic nucleus. Such dynamical correlations are to some extent accounted for by particle-number-conserving approaches (random phase approximation, RPA, or generator coordinate method, GCM) or particle number projection methods. As said before, this situation is in many respects analogous to that of transitional nuclei, whose dynamics is neither vibrational nor rotational. Indeed for these nuclei, the standard mean field approach ceases to be valid and shape fluctuations have to be taken into account.

One of the best examples of the local collapse of pairing can be found in the Hg isotopes. It has been predicted that at the oblate minima the proton pairing will disappear because of the large  $Z = 80$  single-particle gap (408, 410, 412). The same calculations find a large static proton pairing at the prolate shape minima. For such a situation one may introduce the notion of pairing isomers, i.e. two or more coexisting configurations with very different values of the static pair field (408, 439). In this case the two configurations are in fact both shape isomers and pairing isomers. A typical example of pairing isomeric states is shown in Figure 41, which presents the calculated values of the pairing gap versus  $\beta_2$  in selected one-quasi-proton configurations of  $^{99}_{39}\text{Y}$  (206). Because of the large  $Z = 38$  gap



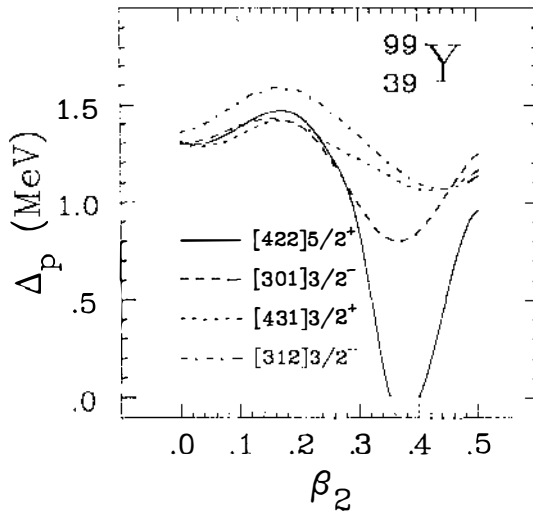


Figure 41 Proton pairing gaps vs quadrupole deformation for different configurations in  $^{99}\text{Y}$ . (From 206.)

at prolate shape, dramatic reduction of proton pairing is seen at the [422 5/2] and [301 3/2] configurations. Experimentally, rotational bands built upon these configurations exhibit unusually large and almost constant moments of inertia, which can be explained in terms of reduced pairing correlations (see 206, 389, 440). These results thus provide a remarkable example of the pairing isomerism phenomenon.

## 8. OTHER INTERACTIONS

In this section we discuss some separable interactions of interest in mean field calculations. In Section 8.1 we discuss the role of the neutron-proton interaction, and in Section 8.2 higher multipole moments both in the ph and pp directions.

### 8.1 Neutron-Proton Interaction

For more than three decades it has been claimed that nuclear deformation is solely determined by the competition between a long-range, deformation-driving ph  $T = 0$  interaction acting mostly between strongly overlapping neutron and proton orbitals and a  $T = 1$  pairing force that drives shapes toward sphericity (441, 442). Within this picture, inspired by the shell model, the largest matrix elements of the neutron-proton (n-p) interaction act between states with identical principal and orbital quantum

numbers,  $N_n = N_p$ ,  $l_n = l_p$ ; for instance, the  $\nu 1g_{9/2}$  and  $\pi 1g_{9/2}$  subshells. According to Federman & Pittel (443), the n-p spin-orbit partners represent another type of strongly interacting orbitals such as the  $\nu 1g_{7/2}$  and  $\pi 1g_{9/2}$  orbitals, which are responsible for the onset of stable deformations around  $^{100}\text{Zr}$  (see 389 and references therein).

At first sight, this picture is in marked contrast with the basic assumption of the mean field method, which states that nuclear deformations and low energy collective dynamics are due to a strong  $Q$ - $Q$  interaction between all valence particles. In the  $A \approx 80$  as well as in the  $A \approx 100$  mass region, the mean field theory attributes the observed nuclear deformations to a spontaneous symmetry breaking mechanism caused by gaps in the proton and neutron Nilsson spectra. Nuclear deformation is determined by the size of a shell correction calculated as the sum of independent proton and neutron contributions, and the n-p interaction does not appear explicitly. In fact, it is hidden within the specifics of the parametrizations of both the macroscopic energy and the average mean field. In particular, the well-known repulsive character of the isovector multipole-multipole interaction is implicitly accounted for by the requirement of identical deformations for the proton and neutron average potentials (7, 444).

In fact, one can show that the n-p force is the leading component of the  $Q$ - $Q$  interaction. Let us consider the commonly used phenomenological quadrupole-plus-pairing Hamiltonian, which consists of a spherical part,  $H_0$ , and  $Q$ - $Q$  isoscalar and isovector terms:

$$H = H_0 + \frac{\kappa_0}{2} Q_0 Q_0 + \frac{\kappa_1}{2} Q_1 Q_1, \quad 22.$$

where  $Q_0 = Q_n + Q_p$  and  $Q_1 = Q_n - Q_p$  are the single-particle quadrupole isoscalar and isovector operators, respectively. The values of the coupling constants  $\kappa_{0,1}$  valid for low-energy collective dynamics can be determined by an adjustment of the harmonic oscillator model predictions to the data (7, 444, 444a, 445). Since the ratio  $\kappa_1/\kappa_0$  is approximately  $-0.66$ , the  $Q$ - $Q$  part of the Hamiltonian (Equation 22) can be written as (445)

$$H_{Q-Q} = \frac{\kappa}{2} (Q_n Q_n + Q_p Q_p) + 5\kappa Q_n Q_p; \quad 23.$$

here  $\kappa_n = \kappa_p = \kappa = \kappa_0 + \kappa_1$ . One can thus conclude that the  $T = 0$  component of the  $Q$ - $Q$  force is much larger than the  $T = 1$  part.

Within more microscopic approaches, the origin of nuclear deformation can be looked for in the properties of the effective nucleon-nucleon force. By evaluating the contributions of different multipolarities and isospin to the mean field, one can determine the importance of the n-p force. Such a

study was recently carried out by Dobaczewski et al (445, 446) within the Skyrme HF method. Figure 42 presents different contributions to the total energy of  $^{72}\text{Ge}$ ,  $E_L^{\tau\tau} = \text{Tr}[\rho_L^\tau \text{Tr}(V\rho_L^\tau)]/(1 + \delta_{\tau\tau})$ , as functions of  $Q_0$ . The total energy results from a subtle balance between the monopole term  $\delta E_0 = E_0 - E_0(Q_0 = 0)$ , which increases with  $Q_0$ , and the quadrupole term  $E_2$ , which decreases with  $Q_0$ . The latter can also be related to the  $Q$ - $Q$  interaction responsible for nuclear deformation. Figure 42 shows also that the n-p  $Q$ - $Q$  interaction is about five times stronger than the sum of the unlike-particle components, in agreement with the simple estimate of Equation 23.

It is well known that many collective nuclear properties show remarkably smooth behavior when plotted versus the product of  $N_p N_n$ , the numbers of valence neutron and proton pairs (448, 449). The relation between  $N_p N_n$  and quadrupole collectivity is usually understood as an indication that the n-p interaction is the main factor in determining the nuclear deformation [in the generalized seniority scheme the expectation value of the  $Q_p Q_n$  force is roughly proportional to  $N_p N_n$  (see 420, 421, 450)]. It has been shown that the variation within a major shell of the calculated total quadrupole stiffness is correlated with the product  $N_p N_n$  (445, 446). However, the interpretation of this microscopic analysis remains difficult.

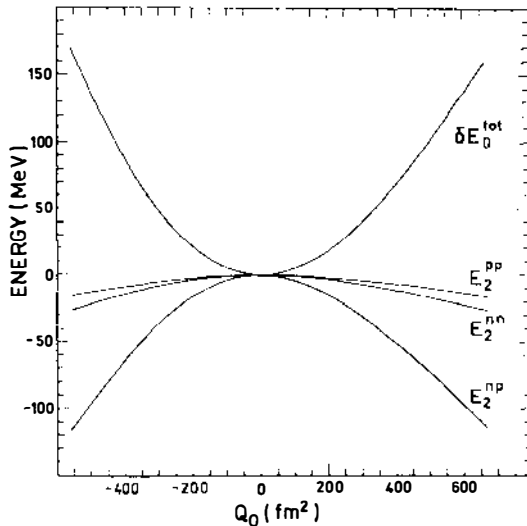


Figure 42 Contributions of different multipolarity  $L$  and isospin  $\tau$ ,  $E_L^{\tau\tau}$ , to the total energy of  $^{72}\text{Ge}$  plotted vs the mass quadrupole moment,  $Q_0$ , as obtained from Skyrme III HF calculations. (From 445.)

Indeed the quadrupole component of the effective interaction appears to depend only weakly on the shell structure. In fact, the monopole term is the determining factor in the variation of the quadrupole stiffness.

It is important to note that the high- $j$  intruder subshells, such as  $\nu 1h_{11/2}$  and  $\pi 1g_{9/2}$ , do obey the shell model criteria (441) for strongly overlapping orbitals. Keeping this in mind, one can interpret the deformation onset in terms of the deformed shell model picture (206). An inspection of the Nilsson diagram (Figure 2) shows that nuclear deformation generally sets in when neutron and proton intruder subshells are being occupied simultaneously. For example, in the heavy Zr region, the deformation sets in around  $N = 60$  and  $Z = 40$  when neutrons occupying the  $[550\ 1/2]$  and  $[541\ 3/2]$  Nilsson states interact with the  $[440\ 1/2]$  and  $[431\ 3/2]$  protons (see also 421, 451).

Let us comment briefly on the neutron-proton interaction in the particle-particle, hole-hole channel ( $T = 0$  pairing). The first studies, which introduced the quasi-particle formalism for both  $T = 0$  and  $T = 1$  pairs were mostly confined to doubly even  $Z = N$  nuclei in the sd shell (452–457). They showed the importance of the n-p pairing for this region of the chart of elements. In fact, the role played by the  $T = 0$  pairing depends strongly on the neutron excess. For  $Z = N$  systems the  $T = 0$  pairing mode is more important than a  $T = 1$  mode (454–458). For nuclei with small neutron excess,  $N - Z = 2$ , a  $T = 0$  pairing is comparable to a  $T = 1$  pairing (456) and for heavier  $N > Z$  nuclei, where protons and neutrons at the Fermi surface are in different spatial states, a  $T = 1$  pair field dominates.

As in n-n and p-p pairing, the n-p pairing correlations tend to decrease nuclear deformations (454). Goodman et al (455, 457) discussed the n-p pairing between the particles moving in time-reversed states  $(\alpha, \bar{\alpha})$  or in identical states  $(\alpha, \alpha)$ . While the  $(\alpha, \bar{\alpha})$   $T = 0$  pairing tends to stabilize axial shapes, the  $(\alpha, \alpha)$  correlations favor triaxial deformations in the mean field ground state.

The concept of a  $T = 0$  pairing has interesting high-spin consequences. The cranked HFB formalism for a  $T = 0$  pairing was developed by Nichols & Sorensen (459), who employed it for sd shell nuclei. This study was then pursued by other authors (460, 461). The results of calculations for  $Z = N$  nuclei show that a  $T = 1$  pairing is destroyed at lower angular momentum than a  $T = 0$  pairing (459–462). Indeed, the Coriolis force easily breaks pairs of particles in time-reversed orbitals, but it does not affect n-p pairs built on identical space-spin states. As a consequence, the n-p pairing survives to very high spin.

A  $T = 0$  pairing force can lead to a shift of band-crossing frequency, especially in light nuclei with  $Z \approx N$  (463), as well as a mixing between

quasi-proton and quasi-neutron configurations (e.g. between proton and neutron *s* bands) (464).

## 8.2 Higher Deformations

Both experimentally and theoretically, very little is known about the surface multipole moments of order higher than four. For  $\lambda = 6$  (hexacontatetrapole), some evidence exists based on  $(\alpha, \alpha')$  (465–467) and  $(p, p')$  (468–470) experiments. From the simple shell model arguments it follows that the total intrinsic moment of even multipolarity  $\lambda$  should change sign  $[(\lambda/2) - 1]$  times within a major shell (471). It is well known, for instance, that for well-deformed systems  $\beta_2$  is always positive, and  $\beta_4$  changes sign once near mid shell. Consequently, one expects  $\beta_6$  to change sign twice within a major shell. Initial microscopic calculations of equilibrium  $\beta_6$  deformations by Nilsson et al (472) reproduced this trend qualitatively, and the recent experimental data for deformed Th and U nuclei give some evidence for a sign change near  $A = 240$  (470).

The equilibrium values of  $\beta_6$  deformations have been computed for those nuclei of the heavy Ba and Ra-Th regions, which exhibit a marked reflection asymmetry instability (see Section 6) (118, 280, 331, 333, 337). In general,  $\beta_6$  is positive ( $\sim 0.02$ ) for light actinides with  $130 \leq N \leq 140$  and negative ( $\sim -0.01$ ) for Xe-Sm nuclei with  $86 \leq N \leq 94$ . At any rate, and before any comparison with data, it is important to remember that the presence of odd-multipolarity deformations in the mean field may significantly affect the equilibrium value of  $\beta_6$  (334, 337) and thus destroy the simple pattern (471) valid for well-deformed reflection-symmetric nuclei.

The shell correction energy has been plotted as a function of  $\beta_6$  (e.g. 364). In general, the shell effects associated with  $\beta_6$  are weak. However, there is a sizeable deviation between the calculated equilibrium values of  $\beta_6$  and those that only minimize the macroscopic part of the nuclear energy (325, 408).

There are almost no experimental data available on moments with  $\lambda > 6$ . For example, Barlett et al (469) gave the value  $\beta_8 = 0.008$  for  $^{176}\text{Yb}$ , but it is very uncertain because it depends strongly on various model assumptions used. For calculated values of  $\beta_8$  in the region of light actinides, see (333).

The higher deformations in the *pp* direction are associated with multipole pairing forces. The strength of the quadrupole pairing component is estimated to be around five times smaller than the monopole pairing coupling constant (8, 13). Quadrupole pairing plays an important role in the description of pairing vibrations (143, 473, 474). It has also been employed in the NS calculations of equilibrium deformations and fission

barriers (402, 475). However, as Nilsson et al (402) pointed out, the quadrupole pairing energy shows an unphysical increase at large deformations and a deformation-dependent renormalization of the coupling constant  $G_2$  is necessary.

Multipole pairing forces influence both the magnitude and the frequency dependence of the moment of inertia (174, 476–481). Hamamoto (478, 479) and Wakai & Faessler (480) investigated the frequency dependence of different magnetic components of the quadrupole pairing field. They demonstrated the anticorrelation effect between the  $Y_{20}$  and  $Y_{2\pm 1}$  modes. In addition to the monopole and quadrupole pairing fields, the high-spin behavior of the higher pairing components (4, 6, ...) of the surface delta interaction has also been discussed (460, 461, 481). The higher pp deformations survive, in general, to much higher frequencies than the monopole pairing field. The monopole pairing field is discussed in Section 5 and in the work of Shimizu et al (182).

Experimentally, there is some evidence for configuration-dependent pairing from the analysis of the crossing frequencies in lqp rotational bands. It has been shown that the crossing frequencies are correlated with the sign and magnitude of the quadrupole moments of the valence nucleons (481–484).

## 9. NEW DEVELOPMENTS

### 9.1 *The Configuration Concept*

The results of mean field calculations presented in Sections 5 and 7 suggest that physical states can be related to very shallow minima of the PES, or even to shell structures that do not generate a proper minimum. In the latter case, it appears that the energy of excited states can be estimated by removing the interaction between the different quasi-particle configurations. This has many important consequences. In standard mean field calculations, the total energy is minimized with respect to some set of deformation parameters describing the shape of a nucleus. When calculations are not constrained to a particular intrinsic shell model configuration, the resulting PES will be (in first approximation) the lower envelope of the set of PES associated with all possible configurations. This means that the original symmetries of the Hamiltonian are not sufficient to distinguish the physically interesting shell model structures. It is therefore necessary to introduce auxiliary quantum numbers. Because the high- $j$  intruder orbitals have a very distinct structure, one can label the important intrinsic configurations according to the number of occupied intruder orbitals. Examples of such calculations are presented in Figures 13, 18, 24, and 39. In order to study a given structure, one should also keep track

of diabatic trajectories as a function of the deformation parameters (or constraints in HFB calculations). In particular, a new procedure must be elaborated to calculate the PES at those deformations for which natural and abnormal parity orbitals cross. Such an extension of the mean field approach, referred to as the configuration-constrained mean field approach, has been successfully applied to many systems in various regimes of angular momentum and deformation (204, 209, 214, 223a, 415, 430, 432, 436, 485–487).

A particularly interesting example of the unique role of high- $j$  orbits is seen in superdeformed high-spin nuclei (Section 5.6). No spin or parity assignments have yet been made experimentally, but configurations have still been assigned. This was done in terms of the number of particles in high- $j$  shells (or rather high- $N$  shells) (see 263). In the NS calculations of superdeformed states, this configuration concept works well and largely facilitates the shape identification of individual bands.

Another example in which the configuration concept is important is band termination (Section 5.4). In order to trace a specific rotational band to its termination in a mean field calculation, the configuration must be specified as detailed as possible (see Figure 13).

The success of these phenomenological methods, inspired and strongly supported by data, leads one to question one of the underlying assumptions of most theoretical approaches of the collective nuclear motion: the adiabatic hypothesis. This problem may be one of the most important we shall have to address in the coming years.

## 9.2 *Relativistic Mean Field*

In recent years it has been shown that ground-state properties of nuclear matter and of closed-shell nuclei can be described within a mean field approximation to a relativistic quantum field theory of nucleons (488). A simple, relativistic, effective Lagrangian usually consists of Dirac nucleons and several massive mesons producing an interaction: phenomenological attractive scalar mesons  $\sigma$ , repulsive vector mesons  $\omega$ , and isovector-vector mesons  $\rho$ . The nucleons move in classical meson fields, which are given in a self-consistent way by nucleonic densities and currents.

Only recently has the relativistic mean field (RMF) theory been applied to deformed nuclei. First studies have been concerned with axially and reflection-symmetric shapes of light nuclei (489–492).

The RMF calculations have also been applied to the axially deformed and reflection-symmetric heavy systems, Gd and Er nuclei (493, 494), as well as to the triaxial shapes in  $^{24}\text{Mg}$  (495). Let us also mention the first relativistic high-spin calculations by means of cranking prescription (496), which have been carried out for  $^{20}\text{Ne}$ . As compared to the nonrotating

case, the resulting equations of motion are modified by the familiar cranking term,  $-\omega I$ , in the Dirac equation and a quadratic term,  $-(\omega I)^2$ , in the Klein-Gordon equations for the fields (496).

Although the preliminary results of RMF theory calculations are encouraging, many problems still remain to be solved, both conceptual (i.e. the treatment of the contribution from the Dirac sea) and technical [i.e. the proper parametrization of the effective Lagrangian (493, 494) and the inclusion of pp-type interactions].

## 10. BEYOND THE MEAN FIELD APPROACH

The mean field method incorporating collective effects—either by addition of shape-constraining operators to the Hamiltonian as in the HF method, or by selection of appropriate deformations for the single-particle well as in the NS method—appears to generate the optimal particle or quasi-particle basis needed for the description of discrete nuclear spectroscopy. Nevertheless, it must be complemented in order to include effects of missing many-body correlations. We have already mentioned that the description of deformation or pairing correlations implies a breaking of the symmetry of the Hamiltonian. Although the presence of these symmetries is approximately taken into account by the addition of constraints on the angular momentum or the particle number, it is sometimes necessary to restore them exactly (499). This is especially true for the particle number symmetry because the distribution of given  $(N, Z)$  components contained in a nuclear BCS many-body wave function is rather narrow (a few nucleon number units) (8). Projected wave functions are obtained by a configuration mixing of all the energy-degenerate mean field states associated with the symmetry. The weight function of this mixing is determined by the properties of the group generated by the symmetry operator ( $I_x$  or  $N$ ). A natural extension will introduce the mixing of non-energy-degenerate mean field solutions. This is the generator coordinate method (GCM) (107), which can also be combined with projection (58). In the GCM, one constructs a wave function that incorporates the dynamical correlations and the quantal fluctuations along the collective path. The GCM weight function must be determined dynamically; this is accomplished by the so-called Hill-Wheeler integral equation. The GCM is fully quantal, but the quality of its predictions depends ultimately on a proper choice of the collective path.

Although we have strong evidence that discrete nuclear spectroscopy is associated with low-multipole nuclear deformations and angular momentum cranking, it would certainly be preferable to derive the collective constraining operator directly from the nuclear effective Hamiltonian. This is one of the goals of the adiabatic time-dependent Hartree-Fock method



(ATDHF) (30, 33, 500, 501). Based on an expansion of the time-dependent Hartree-Fock method (TDHF) to second order in the time-odd components of the one-body density matrix, this method simultaneously determines the collective path and the dynamics along this path. It also provides a natural connection between microscopic theories based on nucleon-nucleon effective interaction (HF, HFB, TDHF) and the very successful Bohr Hamiltonian method, or the random phase approximation (RPA). Up to now, GCM and ATDHF have been considered mostly as providing a conceptual understanding of more phenomenological methods. They have not been used extensively for the study of nuclear spectroscopy. In view of the recent (and expected) exciting developments in this field, they will likely be used more and more often in the near future, in order to determine the amplitude of those correlations effects not accounted for by the mean field.

#### ACKNOWLEDGMENTS

George Dracoulis and Ingemar Ragnarsson are acknowledged for valuable comments on the manuscript. This project has been supported by the Swedish Natural Science Research Council (NFR) and the Polish Ministry of National Education under contract CPBP01.09.

#### Literature Cited

1. Rainwater, J., *Phys. Rev.* 79: 432 (1950)
2. Bohr, A., *Phys. Rev.* 81: 134 (1952)
3. Bohr, A., Mottelson, B. R., *Phys. Rev.* 89: 316 (1953)
4. Bohr, A., Mottelson, B. R., *Phys. Rev.* 90: 717 (1953)
5. Bohr, N., Kalckar, F., *Mat. Fys. Med. Dan. Vid. Selsk.*, Vol. 14, No. 10 (1937)
6. Bohr, A., Mottelson, B. R., *Nuclear Structure*, Vol. I. New York: Benjamin (1969)
7. Bohr, A., Mottelson, B. R., *Nuclear Structure*, Vol. II. New York: Benjamin (1975)
8. Ring, P., Schuck, P., *The Nuclear Many-Body Problem*. New York: Springer-Verlag (1980)
9. Szymański, Z., *Fast Nuclear Rotation*. Oxford: Clarendon (1983)
10. Garrett, J. D., et al., ed., *The Variety of Nuclear Shapes*, *Proc. Int. Conf. on Nucl. Shapes, Crete*. Singapore: World Scientific (1988)
11. Nilsson, S. G., Ragnarsson, I., *Shapes and Shells in Nuclear Structure*. Cambridge Univ. Press. In press (1990)
12. Sharpey-Schafer, J. F., Simpson, J., *Prog. Part. Nucl. Phys.* 21: 293-400 (1988)
13. Lane, A. M., *Nuclear Theory*. New York: Benjamin (1974)
14. Brückner, K. A., Levinson, C. A., Mahmoud, H. M., *Phys. Rev.* 95: 217 (1954)
15. Brückner, K. A., Lockett, A. M., Rotenberg, M., *Phys. Rev.* 121: 255 (1961)
16. Negele, J. W., *Phys. Rev. C*1: 1260-1321 (1970)
17. Campi, X., Sprung, D. W., *Nucl. Phys.* A194: 401-42 (1972)
18. Skyrme, T. H. R., *Philos. Mag.* 1: 1043 (1956)
19. Vautherin, D., Brink, D. M., *Phys. Rev. C*5: 626-47 (1972)
20. Gogny, D., In *Nuclear Self-Consistent Fields*, ed. G. Ripka, M. Porneuf. Amsterdam: North Holland (1975), p. 333
21. Beiner, M., et al., *Nucl. Phys.* A238: 29-69 (1975)
22. Stancu, I., Brink, D. M., Flocard, H., *Phys. Lett.* 68B: 108-12 (1977)
23. Negele, J. W., Vautherin, D., *Phys. Rev. C*5: 1472-93 (1972)
24. Negele, J. W., Vautherin, D., *Phys. Rev. C*11: 1031-41 (1975)
25. Sprung, D. W. L., et al., *Nucl. Phys.* A253: 1-19 (1975)

26. Elliott, J. P., *Proc. R. Soc. London* A245: 128, 562 (1958)
27. Kisslinger, L. S., Sorensen, R. A., *Rev. Mod. Phys.* 35: 853 (1963)
28. Kumar, K., Baranger, M., *Nucl. Phys.* A110: 529–54 (1968)
29. Baranger, M., Kumar, K., *Nucl. Phys.* A122: 241–72 (1968)
30. Villars, F., *Nucl. Phys.* A285: 269–96 (1977)
31. Baranger, M., *J. Phys.* 33: C5 (1972)
32. Marumori, T., *Prog. Theor. Phys.* 57: 112 (1977)
33. Baranger, M., Vénèroni, M., *Ann. Phys.* 114: 123–200 (1978)
34. Reinhard, P.-G., Goeke, K., *Nucl. Phys.* A312: 121–39 (1978)
35. Bohr, A., *Mat. Fys. Medd. Dan. Vid. Selsk.*, Vol. 26, No. 14 (1952)
36. Bassichis, W. H., Kerman, A. K., Svenne, J. P., *Phys. Rev.* 160: 746–52 (1967)
37. Cailliau, M., et al., *Phys. Lett.* 46B: 11–14 (1973)
38. Flocard, H., et al., *Nucl. Phys.* A231: 176–88 (1974)
39. Kolb, D., Cusson, R. Y., Schmitt, H. W., *Phys. Rev.* C10: 1529–47 (1974)
40. Mayer, M. G., *Phys. Rev.* 78: 22 (1950)
41. Bardeen, J., Cooper, L. N., Schrieffer, J. R., *Phys. Rev.* 108: 1175 (1957)
42. Bohr, A., Mottelson, B. R., Pines, D., *Phys. Rev.* 110: 936 (1958)
43. Belyaev, S. T., *Mat. Fys. Medd. Dan. Vid. Selsk.*, Vol. 31, No. 11 (1959)
44. Kerman, A. K., *Ann. Phys.* 12: 300 (1961)
45. Bogoliubov, N. N., *Sov. Phys. JETP* 7: 41 (1958)
46. Bogoliubov, N. N., *Usp. Fiz. Nauk* 67: 549 (1959)
47. Baranger, M., *Phys. Rev.* 122: 992 (1961)
48. Baranger, M., *Phys. Rev.* 130: 1244 (1961)
49. Valatin, J. G., *Phys. Rev.* 122: 1012–20 (1961)
50. Reinhard, P.-G., Otten, E. W., *Nucl. Phys.* A420: 173–92 (1984)
51. Elliott, J. P., Dawber, P. G., *Symmetry in Physics*, Vol. 2. London: Macmillan (1986)
52. Schmidt, H., *Varenna Lectures*, 44 pp. (1971)
53. Broglia, R. A., Hansen, O., Riedel, C., *Adv. Nucl. Phys.* 6: 287 (1973)
54. Bès, D. R., Broglia, R. A., *Varenna Lectures*, 69: 55 (1976)
55. Peierls, R. E., Yoccoz, J., *Proc. Phys. Soc. London* A70: 381 (1957)
56. Dietrich, K., Mang, H. J., Pradal, J. H., *Phys. Rev.* 135: B22–B34 (1964)
57. Yoccoz, J., *Varenna Lectures*, 36: 474 (1974)
58. Wong, C. W., *Phys. Rep.* 15C: 283–357 (1975)
59. Kamla, A., *Z. Phys.* 216: 52 (1968)
60. Beck, R., Mang, H. J., Ring, P., *Z. Phys.* 231: 26 (1970)
61. Mang, H. J., *Phys. Rep.* 18C: 325 (1975)
62. Islam, S., Mang, H. J., Ring, P., *Nucl. Phys.* A326: 161–81 (1979)
63. Thouless, D. J., Valatin, J. G., *Nucl. Phys.* 31: 211–30 (1962)
64. Villars, F., Schmeing-Rogerson, N., *Ann. Phys.* 63: 443 (1971)
65. Banerjee, B., Ring, P., Mang, H. J., *Nucl. Phys.* A221: 564–72 (1974)
66. Banerjee, B., Mang, H. J., Ring, P., *Nucl. Phys.* A215: 366–82 (1973)
67. Egidio, J. L., Mang, H. J., Ring, P., *Nucl. Phys.* A334: 1–20 (1980)
68. Egidio, J. L., Mang, H. J., Ring, P., *Nucl. Phys.* A339: 390–414 (1980)
69. Dechargé, J., Gogny, D., *Phys. Rev.* C21: 1568–93 (1980)
70. Egidio, J. L., Ring, P., *Nucl. Phys.* A383: 189–204 (1982)
71. Egidio, J. L., Ring, P., *Nucl. Phys.* A388: 19–36 (1982)
72. Girod, M., Grammaticos, B., *Phys. Rev.* C27: 2317–39 (1983)
73. Berger, J. F., Girod, M., Gogny, D., *Nucl. Phys.* A428: 23c–36c (1984)
74. Bonche, P., et al., *Nucl. Phys.* A443: 39–63 (1985)
75. Bonche, P., See Ref. 10, pp. 302–20
76. Ripka, G., *Adv. Nucl. Phys.* 1: 183 (1968)
77. Bohr, A., *Varenna Lectures* 69: 1 (1976)
78. Bohr, A., *Rev. Mod. Phys.* 48: 365–74 (1976)
79. Strutinsky, V. M., *Nucl. Phys.* A95: 420–42 (1967)
80. Strutinsky, V. M., *Nucl. Phys.* A122: 1–33 (1968)
81. Nilsson, S. G., *Mat. Fys. Medd. Dan. Vid. Selsk.*, Vol. 29, No. 16 (1955)
82. Mottelson, B. R., Nilsson, S. G., *Mat. Fys. Medd. Dan. Vid. Selsk.*, Vol. 1, No. 8 (1959)
83. Bès, D. R., Szymański, Z., *Nucl. Phys.* 28: 42–62 (1961)
84. Von Weizsäcker, C. F., *Z. Phys.* 96: 431 (1935)
85. Myers, W. D., Swiatecki, W. J., *Nucl. Phys.* 81: 1–60 (1966)
86. Polikanov, S. M., et al., *Sov. Phys. JETP* 15: 1016 (1962)
87. Vandenbosch, R., *Annu. Rev. Nucl. Part. Sci.* 27: 1–35 (1977)
88. Bjørnholm, S., Lynn, J. E., *Rev. Mod. Phys.* 52: 725–931 (1980)
89. Swiatecki, W. J., In *Proc. 2nd Int. Conf. on Nuclidic Masses*, Vienna, ed. W. H. Johnson, Jr. Vienna: Springer-Verlag (1964), 58 pp.
90. Bunatian, G. G., Kolomietz, V. M.,

- Strutinsky, V. M., *Nucl. Phys.* A188: 225–58 (1972)
91. Brack, M., et al., *Rev. Mod. Phys.* 44: 320–405 (1972)
  92. Strutinsky, V. M., *Nucl. Phys.* A218: 169–79 (1974)
  93. Brack, M., Quentin, P., *Phys. Lett.* 56B: 421–23 (1975)
  94. Bhaduri, R. K., *Phys. Rev. Lett.* 39: 329–32 (1977)
  95. Chu, Y. H., Jennings, B. K., Brack, M., *Phys. Lett.* 68B: 407–11 (1977)
  96. Brack, M., Quentin, P., *Nucl. Phys.* A361: 35–82 (1981)
  97. Bengtsson, R., et al., *Phys. Lett.* 57B: 301–5 (1975)
  98. Neergård, K., Pashkevich, V. V., *Phys. Lett.* 59B: 218–22 (1975)
  99. Neergård, K., Pashkevich, V. V., Frauendorf, S., *Nucl. Phys.* A262: 61–90 (1976)
  100. Andersson, G., et al., *Nucl. Phys.* A268: 205–56 (1976)
  101. Cohen, S., Plasil, F., Swiatecki, W. J., *Ann. Phys.* 82: 557 (1974)
  102. Sierk, A. J., *Phys. Rev.* C33: 2039–53 (1986)
  103. Bohr, A., Mottelson, B. R., In *Proc. Int. Conf. on Nucl. Struct.*, *J. Phys. Soc. Jpn. Suppl.* 44: 157 (1977)
  104. Bengtsson, R., Frauendorf, S., *Nucl. Phys.* A327: 139–71 (1979)
  105. Bengtsson, R., Garrett, J. D., In *Int. Rev. Nucl. Phys.*, Vol. 2. Singapore: World Scientific (1984), p. 193
  106. Frisk, H., Bengtsson, R., *Phys. Lett.* 196B: 14–18 (1987)
  107. Hill, D. L., Wheeler, J. A., *Phys. Rev.* 89: 1102 (1953)
  108. Skalski, J., To be published (1990)
  109. Larsson, S. E., et al., *Nucl. Phys.* A261: 77–92 (1976)
  110. Ansari, A., Civitarese, O., Faessler, A., *Nucl. Phys.* A334: 93–108 (1980)
  111. Rohozinski, S. G., Sobczewski, A., *Acta Phys. Pol.* B12: 1001 (1981)
  112. Nazarewicz, W., Rozmej, P., *Nucl. Phys.* A369: 396–412 (1981)
  113. Larsson, S. E., *Phys. Scr.* 8: 17–31 (1973)
  114. Bengtsson, R., et al., *Phys. Scr.* 39: 196–220 (1989)
  115. Pashkevich, V. V., *Nucl. Phys.* A169: 275–93 (1971)
  116. Götz, U., et al., *Nucl. Phys.* A192: 1–38 (1972)
  117. Nix, J. R., *Annu. Rev. Nucl. Part. Sci.* 22: 65–120 (1972)
  118. Chasman, R. R., et al., *Rev. Mod. Phys.* 49: 833–91 (1977)
  119. Pashkevich, V. V., *Nucl. Phys.* A477: 1–17 (1988)
  120. Nerlo-Pomorska, B., Pomorski, K., *Nukleonika* 22: 289 (1977)
  121. Dudek, J., Nazarewicz, W., Rozmej, P., *J. Phys.* G6: 1521–34 (1980)
  122. Dudek, J., Nazarewicz, W., Olanders, P., *Nucl. Phys.* A420: 285–96 (1984)
  123. Möller, P., Nix, J. R., *At. Data Nucl. Data Tables* 26: 165 (1981)
  124. Bengtsson, R., et al., *Phys. Scr.* 29: 402–30 (1984)
  125. Möller, P., Nix, J. R., *At. Data Nucl. Data Tables* 29: 402 (1988)
  126. Ragnarsson, I., Sheline, R. K., *Phys. Scr.* 29: 385–401 (1984)
  127. Campi, X., et al., *Nucl. Phys.* A251: 193–205 (1975)
  128. Détraz, C., Vicira, D. J., *Annu. Rev. Nucl. Part. Sci.* 39: 407–65 (1989)
  129. Tanihata, I., et al., *Phys. Lett.* 206B: 592–96 (1988)
  130. Ragnarsson, I., Åberg, S., Sheline, R. K., To be published (1990)
  131. Hansen, P. G., Jonson, B., *Europhys. Lett.* 4: 409–14 (1987)
  132. Davydov, A. S., Filippov, G. F., *Nucl. Phys.* 8: 237 (1958)
  133. Toki, K., Faessler, A., *Phys. Lett.* 63B: 121–24 (1976)
  134. Kumar, K., Baranger, M., *Nucl. Phys.* A122: 273–324 (1968)
  135. Zofka, J., Ripka, G., *Nucl. Phys.* A168: 65–96 (1971)
  136. Curry, P. D., Sprung, D. W. L., *Nucl. Phys.* A216: 125–44 (1973)
  137. Lassey, K., Manning, M., Volkov, A., *Can. J. Phys.* A51: 2522 (1973)
  138. Flerackers, E., Knuyt, G., Bouten, M., *Phys. Lett.* 67B: 139–40 (1977)
  139. Sandhu, T. S., Rustgi, M. L., *Phys. Rev.* C14: 675–81 (1976)
  140. Frois, B., et al., *Phys. Lett.* 122B: 347–50 (1983)
  141. Pashkevich, V. V., *Nucl. Phys.* A133: 400–4 (1969)
  142. Larsson, S. E., Ragnarsson, I., Nilsson, S. G., *Phys. Lett.* 38B: 269–73 (1972)
  143. Ragnarsson, I., et al., *Nucl. Phys.* A233: 329–56 (1974)
  144. Leander, G. A., Larsson, S. E., *Nucl. Phys.* A239: 93–113 (1975)
  145. Åberg, S., *Phys. Scr.* 25: 23–27 (1982)
  146. Götz, U., Pauli, H. C., Adler, K., *Nucl. Phys.* A175: 481–94 (1971)
  147. Ardouin, D., et al., *Phys. Rev.* C12: 1745–61 (1975)
  148. Girod, M., Grammaticos, B., *Phys. Rev. Lett.* 40: 261–64 (1978)
  149. Sahu, R., et al., *Phys. Rev.* C19: 511–20 (1979)
  150. Redon, N., et al., *Phys. Lett.* 181B: 223–28 (1986)
  151. Redon, N., et al., *Z. Phys.* A325: 127–38 (1986)
  152. Kern, B. D., et al., *Phys. Rev.* C36: 1514–21 (1987)

153. Redon, N., et al., *Phys. Rev. C*38: 550–52 (1988)
154. Soramel, F., et al., *Phys. Rev. C*38: 537–40 (1988)
155. Hayashi, A., Hara, K., Ring, P., *Phys. Rev. Lett.* 53: 337–40 (1984)
156. Bohr, A., Mottelson, B. R., *Phys. Scr.* A10: 13–20 (1974)
157. Ragnarsson, I., Nilsson, S. G., Sheline, R. K., *Phys. Rep.* 45: 1–87 (1978)
158. Åberg, S., et al., In *Physics and Chemistry of Fission*, Vol. I. Vienna: IAEA (1980), pp. 303–58
- 158a. Faessler, A., Płoszajczak, M., Schmid, K. W., *Prog. Part. Nucl. Phys.* 5: 79–142 (1981)
159. de Voigt, M. J. A., Dudek, J., Szymanski, Z., *Rev. Mod. Phys.* 55: 949–1046 (1983)
160. Hamamoto, I., In *Treatise on Heavy-Ion Science*, Vol. 3, ed. D. A. Bromley. New York: Plenum (1985), p. 313
161. Garrett, J. D., Hagemann, G. B., Herskind, B., *Annu. Rev. Nucl. Part. Sci.* 36: 419–73 (1986)
162. Marshalek, E. R., *Phys. Rev.* 139: B770–89 (1965)
163. Bengtsson, R., et al., *Nucl. Phys.* A405: 221–36 (1983)
164. Åberg, S., Bengtsson, R., In *Proc. 24th Int. Winter Meet. Nucl. Phys., Bormio, Italy, Ric. Sci. Educ. Permanente Suppl.* 49: 578 (1986)
165. Bengtsson, R., See Ref. 447, p. 317
166. Carpenter, M. P., et al., *Nucl. Phys. A* (1990) in print
167. Azgui, F., et al., *Nucl. Phys.* A439: 573–88 (1985)
168. Emling, H., et al., *Nucl. Phys.* A419: 187–220 (1984)
169. Kulesa, R., et al., *Phys. Lett.* 218B: 421–26 (1989)
170. Ring, P., et al., *Phys. Lett.* 110B: 423–27 (1982)
171. Onishi, N., et al., *Nucl. Phys.* A452: 71–92 (1986)
172. Grosse, E., et al., *Phys. Scr.* 24: 337–48 (1981)
173. Ower, H., et al., *Nucl. Phys.* A388: 421–44 (1982)
174. Egido, J. L., Ring, P., *Nucl. Phys.* A423: 93–120 (1984)
175. Czosnyka, T., In *Proc. Int. Conf. on Nucl. Struct. Through Static and Dynamic Moments*, Melbourne, ed. H. H. Bolotin. Melbourne: Conf. Proc. Press (1987), pp. 49–60
176. Cline, D., *Annu. Rev. Nucl. Part. Sci.* 36: 683–716 (1986)
177. Cline, D., See Ref. 10, pp. 1–20
178. Stephens, F. S., et al., *Phys. Rev. Lett.* 29: 438–41 (1972); Stephens, F. S., Simon, R. S., *Nucl. Phys.* A183: 257–84 (1972)
179. Johnson, A., Ryde, H., Sztarkier, J., *Phys. Lett.* 34B: 605 8 (1971)
180. Johnson, A., Ryde, H., Hjorth, S. A., *Nucl. Phys.* A179: 753–68 (1972)
181. Ring, P., See Ref. 447, pp. 677–98
182. Shimizu, Y. R., et al., *Rev. Mod. Phys.* 61: 131–68 (1989)
183. Frauendorf, S., May, F. R., *Phys. Lett.* 125B: 245–50 (1983)
184. Hamamoto, I., Mottelson, B. R., *Phys. Lett.* 127B: 281–85 (1983)
185. Bengtsson, R., et al., *Nucl. Phys.* A415: 189–214 (1984)
186. Hagemann, G. B., Hamamoto, I., *Phys. Rev.* 40C: 2862–69 (1989)
187. Matsuzaki, M., Shimizu, Y. R., Matsuyanagi, K., *Prog. Theor. Phys.* 79: 836 (1988)
188. Hamamoto, I., *Phys. Lett.* 179B: 327–31 (1986)
189. Ikeda, A., Shimano, T., *Phys. Rev. Lett.* 63: 139–42 (1989)
190. Chen, Y. S., Frauendorf, S., Leander, G. A., *Phys. Rev. C*28: 2437–45 (1983)
191. Leander, G. A., Frauendorf, S., May, F. R. 1983. In *Proc. Int. Conf. on High Angular Momentum Properties of Nuclei, Oak Ridge*, ed. N. R. Johnson. New York: Harwood Academic (1983), p. 281
192. Chen, Y. S., *Nucl. Phys.* A421: 403c–18c (1984)
193. Paul, E. S., et al., *Phys. Rev. Lett.* 58: 984–87 (1987)
194. Wyss, R., et al., *Z. Phys.* A329: 255–56 (1988)
195. Wyss, R., et al., *Nucl. Phys.* A505: 337–51 (1989)
196. Funke, L., et al., *Phys. Lett.* 120B: 301–4 (1983)
197. Lühmann, L., et al., *Phys. Rev.* C31: 828–42 (1985)
198. Hüttmeier, U. J., et al., *Phys. Rev.* C37: 118–31 (1988)
199. Moore, E. F., et al., *Phys. Rev.* C38: 696–711 (1988)
200. Winter, G., et al., *J. Phys.* G14: L13–L18 (1988)
201. Tabor, S. L., et al., *Phys. Rev.* C39: 1359–70 (1989)
202. Mylaeus, T., et al., *J. Phys.* G15: L135–41 (1989)
203. Gross, C. J., et al., *Nucl. Phys.* A501: 367–400 (1989)
204. Nazarewicz, W., et al., *Nucl. Phys.* A435: 397–447 (1985)
205. Bengtsson, R., Nazarewicz, W., In *Proc. 19th Winter Sch. on Phys., Zakopane*, Rep. IFJ No. 1268, ed. Z. Stachura (1984), p. 171
206. Nazarewicz, W., Werner, T., See Ref. 296, p. 277
207. Recht, J., et al., *Nucl. Phys.* A440: 366–96 (1985)

208. Lieder, R. M., et al., *Nucl. Phys.* 476: 545–88 (1988)
209. Ragnarsson, I., Åberg, S., Sheline, R. K., *Phys. Scr.* 24: 215–35 (1981)
210. Bengtsson, R., et al., In preparation (1990)
211. Nolan, P. J., Twin, P. J., *Annu. Rev. Nucl. Part. Sci.* 38: 533–62 (1988)
212. Kirwan, A. J., et al., *Phys. Rev. Lett.* 58: 467–70 (1987)
213. Wyss, R., et al., *Phys. Lett.* 215B: 211–17 (1988)
214. Bengtsson, T., Ragnarsson, I., *Nucl. Phys.* A436: 14–82 (1985)
215. Dudek, J., See Ref. 10, pp. 195–221
216. Dudek, J., et al., *Phys. Rev. Lett.* 59: 1405–8 (1987)
217. Heyde, K., et al., *Phys. Rep.* 102: 291–393 (1983)
218. Arnell, S. E., et al., *J. Phys.* G9: 1217–35 (1983)
219. Ma, W. C., et al., *Phys. Lett.* 167B: 277–82 (1986)
220. Walus, W., et al., *Phys. Scr.* 34: 710–16 (1986)
221. Larabee, A. J., et al., *Phys. Lett.* 169B: 21–27 (1986)
222. Hcbbinhgaus, G., et al., *Z. Phys.* A328: 387–92 (1987)
223. Arima, A., Sakakura, M., Sebe, T., *Nucl. Phys.* A170: 273–308 (1971)
- 223a. Bengtsson, T., Ragnarsson, I., *Phys. Scr.* T5: 165–70 (1983)
224. Ragnarsson, I., et al., *Phys. Scr.* 34B: 651–68 (1986)
225. Ragnarsson, I., et al., *Phys. Rev. Lett.* 54: 982–85 (1985)
226. Stephens, F. S., et al., *Phys. Rev. Lett.* 54: 2584–87 (1985)
227. Cranmer-Gordon, N. W., et al., *Nucl. Phys.* A465: 506–28 (1987)
228. Beck, F. A., et al., *Phys. Lett.* 192B: 49–54 (1987)
229. Xing, Z., Ragnarsson, I., Bengtsson, T., *Phys. Lett.* 177B: 265–70 (1986)
230. Pakkanen, A., et al., *Phys. Rev. Lett.* 48: 1530–33 (1982)
231. Tjøm, P. O., et al., *Phys. Rev. Lett.* 55: 2405–8 (1986)
232. Beck, E. M., et al., *Phys. Lett.* 215B: 624–28 (1988)
- 232a. Ma, W. C., et al., *Phys. Rev. Lett.* 61: 46–49 (1988)
233. Emling, H., et al., *Phys. Lett.* 217B: 33–37 (1989)
234. Cerkaski, M., et al., *Phys. Lett.* 70B: 9–13 (1977)
235. Døssing, T., et al., *Phys. Rev. Lett.* 39: 1395–97 (1977)
236. Andersson, C. G., et al., *Nucl. Phys.* A309: 141–76 (1978)
237. Åberg, S., *Phys. Scr.* 31: 233–36 (1985)
238. Matsuyanagi, K., Døssing, T., Neergård, K., *Nucl. Phys.* A307: 253–76 (1978)
239. Døssing, T., Neergård, K., Sagawa, H., *Phys. Scr.* 24: 258–365 (1981)
240. Häusser, O., et al., *Phys. Rev. Lett.* 44: 132–35 (1980)
- 240a. Poletti, S. J., et al., *Nucl. Phys.* A448: 189–204 (1986)
241. Cerkaski, M., et al., *Nucl. Phys.* A315: 269–90 (1979)
242. Dudek, J., et al., *Phys. Rev.* C26: 1712–18 (1982)
243. Beck, F. A., et al., *Z. Phys.* A319: 119–32 (1984)
244. Deleplanque, M. A., et al., *Phys. Lett.* 195B: 17–21 (1987)
245. Schück, C., et al., *Nucl. Phys.* A496: 385–402 (1989)
246. Dudek, J., *J. Phys. Coll.* C10: 18 (1980)
247. Schulz, N., et al., *J. Phys.* G10: 1201–18 (1984)
248. Faessler, A., Płoszajczak, M., *Phys. Rev.* C16: 2032–38 (1977)
249. Åberg, S., *Nucl. Phys.* A306: 89–100 (1978)
250. Bonche, P., Flocard, H., Heenen, P. H., *Nucl. Phys.* A467: 115–35 (1987)
251. Sheline, R. K., et al., *J. Phys.* G14: 1201–35 (1988)
252. Åberg, S., Døssing, Th., Neergård, K., *Nucl. Phys.* A443: 91–119 (1985)
253. Twin, P. J., et al., *Phys. Rev. Lett.* 57: 811–14 (1986)
254. Bentley, M. A., et al., *Phys. Rev. Lett.* 59: 2141–44 (1987)
255. Moore, E. F., et al., *Phys. Rev. Lett.* 63: 360–63 (1989)
256. Ragnarsson, I., et al., *Nucl. Phys.* A347: 287–315 (1980)
257. Bengtsson, T., et al., *Phys. Scr.* 24: 200–14 (1981)
258. Andersson, C. G., et al., *Phys. Scr.* 24: 266–82 (1981)
259. Schutz, Y., et al., *Phys. Rev. Lett.* 48: 1535–37 (1982)
260. Dudek, J., Nazarewicz, W., *Phys. Rev.* C31: 298–301 (1982)
261. Chasman, R. R., *Phys. Lett.* 187B: 219–22 (1987)
262. Ragnarsson, I., Åberg, S., *Phys. Lett.* 180B: 191–97 (1986)
263. Bengtsson, T., Ragnarsson, I., Åberg, S., *Phys. Lett.* 208B: 39–44 (1988)
264. Nazarewicz, W., Wyss, R., Johnson, A., *Phys. Lett.* 225B: 208–14 (1989)
265. Nazarewicz, W., Wyss, R., Johnson, A., *Nucl. Phys.* A503: 285–330 (1989)
- 265a. Shimizu, Y. R., Vigezzi, E., Broglia, R. A., *Nucl. Phys.* A509: 80–116 (1990)
266. Åberg, S., et al., In *Proc. 26th Int. Winter Meet. on Nucl. Phys., Bormio, Italy, Ric. Sci. Educ. Permanente Suppl.* 63: 546–77 (1988)

267. Johansson, J. K., et al., *Phys. Rev. Lett.* 63: 2200–3 (1989)
268. Åberg, S., *Nucl. Phys.* A477: 18–36 (1988)
269. Haas, B., et al., *Phys. Rev. Lett.* 60: 503–6 (1988)
- 269a. Fallon, P., et al., *Phys. Lett.* 218B: 137–42 (1989)
270. Hebbinghaus, G., et al., *Phys. Lett.* 240B: 311–16 (1990)
271. Shimizu, Y. R., Vigezzi, E., Broglia, R. A., *Phys. Lett.* 198B: 33–36 (1987)
272. Dudek, J., et al., *Phys. Rev.* C38: 940–52 (1988)
273. Riley, M. A., et al., *Nucl. Phys.* A512: 178–88 (1990)
274. Carpenter, M. P., et al., *Phys. Lett.* 240B: 44–49 (1990)
275. Ye, D., et al., *Phys. Rev.* C41: R13–16 (1990)
276. Becker, J. A., et al., *Phys. Rev.* C41: R9–12 (1990)
277. Theine, K., et al., *Z. Phys.* A334: 361–62 (1989)
278. Tsang, C. F., Nilsson, S. G., *Nucl. Phys.* A140: 275–88 (1970)
279. Girod, M., Delaroche, J. P., Berger, J. F., *Phys. Rev.* C38: 1519–22 (1988)
280. Chasman, R. R., *Phys. Lett.* 219B: 232–36 (1989)
281. Delaroche, J. P., et al., *Phys. Lett.* 232B: 145–50 (1989)
282. Bonche, P., et al., *Nucl. Phys.* A500: 308 (1989)
283. Brack, M., See Ref. 158, pp. 227–61
284. Ragnarsson, I., et al., *Nucl. Phys.* A361: 1–22 (1981)
285. Sheline, R. K., Ragnarsson, I., Nilsson, S. G., *Phys. Lett.* 41B: 115–21 (1972)
286. Auerlot, D., et al., *Phys. Lett.* 149B: 6–8 (1984)
287. Erb, K. A., Bromley, D. A., See Ref. 160, pp. 201–310
288. Marsh, S., Rae, W. D. M., *Phys. Lett.* 180B: 185 (1986)
289. Betts, R. R., DiCenzo, S. B., Petersen, J. F., *Phys. Rev. Lett.* 43: 253–56 (1979)
290. Zurmühle, R. W., et al., *Phys. Lett.* 129B: 384–86 (1983)
291. Bengtsson, T., et al., *Preprint Lund-MPh-84/01*. Unpublished (1984)
292. Hamamoto, I., Ogle, W., *Nucl. Phys.* A240: 54–76 (1975)
293. Dudek, J., Nazarewicz, W., Faessler, A., *Nucl. Phys.* A412: 61–91 (1984)
294. Chasman, R. R., Wilkins, B. D., *Phys. Lett.* 149B: 433–35 (1984)
- 294a. Ragnarsson, I., Bengtsson, R., See Ref. 296, pp. 193–98
295. Dudek, J., Nazarewicz, W., Rowley, N., *Phys. Rev.* C35: 1489–1501 (1987)
296. Eberth, J., Sistemich, K., Meyer, R. A., eds., *Nuclear Structure of the Zirconium Region*. Berlin: Springer-Verlag (1988)
297. Flocard, H. C., See Ref. 296, pp. 143–54
298. Zhang, J.-Y., Åberg, S., *Nucl. Phys.* A390: 314–35 (1982)
299. Ragnarsson, I., *Hyperfine Interact.* 43: 425–40 (1988)
300. Bengtsson, T., Ragnarsson, I., Åberg, S., In preparation (1990)
301. Höller, J., Åberg, S., *Z. Phys.* A336: 363–64 (1990)
302. Dudek, J., Werner, T., Riedinger, L. L., *Phys. Lett.* 211B: 252–58 (1988)
303. Mottelson, B. R., Presented at NBI Meet., May 1988, Slidereport, Copenhagen
304. Okolowicz, J., Irvine, M., *J. Phys.* G15: 823–28 (1989)
305. Alder, K., et al., *Rev. Mod. Phys.* 28: 432 (1956)
306. Strutinsky, V. M., *J. Nucl. Energy* 4: 523 (1957)
307. Stephens, F., Asaro, F., Perlman, I., *Phys. Rev.* 96: 1568 (1954)
308. Lee, K., Inglis, D. R., *Phys. Rev.* 108: 774 (1957)
309. Dutt, I., Mukherjee, P., *Phys. Rev.* 124: 888–89 (1961)
310. Suekane, S., *Prog. Theor. Phys.* 21: 74 (1959)
311. Johansson, S. A. E., *Nucl. Phys.* 22: 529–52 (1961)
312. Rustugi, M. L., Mukherjee, S. N., *Phys. Rev.* 131: 2615 (1963)
313. Krappe, H. J., Wahsweiler, H. G., *Nucl. Phys.* A104: 633–41 (1967)
314. Vogel, P., *Nucl. Phys.* A112: 583–93 (1968)
315. Eichler, J., Faessler, A., *Nucl. Phys.* A157: 166–76 (1970)
316. Satpathy, L., Friedrich, H., Weiguny, A., *J. Phys.* 32: C6–269 (1971)
317. Onishi, N., Sheline, R. K., *Nucl. Phys.* A165: 180–89 (1971)
318. Gustafsson, C., Möller, P., Nilsson, S. G., *Phys. Lett.* 34B: 349–53 (1971)
319. Möller, P., Nilsson, S. G., Sheline, R. K., *Phys. Lett.* 40B: 329–32 (1972)
320. Larsson, S. E., Möller, P., Nilsson, S. G., *Phys. Scr.* 10A: 53–59 (1974)
321. Greenwood, L. R., et al., *Phys. Rev.* C10: 1211–12 (1974)
322. Leander, G. A., et al., *Nucl. Phys.* A388: 452–76 (1982)
323. Chasman, R. R., *Phys. Lett.* 96B: 7–10 (1980)
324. Möller, P., Nix, J. R., *Nucl. Phys.* A361: 117–46 (1981)
325. Nazarewicz, W., et al., *Nucl. Phys.* A429: 269–95 (1984)
326. Chasman, R. R., *J. Phys.* 45: C6–167 (1984)

327. Rozmej, P., Boening, K., Sobiczewski, A., *Preprint GSI-86-8* (1986)
328. Skalski, J., *Phys. Lett.* 238B: 6–10 (1990)
329. Möller, P., Nilsson, S. G., *Phys. Lett.* 31B: 283–86 (1970)
330. Möller, P., *Nucl. Phys.* A192: 529–80 (1972)
331. Chasman, R. R., *Phys. Lett.* 175B: 254–56 (1986)
332. Rozmej, P., Cwiok, S., Sobiczewski, A., *Phys. Lett.* 203B: 197–99 (1988)
333. Sobiczewski, A., et al., *Nucl. Phys.* A485: 16–30 (1988)
334. Cwiok, S., Nazarewicz, W., *Nucl. Phys.* A496: 367–84 (1989)
335. Bonche, P., et al., *Phys. Lett.* 175B: 387–91 (1986)
336. Robledo, L. M., et al., *Phys. Lett.* 187B: 223–28 (1987)
337. Egido, J. L., Robledo, L. M., *Nucl. Phys.* A494: 85–101 (1989)
338. Robledo, L. M., et al., *Phys. Lett.* 201B: 409–14 (1988)
339. Ward, D., et al., *Nucl. Phys.* A406: 591–612 (1983)
340. Nazarewicz, W., Olanders, P., *Nucl. Phys.* A441: 420–44 (1985)
341. Nazarewicz, W., In *Proc. Niels Bohr Centennial Conf., Nucl. Struct. 1985*, ed. G. B. Hagemann, R. Broglia, B. Herskind. Amsterdam: Elsevier (1985), p. 263
342. Żylicz, J., In *Nuclear Structure, Reactions and Symmetries*, Vol. I. Singapore: World Scientific (1986), p. 79
343. Dahlinger, M., et al., *Nucl. Phys.* A484: 337–75 (1988)
344. Phillips, W. R., et al., *Phys. Rev. Lett.* 57: 3257–60 (1986)
345. Nazarewicz, W., See Ref. 175, p. 180
346. Urban, W., et al., *Phys. Lett.* 185B: 331 (1987)
347. Urban, W., et al., *Phys. Lett.* 200B: 424–28 (1988)
348. Phillips, W. R., et al., *Phys. Lett.* 212B: 402–6 (1988)
349. Goodman, A. L., *Nucl. Phys.* A230: 466–76 (1974)
350. Nazarewicz, W., et al., *Phys. Rev. Lett.* 52: 1272–75 (1984)
351. Nazarewicz, W., et al., *Phys. Rev. Lett.* 53: 2060(E) (1984)
352. Frauendorf, S., Pashkevich, V. V., *Phys. Lett.* 141B: 23–27 (1984)
353. Faber, M. E., *Phys. Rev.* C24: 1047–54 (1981)
354. Faber, M. E., Płoszajczak, M., *Phys. Scr.* 24: 189–99 (1981)
355. Nazarewicz, W., Leander, G. A., Dudek, J., *Nucl. Phys.* A467: 437–60 (1987)
356. Nazarewicz, W., Olanders, P., *Phys. Rev.* C32: 602–8 (1985)
357. Schwartz, B., PhD thesis, Univ. Heidelberg (1988)
358. Schulz, N., et al., *Phys. Rev. Lett.* 63: 2645–48 (1989)
359. Ragnarsson, I., *Phys. Lett.* 130B: 353–58 (1983)
360. Sheline, R. K., Leander, G. A., *Phys. Rev. Lett.* 51: 359–62 (1983)
361. Leander, G. A., Sheline, R. K., *Nucl. Phys.* A413: 375–415 (1984)
362. Leander, G. A., et al., *Phys. Lett.* 152B: 284–90 (1985)
363. Leander, G. A., Chen, Y. S., *Phys. Rev.* C37: 2744–78 (1988)
364. Cwiok, S., Nazarewicz, W., *Phys. Lett.* 224B: 5–10 (1989)
365. Bohr, A., Mottelson, B. R., *Nucl. Phys.* 4: 529–31 (1957)
366. Bohr, A., Mottelson, B. R., *Nucl. Phys.* 9: 687–88 (1959)
367. Leander, G. A., *AIP Conf. Proc.* 125: 125 (1985)
368. Leander, G. A., et al., *Nucl. Phys.* A453: 58–76 (1986)
369. Dorso, C. O., Myers, W. D., Swiatecki, W. J., *Nucl. Phys.* A451: 189–201 (1986)
370. Denisov, V. Yu., *Sov. J. Nucl. Phys.* 49: 399–405 (1989)
- 370a. Myers, W. D., Swiatecki, W. J., *Nucl. Phys. A*. Submitted (1990)
371. Mach, H., et al., *Phys. Rev.* C41: R2469–73 (1990)
372. Butler, P., Nazarewicz, W., In preparation (1990)
373. Chasman, R. R., Ahmad, I., *Phys. Lett.* 182B: 261–64 (1986)
374. Cwiok, S., Nazarewicz, W., In preparation (1990)
375. Mach, H., et al., *Phys. Rev. C*. Submitted (1990)
376. Pauli, H. C., Ledergerber, T., Brack, M., *Phys. Lett.* 34B: 264–68 (1971)
377. Bolsterli, M., et al., *Phys. Rev.* C5: 1050–77 (1972)
378. Mustafa, M. G., Mosel, U., Schmitt, H. W., *Phys. Rev.* C7: 1519–32 (1973)
379. Möller, P., Nix, J. R., In *Physics and Chemistry of Fission, Proc. Int. Conf. at Rochester*. Vienna: IAEA (1974), 1: 103
380. Baran, A., et al., *Nucl. Phys.* A361: 83–101 (1981)
381. Möller, P., Nix, J. R., Swiatecki, W. J., *Nucl. Phys.* A469: 1–50 (1987)
382. Hulet, E. K., et al., *Phys. Rev. Lett.* 56: 313–16 (1986)
383. Blons, J., Mazur, C., Paya, D., *Phys. Rev. Lett.* 35: 1749–51 (1975)
384. Blons, J., et al., *Phys. Rev. Lett.* 41: 1282–85 (1978)
385. Fabbro, B., et al., *J. Phys. Lett.* 45: L843 (1984)
386. Bengtsson, R., et al., *Nucl. Phys.* A473: 77–110 (1987)

387. Hamilton, J. H., In *Lecture Notes in Physics 168, Heavy Ion Collision*. Berlin/Heidelberg/New York: Springer-Verlag (1982), p. 287
388. Hamilton, J. H., Hansen, P. G., Zganjar, E. F., *Rep. Prog. Phys.* 48: 631 (1985)
389. Hamilton, J. H., In *Treatise on Heavy Ion Science*, ed. D. A. Bromley. New York: Plenum (1989), 8: 1-98
390. Ogle, W., et al., *Rev. Mod. Phys.* 43: 424-78 (1971)
391. Arseniev, D. A., et al., *Phys. Lett.* 40B: 305-6 (1972)
392. Nielsen, B. S., Bunker, M. E., *Nucl. Phys.* A245: 376-96 (1975)
393. Alikov, B. A., et al., *Izv. Akad. Nauk SSR Ser. Fiz.* 48: 875 (1984)
394. Coc, A., et al., *Phys. Lett.* 192B: 263-67 (1987)
- 394a. Nazarewicz, W., Riley, M. A., Garrett, J. D., *Nucl. Phys.* A512: 61-96 (1990)
395. Galeriu, D., Bucurescu, D., Ivascu, M. J., *J. Phys.* G12: 329-48 (1986)
396. Bengtsson, R., See Ref. 296, pp. 17-25
397. Ahlpara, D. P., Bhatt, K. H., *Phys. Rev.* C25: 2072 (1982)
398. Grummer, F., Petrovici, A., Schmid, K. W., See Ref. 296, pp. 32-38
399. Petrovici, A., et al., *Nucl. Phys.* A483: 317-47 (1988)
400. Kumar, K., Baranger, M., *Nucl. Phys.* A110: 529-54 (1968)
401. Faessler, A., et al., *Phys. Lett.* 39B: 579-82 (1972)
402. Nilsson, S. G., et al., *Nucl. Phys.* A222: 221-34 (1974)
403. Dickman, F., Dietrich, W., *Z. Phys.* 271: 417 (1974)
404. Kolb, D., Wong, C. Y., *Nucl. Phys.* A245: 205-20 (1975)
405. Fraundorf, S., Pashkevich, V. V., *Phys. Lett.* 55B: 365-68 (1975)
406. Dionisio, J. S., et al., *J. Phys.* G2: L183-95 (1976)
407. De Wiclawik, W., et al., *J. Phys.* G3: L57-66 (1977)
408. Ragnarsson, I., In *Future Directions in Studies of Nuclei Far From Stability*, ed. R. C. Bingham, et al. Amsterdam: North-Holland (1980), p. 367
409. Frauendorf, S., May, F. R., Pashkevich, V. V., See Ref. 408, p. 133
410. Sauvage-Letessier, J., Quentin, P., Flocard, H., *Nucl. Phys.* A370: 231-55 (1981)
411. Girod, M., Reinhard, P. G., *Phys. Lett.* 117B: 1-4 (1982)
412. Köppel, Th. J., Faessler, A., Götz, U., *Nucl. Phys.* A403: 263-97 (1983)
413. Porquet, M.-G., et al., *Nucl. Phys.* A451: 365-91 (1986)
414. Bengtsson, R., et al., *Phys. Lett.* 183B: 1-6 (1987)
- 414a. Dracoulis, G. D., et al., *Phys. Lett.* 208B: 365-68 (1988)
415. Bengtsson, R., Nazarewicz, W., See Ref. 10, pp. 371-83
416. Dracoulis, G. D., et al., *J. Phys.* G12: L97-103 (1986)
417. Kortelahti, M. O., et al., *J. Phys.* G14: 1361-71 (1988)
418. Wallmeroth, K., et al., *Nucl. Phys.* A493: 224-52 (1989)
419. Heyde, K., et al., In *Proc. Int. Symp. on In-Beam Nucl. Spectrosc.*, ed. Zs. Dombradi, T. Fényes. Budapest: Akad. Kiado (1984), pp. 151-61
420. Heyde, K., et al., *Nucl. Phys.* A466: 189-226 (1987)
421. Heyde, K., See Ref. 447, p. 183
422. Dietrich, W., et al., *Nucl. Phys.* A253: 429-47 (1975)
423. Wohn, F. K., et al., *Phys. Rev.* C33: 677-90 (1986)
424. Arseniev, D. A., Sobiczewski, A., Soloviev, V. G., *Nucl. Phys.* A139: 269-76 (1969)
425. Faessler, A., et al., *Nucl. Phys.* A230: 302-16 (1974)
426. Ragnarsson, I., In *Proc. Int. Conf. on At. Masses, East Lansing, CERN Preprint TH.2766-CERN*. Geneva: CERN (1979)
427. Azuma, R. E., et al., *Phys. Lett.* 86B: 5 (1979)
428. Heyde, K., Moreau, J., Waroquier, M., *Phys. Rev.* C29: 1859-71 (1984)
429. Campi, X., Epherre, M., *Phys. Rev.* C22: 2605-11 (1980)
430. Nazarewicz, W., See Ref. 447, pp. 467-86
431. Van Duppen, P., et al., *Phys. Rev. Lett.* 52: 1974-77 (1984)
432. Bengtsson, R., Nazarewicz, W., *Z. Phys.* 334: 269-76 (1989)
433. Heyde, K., et al., *Phys. Lett.* 64B: 135-39 (1976)
434. Bounds, J. A., et al., *Phys. Rev. Lett.* 55: 2269-72 (1985)
435. Chasman, R. R., *Phys. Rev.* C14: 1935-45 (1976)
436. Bengtsson, T., *Nucl. Phys.* A496: 56-92 (1989)
437. Dendooven, D., et al., *Phys. Lett.* 226B: 27-30 (1989)
438. Heyde, K., et al., *Phys. Lett.* 218B: 287-90 (1989)
439. Ragnarsson, I., Broglia, R. A., *Nucl. Phys.* A263: 315-48 (1976)
440. Peker, L. K., Hamilton, J. H., *Bull. Am. Phys. Soc.* 31: 1765 (1986)
441. DeShalit, A., Goldhaber, M., *Phys. Rev.* 92: 1211 (1953)
442. Talmi, I., *Rev. Mod. Phys.* 34: 704 (1962)



443. Federman, P., Pittel, S., *Phys. Rev. C*20: 820–29 (1979)
444. Bès, D. R., Sorensen, R. A., *Adv. Nucl. Phys.* 2: 129 (1969)
- 444a. Bès, D. R., Broglia, R. A., Nilsson, B. S., *Phys. Rep.* 16C: 1–56 (1975)
445. Dobaczewski, J., et al., *Phys. Rev. Lett.* 60: 2254–57 (1988)
446. Dobaczewski, J., See Ref. 447, p. 227
447. Casten, R. F., et al., eds., *Contemporary Topics in Nuclear Structure Physics*. Singapore: World Scientific (1988)
448. Hamamoto, I., *Nucl. Phys.* 73: 225–33 (1965)
449. Casten, R. F., *Phys. Rev. Lett.* 54: 1991–94 (1985)
450. Iachello, F., Talmi, I., *Rev. Mod. Phys.* 59: 339–61 (1987)
451. Casten, R. F., Heyde, K., Wolf, A., *Phys. Lett.* 208B: 33–38 (1988)
452. Goswami, A., *Nucl. Phys.* 60: 228–40 (1964)
453. Chen, H. T., Goswami, A., *Phys. Lett.* 24B: 257–59 (1967)
454. Bar-Touv, J., et al., *Phys. Rev.* 178: 1670–81 (1969)
455. Goodman, A. L., et al., *Phys. Rev. C*2: 380–95 (1970)
456. Wolter, H., Faessler, A., Sauer, P., *Nucl. Phys.* A167: 108–28 (1971)
457. Goodman, A. L., *Nucl. Phys.* A186: 475–92 (1972)
458. Goswami, A., Kisslinger, L. S., *Phys. Rev.* B140: 26–31 (1965)
459. Nichols, K., Sorensen, R. A., *Nucl. Phys.* A309: 45–58 (1978)
460. Mühlhans, K., et al., *Phys. Lett.* 105B: 329–33 (1981)
461. Müller, E. M., et al., *Nucl. Phys.* A383: 233–50 (1982)
462. Goodman, A. L., *Nucl. Phys.* A402: 189–204 (1983)
463. Sheikh, J. A., et al., *Phys. Rev. Lett.* 64: 376–79 (1990)
464. Kreiner, A. J., Pomar, C., *Phys. Rev. C*36: 463–66 (1987)
465. Hendrie, D. L., et al., *Phys. Lett.* 26B: 127–31 (1968)
466. Aponick, A. A. Jr., et al., *Nucl. Phys.* A159: 367–84 (1970)
467. Hendrie, D. L., et al., *Phys. Rev. Lett.* 30: 571–74 (1973)
468. Moss, J. M., et al., *Phys. Rev. Lett.* 26: 1488–91 (1971)
469. Barlett, M. L., et al., *Phys. Rev. C*22: 1168–79 (1980)
470. Ronningen, R. M., et al., *Phys. Rev. C*28: 123–33 (1983)
471. Bertsch, G. F., *Phys. Lett.* 26B: 130–31 (1968)
472. Nilsson, S. G., et al., *Nucl. Phys.* A131: 1–66 (1969)
473. Bès, D. R., Broglia, R. A., *Phys. Rev. C*3: 2349–71 (1971)
474. Bès, D. R., Broglia, R. A., Nilsson, B., *Phys. Lett.* 40B: 338–44 (1972)
475. Lojewski, Z., Pomorski, K., *Nucl. Phys.* A345: 134–40 (1980)
476. Bhargava, P. C., *Nucl. Phys.* A207: 258–72 (1973)
477. Bhargava, P. C., Thouless, D. J., *Nucl. Phys.* A215: 515–24 (1973)
478. Hamamoto, I., *Nucl. Phys.* A232: 445–64 (1974)
479. Hamamoto, I., *Phys. Lett.* 66B: 222–25 (1977)
480. Wakai, M., Faessler, A., *Nucl. Phys.* A295: 86–110 (1978)
481. Mühlhans, K., et al., *Phys. Lett.* 120B: 44–48 (1983)
482. Garrett, J. D., et al., *Phys. Lett.* 118B: 297–302 (1982)
483. Diebel, M., *Nucl. Phys.* A419: 221–40 (1984)
484. Wyss, R., et al., *Nucl. Phys.* A503: 244–62 (1989)
485. Shimizu, Y. R., Matsuyanagi, K., *Prog. Theor. Phys.* 67: 1637 (1982)
486. Shimizu, Y. R., Matsuyanagi, K., *Prog. Theor. Phys.* 70: 144 (1983)
487. Shimizu, Y. R., Matsuyanagi, K., *Prog. Theor. Phys.* 74: 1346 (1985)
488. Serot, B. D., Walecka, J. D., *Adv. Nucl. Phys.* 16: 1 (1985)
489. Lee, S. J., et al., *Phys. Rev. Lett.* 59: 1171 (1987)
490. Pannert, W., Ring, P., Boguta, J., *Phys. Rev. Lett.* 59: 2420–22 (1987)
491. Price, C. E., Walker, G. E., *Phys. Rev. C*36: 354–64 (1987)
492. Fink, J., et al., *Phys. Lett.* 218B: 277–82 (1989)
493. Gambhir, Y. K., Ring, P., *Phys. Lett.* 202B: 5–9 (1989)
494. Blum, V., et al., *Phys. Lett.* 223B: 123–26 (1989)
495. Koepf, W., Ring, P., *Phys. Lett.* 212B: 397–401 (1988)
496. Koepf, W., Ring, P., *Nucl. Phys.* A493: 61–92 (1989)
497. Twin, P. J., In *Proc. Int. Nucl. Phys. Conf., Sao Paulo, Brasil*, ed. M. S. Hussein, et al. Singapore: World Scientific (1990), p. 373
498. Cwiok, S., et al., *Nucl. Phys.* A491: 281–89 (1989)
499. Macdonald, N., *Adv. Phys.* 19: 371–407 (1970)
500. Rowe, D. J., Bassermann, R., *Nucl. Phys.* A220: 404–28 (1974)
501. Goeke, K., Reinhard, P. G., *Ann. Phys. (NY)* 112: 328–55 (1978)